Die approbierte Originalversion dieser Dissertation ist in der Hauptbibliothek der Technischen Universität Wien aufgestellt und zugänglich.
http://www.ub.tuwien.ac.at

The approved original version of this thesis is available at the main library of the Vienna University of Technology.
http://www.ub.tuwien.ac.at/eng

TECHNISCHE UNIVERSITÄT WIEN

DISSERTATION

Network analysis of brain functions of patients with severe chronic disorders of consciousness using functional magnetic resonance imaging

Ausgeführt zum Zwecke der Erlangung des akademischen Grades einer
Doktorin der technischen Wissenschaften

unter der Leitung von
Ao.Univ.Prof.i.R. Privatdoz. Dipl.-Ing. Dr.sc.med. Dr.techn. Dr.rer.nat. Frank Rattay
Institut für Analysis and Scientific Computing (E101)

zweitbetreut von
Privatdozent Dipl.-Ing. Dr. Stefan M. Golaszewski
Paracelsus Medizinische Privatuniversität

eingereicht an der Technischen Universität Wien
Fakultät für Mathematik und Geoinformation

von
Dipl. -Ing. Mag. Bettina Wutzl Bakk. BSc
0625272
Osaka, Japan

Wien, am

Abstract

The diagnosis and prognosis of patients with severe chronic disorders of consciousness (scDOC) are still challenging and a lot of misdiagnosis is evident. We aim to show new techniques to get a better insight into these disorders and introduce methods that can help in the diagnosis, all focusing on functional magnetic resonance imaging (fMRI) as modality.

After a general introduction, an overview of fMRI is given. The physical and physiological basis is described. Furthermore, the most important experimental designs as well as analysis techniques are explained. The next part focuses on scDOC patients and presents definitions of the different diagnoses and challenges that are faced nowadays.

After these introductory sections, a chapter dealing with fMRI under anesthesia follows. The patient group of scDOC patients is especially difficult to investigate because they often cannot lie still for the duration of an fMRI scan. We show for the first time, as far as known to us, results of fMRI under anesthesia of a patient in minimally consciousness state. Such results are possible because we choose a specific task, namely stimulation with a brush. Moreover, in a second example we show that it is possible to detect brain activity in the motor cortex of a patient in the final stage of Creutzfeldt-Jakob disease when anesthetized. This is a new result because, up to now, it was assumed that patients in the late stages of Creutzfeldt-Jakob disease are in the apallic syndrome and thus do not activate the cerebral cortex no more.

The next part deals with the analysis of resting state fMRI. Resting state fMRI describes an fMRI experiment when the subject does not perform any task during scanning. This is of special interest for the considered patient group because no active participation of the subject is needed for such an examination. We present different analysis methods dealing with regions of interest (ROI). The first is an ROI-to-ROI analysis using a special connectivity analysis software. After that we turn to a method using graph theory. We construct networks out of the correlation matrices of the ROIs and then analyze the modularity with the multislice modularity approach. We choose this method because standard methods are not able to detect differences in the modularity of the different patient groups with scDOC. We are the first to use this new technique on this patient group and are able to detect differences between the subgroups. Furthermore, we introduce a new approach for a classifier which is based on modularity detection with the multislice method. The last part of this chapter combines a genetic algorithm and a support vector classifier to find the ROIs which differ most when considering the diverse groups of scDOC patients as well as healthy controls. The approach to combine a genetic

algorithm and a support vector classifier is well-established but it has never been used in this special way and with this patient group.

The last section gives a conclusion and outlook of what kind of work still has to be done in this field and shows how our new results can contribute to the understanding of this disease, e.g., by showing which ROIs are the most important indicators for the different types of disorders.

Zusammenfassung

Die Diagnose und Prognose von Patienten mit schweren chronischen Bewusstseinsstörungen (scBS) sind immer noch eine Herausforderung und eine hohe Anzahl an Fehldiagnosen ist bekannt. Wir zeigen neue Techniken um ein besseres Verständnis dieser Störungen zu erlangen und stellen Methoden vor, die bei der Diagnose behilflich sein könnten, alles im Hinblick auf funktionelle Magnetresonanztomographie (fMRT).

Nach einer allgemeinen Einleitung, wird ein Überblick über fMRT gegeben. Die physikalischen als auch physiologischen Grundlagen werden erklärt. Darüber hinaus wird ein Überblick über die wichtigsten experimentellen Methoden und Analysetechniken gegeben. Der nächste Abschnitt konzentriert sich auf Patienten mit scBS und führt die Definitionen der unterschiedlichen Diagnosen und die Herausforderungen, die sich gegenwertig stellen, an.

Nach diesen einführenden Kapiteln folgt ein Abschnitt der sich mit fMRT unter Anästhesie beschäftigt. Die betrachtete Patientengruppe ist eine sehr schwierig zu untersuchende Gruppe, da sie oft für die Dauer des fMRT Scans nicht still liegen kann. Wir zeigen, zu unserer Kenntnis zum ersten Mal, Resultate einer fMRT Untersuchung eines Patienten im Minimally Consciousness State unter Narkose. Diese Ergebnisse sind möglich, weil wir eine spezielle Methode, nämlich die Stimulation mit einer Bürste, wählen. In einem zweiten Beispiel zeigen wir, dass es möglich ist, im Endstadion der Creutzfeldt-Jakob Krankheit immer noch Aktivität im Motorkortex festzustellen, wenn der Patient unter Narkose steht. Dies ist eine neue Erkenntnis, weil bis jetzt geglaubt wurde, dass sich Patienten im Endstadion der Creutzfeldt-Jakob Krankheit im Apallischen Syndrom befinden und somit keinerlei cerebralen Kortex mehr aktivieren.

Der nächste Teil beschäftigt sich mit der Analyse von Ruhezustands fMRT. Eine solche Untersuchung beschreibt ein fMRT bei dem keinerlei Aufgaben durchgeführt werden. Diese Vorgehensweise ist von speziellem Interesse für Patienten mit scBS, da keinerlei aktive Teilnahme der Versuchsperson für eine solche Untersuchung nötig ist. Wir zeigen unterschiedliche Analysemethoden. Die erste ist eine Interessensregion zu Interessensregion Analyse einer speziellen Konnektivitätsanalysesoftware. Danach gehen wir zu einer Methode, die Graphentheorie verwendet, über. Wir konstruierten Netzwerke aus den Korrelationsmatrizen der Interessensregionen und analysieren die Modularität mit mehrschichtiger Netzwerkmodul Berechnung. Wir wählen diese Methode, weil die Standardmethoden keinerlei Unterschied in der Modularität der unterschiedlichen scBS Patientenuntergruppen finden können. Wir verwenden als Erste diese neue Technik und sind damit

fähig solche Unterschiede zu zeigen. Darüber hinaus stellen wir eine neue Methodik für einen Klassifikator, der auf der Mehrschicht-Modul Berechnung basiert, vor. Der letzte Teil dieses Abschnitts kombiniert einen genetischen Algorithmus mit einem Support Vektor Klassifikator, um die wichtigsten Interessensregionen zu finden, welche den größten Unterschied zwischen den diversen Krankheitsbildern als auch gesunden Probanden zeigen. Der Ansatz einen genetischen Algorithmus mit einem Support Vektor Klassifikator zu kombinieren ist gut etabliert, allerdings wurde es noch nicht in dieser speziellen Weise und mit dieser Patientengruppe gemacht.

Der letzte Abschnitt dient der Zusammenfassung und gibt einen Ausblick auf Arbeit, die noch getan werden muss und zeigt wie unsere Ergebnisse und Techniken zum Verständnis der Krankheit beitragen können, indem sie zum Beispiel aufzeigen, welche Interessensregionen am wichtigsten sind für die Unterscheidung der Patientensubgruppen.

Contents

1. Introduction 1
2. Functional magnetic resonance imaging 3
2.1. Overview of fMRI technology 3
2.1.1. Overview of magnetic resonance imaging (MRI) 4
2.1.1.1. The history of MRI 4
2.1.1.2. Underlying physical principles of MRI 5
2.1.1.3. Encoding techniques for MRI 11
2.1.2. FMRI and its physiological basis 12
2.2. Experimental design in fMRI 16
2.2.1. Comparing methods for different paradigm 16
2.2.2. Event-related and block design of stimuli 17
2.2.3. Temporal and spatial resolution of fMRI 20
2.3. FMRI signal analysis 21
2.3.1. Preprocessing 21
2.3.2.1. Quality control 21
2.3.2.2. Head motion and realignment 22
2.3.2.3. Slice timing 24
2.3.2.4. Coregistration 25
2.3.2.5. Normalization 26
2.3.2.6. Segmentation 28
2.3.2.7. Further common preprocessing techniques 29
2.3.2. Statistical analysis 32
2.3.3.1. The general linear model 34
3. Severe chronic disorders of consciousness (scDOC) 39
3.1. Different categories of scDOC 39
3.1.1. Coma 39
3.1.2. Unresponsive wakefulness syndrome (UWS) 40
3.1.3. Minimally conscious state (MCS) 41
3.1.3.1. MCS+ and MCS- 42
3.1.4. Locked-in syndrome (LIS) 42
3.1.5. Summary of the different stages of consciousness 43
3.2. Behavioral testing 44
3.2.1. Glasgow Coma Scale (GCS) 45
3.2.2. JFK Coma Recovery Scale-Revised (CRS-R) 46
3.2.3. Limits of behavioral testing 47
3.2.4. Summary of behavioral testing 48
4. Experiments under anesthesia 49
4.1. Case report 1: MCS patient 49
4.1.1. Introduction to case report 1 49
4.1.2. Clinical Case of the MCS patient 50
4.1.3. Methods used for the fMRI measurement of the MCS patient 52
4.1.3.1. The FMRI experiment 52
4.1.3.2. The used anesthesia 53
4.1.3.3. Data analysis 53
4.1.4. Results found from the fMRI experiment of the MCS patient under anesthesia 54
4.1.1. Summary of case report 1 54
4.2. Case report 2: patient with Creutzfeldt-Jakob disease 55
4.2.1 Introduction to case report 2 55
4.2.2 Creutzfeldt-Jakob disease 56

4.2.3 Clinical case of the CJD patient 58
4.2.4 Paraclinical investigations 59
4.2.5 Methods used for the fMRI experiment for the CJD patient 59
4.2.5.1 The fMRI experiment 59
4.2.5.2 The used anesthesia 60
4.2.5.3 Data analysis 61
4.2.6 Results found from the fMRI experiment of the CJD patient under anesthesia 61
4.2.7 Summary of case report 2 62
5. Analysis of resting state fMRI data 63
5.1. Introduction to resting state fMRI 63
5.1.1. Analysis methods for resting state fMRI data 64
5.1.2. Different resting state networks 65
5.2. Experimental details for the resting state fMRI measurement 70
5.3. Preprocessing of the resting state fMRI data 70
5.4. Connectivity analysis using the software CONN 72
5.4.1. Using the software CONN 72
5.4.2. Results found with the software CONN 73
5.4.3. Discussion of the results found with the software CONN 73
5.4.4. Summary of the connectivity analysis with the software CONN 74
5.5. Analyzing resting state fMRI data using networks and modularity 78
5.5.1. Mathematical definitions of networks and modularity 78
5.5.2.1. Mucha's multislice modularity 83
5.5.2.2. Accuracy, precision and recall 85
5.5.2. Introduction to the analysis of resting state fMRI data with networks and modularity 87
5.5.3. Methods for the analysis of resting state fMRI data with networks and modularity 88
5.5.3.1. Multislice Modularity 88
5.5.3.2. Classification 91
5.5.4. Results found when analyzing resting state fMRI data with networks and modularity 92
5.5.4.1. Results from the multislice modularity 92
5.5.4.2. Results from the classification 93
5.5.5. Discussion of the analysis of resting state fMRI data with networks and modularity .. 94
5.5.6. Summary of the analysis of resting state fMRI data with networks and modularity 95
5.6. Using genetic algorithm and support vector classifier for feature selection 96
5.6.1. Introduction to the use of genetic algorithm and support vector classifier 96
5.6.2. Genetic algorithm (GA) 97
5.6.3. Support vector classifier (SVC) 100
5.6.4. Methods for the combination of GA and SVC 103
5.6.5. Results found by the combination of GA and SVC 106
5.6.6. Discussion of the approach to combine GA and SVC for scDOC patients 111
5.6.7. Summary of the approach to combine GA and SVC for scDOC patients 112
6. Conclusion 113
7. Supplemental material 117
References 125
List of Abbreviations 141

1. Introduction

In the last decades, intensive care as well as emergency treatment have improved significantly, thus a lot more patients survive severe brain injuries or diseases. Nonetheless, not all of these patients recover fully, but some remain with severe chronic disorder of consciousness (scDOC) (Giacino et al., 2009; Laureys et al., 2006). We mainly distinguish two types of scDOC, namely unresponsive wakefulness syndrome (UWS), which describes patients that are not aware of themselves or their environment but do have a day and night circle, and minimally consciousness state (MCS), which are patients who react to some external stimuli but inconsequently (Giacino et al., 2002; Laureys et al., 2010). Moreover, there is the locked-in syndrome (LIS), which is a state that might look like the patients suffer from scDOC but indeed are totally aware of themselves and their environment, they just cannot communicate (Posner et al., 2007). Most of the time behavioral testing is taken as the golden standard when it comes to consciousness evaluation. What is important is that there is a huge misdiagnosis rate in the field of scDOC. In the literature we find a value of up to 43% for the misdiagnosis (Andrews et al., 1996; Giacino et al., 2009; Schnakers et al., 2009). A newer study from Russia even reports that 80% of MCS and 55% of UWS patients are initially misdiagnosed (Legostaeva et al., 2017). Such a high misdiagnosis rate can be devastating for the patients and has an impact on ethical as well as legal questions. Moreover, the diagnosis is also important for the prognosis of these patients (Luauté et al., 2010; Noé et al., 2012). Hence, new methods for the diagnosis are needed.

In the last years, neuroimaging techniques - like functional magnetic resonance imaging (fMRI) - have seemed to gain possible insights into scDOC (Gosseries et al., 2016, 2014; Hirschberg and Giacino, 2011; Jox et al., 2012). One famous example was reported by Owen et al. in 2006. They used fMRI to show that a patient diagnosed as being in UWS was actually in LIS and totally aware of herself and her environment (Owen et al., 2006). This is why a lot of physicians make their patients undergo fMRI, which can be a quite challenging task in daily clinic. Many of the patients suffering from scDOC also develop movement disorders or just do not tolerate being put into the scanner. Hence, we decided to anesthetize the patients in order to see whether we can find fMRI signals. There are studies focusing on anesthesia and the change of the fMRI signal due to anesthesia but up to now this was not done with scDOC patients. We used a special guided anesthesia and a robust stimulus (Rath et al., 2016). This method was able to detect fMRI signals of patients when under anesthesia (Wutzl et al., 2018).

Besides the actual scanning procedure and trying to improve the setup, there has also been research on new analysis methods. Resting state, which describes an investigation in which the subject does not have to actively participate is of special interest for this patient group. One new approach for the analysis is to use graph-theoretical methods. Studying graphs, or networks, is not a new topic and has been done in a lot of fields like computer sciences or also in applied fields like sociology. In the last decades, the theories developed in these different fields came to neuroscience (Sporns, 2010). We focused on one special technique whose basis are modules, i.e., nodes of the same module are more tightly connected to one another than to the nodes of the rest of the network (Fortunato, 2010; Girvan and Newman, 2002; Porter et al., 2009). What is known so far is that the brain network has a small-world structure and is modular with highly connected hubs (nodes with many of connections) (Bullmore and Sporns, 2009). These methods have also been used for scDOC patients, e.g., (Achard et al., 2012; Crone et al., 2014; Giacino et al., 2006; Schiff et al., 2005). Nevertheless, none of these studies was able to find differences in the modularity of the different groups of scDOC patients. We used a new method introduced by Mucha et al. in 2010 (Mucha et al., 2010). Instead of looking at every subject individually, we connected their graphs and calculated the modularity for the whole group. Using this method, we were able to find differences between healthy subjects and MCS patients, between healthy subjects and UWS patients, and between UWS and MCS patients. Furthermore, we introduce one classifier which is able to distinguish healthy controls and scDOC patients and also with a slight modification separates UWS and MCS patients better than at random.

Another approach that is used for trying to better understand these diseases is feature selection with a classification algorithm. We use a well-established method, namely combining a genetic algorithm (GA) with a support vector classifier (SVC). Even though the approach is not new, it has so far not been used for scDOC patients. We truncate the correlation matrix of the resting state fMRI in a special way so that we find the regions of interest (ROIs) that are most important for the distinction of the different disease groups as well as to healthy controls. These are also the ROIs that differ most when comparing the different groups.

2. Functional magnetic resonance imaging

Measuring the human brain, in particular its function, has been a challenge since early times of modern medicine. In the past, a lot was speculated about the brain functions and several of theories, especially by philosophers, have been made. Nowadays, we are able to measure the brain and its function directly and indirectly. Hence, there are a lot of different tools for measuring brain activity, like electroencephalography (EEG), positron-emission tomography (PET), functional magnetic resonance imaging (fMRI), magnetoencephalography (MEG), and even others. All these methods use different physical or physiological mechanisms to detect brain activity. We focus on fMRI, whose physical mechanisms are described in the following sections.

2.1. Overview of fMRI technology

FMRI is a technique that makes use of the blood oxygenation level dependent (BOLD) effect and measures the brain activity using magnetic resonance imaging (MRI). It is of special interest because it does not use any ionizing radiation, like X-rays, and is a completely non-invasive method. Considering its properties, it has a temporal resolution of seconds s and a high spatial resolution of millimeters mm. Figure 1 shows different neurological imaging techniques and compares their temporal resolution on the logarithmic-scaled x-axis in seconds versus the spatial resolution given on the logarithmic-scaled y-axis in millimeter. FMRI is shown in the upper middle part of the figure. As one can see, it occupies quite a big area of this chart. This indicates that fMRI is useable for a wide range of scales, i.e., it has a temporal resolution from hours to seconds and a spatial resolution from the entire brain down to neural columns. These properties make fMRI suitable for a lot of different experiments and examinations. The electrophysiological methods, like MEG and EEG, are shown in the upper left corner. Hence, their temporal resolution is better than that of fMRI, but their spatial resolution does not occupy such a big field, i.e., its spatial resolution is not as good as the one of fMRI. According to Figure 1, PET, which is shown in the upper right corner is not favorable, first because its temporal and spatial resolution are poorer than those of fMRI and beyond that it is an invasive method using radioactive substances. Looking at Figure 1, one finds that other techniques like the patch clamp technique do have even better temporal and spatial resolution than fMRI. Nevertheless, this technique is hard to use and is also an invasive method, which makes it less favorable.

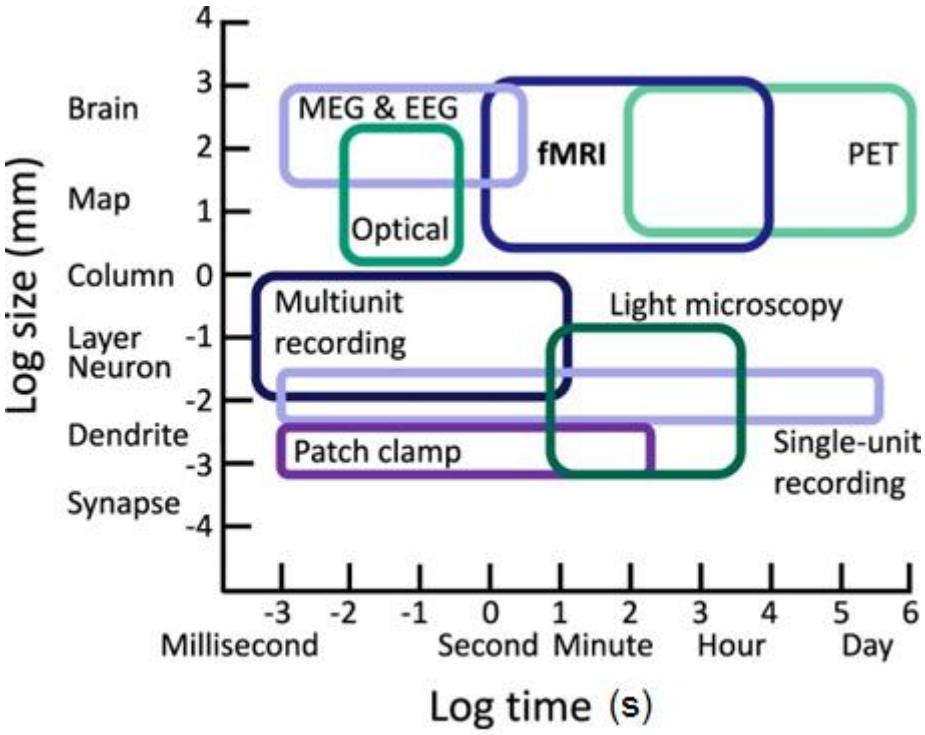

Figure 1: Overview of different neural measurement techniques and their relation to spatial and temporal resolution Modified from (Medaglia, 2017).

2.1.1. Overview of magnetic resonance imaging (MRI)

2.1.1.1. The history of MRI

MRI was first described by Paul Christian Lauterbur (06.05.1929 - 17.03.2007) in 1971 and published in 1973 (Becker, 2007; Filler, 2009). Since then it has been gaining more and more importance, especially in the field of medicine, where it is used quite regularly these days. In 2003, Lauterbur and Sir Peter Mansfield (09.10.1933 - 08.02.2017) received the Nobel Prize for physiology and medicine for their work on MRI (Filler, 2009; Morris, 2017).

The underlying principle of MRI is nuclear magnetic resonance (NMR) which is now known for a little less than hundred years. The first important scientist who worked on that field was Wolfgang Ernst Pauli (25.04.1900 - 15.12.1958) in the 1920s. This was followed by Isidor Isaac Rabi (29.07.1898 - 11.01.1988) who made an experiment to detect magnetic spins of nuclei in 1938 for which he won the Nobel Prize in 1944 (Filler, 2009; Peierls, 1960; Shampo et al., 2012).

Felix Bloch (23.10.1905 - 10.09.1983) and Edward Mills Purcell (30.08.1912 - 07.03.1997) described independently that the results of magnetic resonance found by Rabi in gases can also be found in

solids. This finding lead to the Nobel Prize in physics for both of them in 1952 (Bleaney, 1999; Hofstadter, 2008).

There are even more researchers, who were awarded the Nobel Prize for their work related to MRI namely Nicolaas Bloembergen (1981), Norman F. Ramsey (1989), Richard R. Ernst (1991) and Kurt Wüthrich (2002) (Boesch, 2004).

2.1.1.2. Underlying physical principles of MRI

In order to describe the basic principles of MRI we follow standard textbooks on this topic, like (Huettel et al., 2008; Plewes and Kucharczyk, 2012).

The main aspect of MRI makes use of NMR, which is a physical phenomenon describing that atomic nuclei absorb and re-emit electromagnetic radiation when brought into a magnetic field. Nucleons with a spin unequal to zero behave like little magnets. The most important nucleon for imaging is ^{1}H, which is one of the main elements found in the human body – but also, e.g., ^{13}C, ^{19}F, ^{23}Na or ^{31}P, are used. What makes an element suitable for MRI is when it has an odd number of neutrons or protons, i.e., it exhibits a spin unequal to zero. In the following we will focus on ^{1}H because it is most often used for MRI. Moreover, it is easy to describe because it consists of just a single proton. Nevertheless, all descriptions hold for all elements used for MRI.

The proton of the ^{1}H is positively charged and due to thermal effects, it rotates around its own axis like a spinning top. Other than a spinning top, it cannot be stopped nor can it be accelerated. The rotation produces a current and hence a magnetic field which is called magnetic moment μ. Furthermore, the proton has a mass. Hence, its spin results in an angular momentum denoted as J. What all nuclei for MRI have in common is that they have a magnetic moment μ as well as an angular momentum J. These two are proportional to each other given by a constant γ which is called the gyromagnetic ratio. This equality is shown in Equation (1).

$$\mu = \gamma \cdot J \tag{1}$$

As mentioned before γ is a constant and as such does not depend on any external condition such as pressure, temperature, or anything else and it is unique to each element. Its unit is rad per second and Tesla. Some values for the gyromagnetic ratio are given in Table 1– in the more commonly used unit of Mega Hertz per Tesla.

Table 1: Gyromagnetic ratio of different elements (Plewes and Kucharczyk, 2012)

Element	Gyromagnetic ratio (γ) [MHz/T]
^{1}H	42.58
^{2}H	6.53
^{19}F	2.627
^{23}Na	11.27
^{31}P	1.131
^{17}O	-5.77

The application of an external magnetic field to the protons leads to parallel and antiparallel alignment to the external magnetic field. The parallel as well as the antiparallel state are equilibrium states. The parallel state is the low energy state whereas the antiparallel is the high energy state.

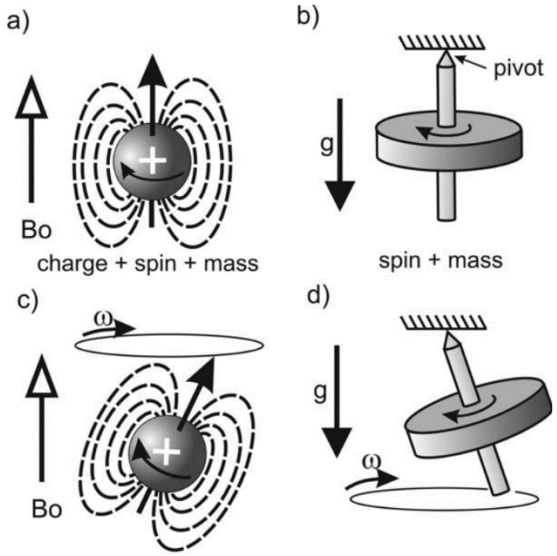

Figure 2: a) A proton in the outer magnetic field B_0 tries to align parallel (most of the times), b) a gyroscope in the outer gravitational field g, c) a proton precessing with an angular velocity of ω in the outer magnetic field B_0 d) a gyroscope precessing with an angular velocity of ω in the outer gravitational filed g (Plewes and Kucharczyk, 2012)

When a nucleon with a spin unequal to zero is brought into a magnetic field it tries to realign in a parallel or antiparallel direction to the outer magnetic field (more often it will align parallel to the outer magnetic field). Figure 2a) shows a nucleon parallel to the outer magnetic field B_0. This can be compared to a gyroscope in the Earth's gravitational field g - see Figure 2b) where a gyroscope hanging from a vertical pivot is shown. However, the proton also has an angular momentum. Hence, it starts precessing with an angular velocity ω around the axis of B_0 which can be seen in Figure 2c).

The same effect would occur if the gyroscope is slightly disturbed. It would also start to precess with ω around the outer axis of g (Figure 2d)). The frequency of this precession is proportional to B_0 as well as to γ which is, as mentioned above, unique to each element. This is summed up in the so called Larmor Equation (2).

$$\nu = \frac{\gamma}{2\pi} B_0 \qquad (2)$$

with ν being the Larmor frequency in Mega Hertz, B_0 in Tesla and γ in Mega Hertz per Tesla. See Table 2 for some values ν of some common elements.

Table 2: Larmor frequencies of different elements at different outer magnetic fields.

Element	**ν for B_0=1T [MHz]**	**ν for B_0=1.5T [MHz]**	**ν for B_0=3T [MHz]**
^{1}H	6.78	10.17	20.34
^{2}H	1.04	1.56	3.12
^{19}F	0.42	0.63	1.26
^{23}Na	1.79	2.69	5.37
^{31}P	0.18	0.27	0.54
^{17}O	-0.92	-1.38	-2.75

When a sample of several protons is brought into an outer magnetic field B_0, most of the protons will align parallel and some will align antiparallel to B_0. One might think that difference between the parallel and antiparallel aligned protons is huge, but it is rather small, i.e., just about one out of 100000 protons does not cancel out with another proton in antiparallel state. This one out of 100000 then contributes to the MRI signal. However, this leads to a net magnetization. Summing up all these protons that do not cancel out can be illustrated as one magnetization vector precessing around B_0. This can be seen in Figure 3.

In order to measure the precession magnetization, receiver coils are used - see Figure 4 for an illustration. The magnetic field varies due to the precession of the nucleons. Hence, a current is induced into the coils. This magnetization is known as *transverse component*. Two coils are used so that the direction of rotation as well as the angle can be determined at any time.

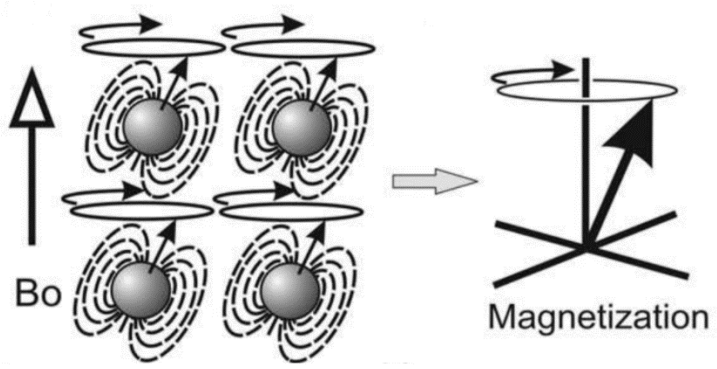

Figure 3: Showing just the protons that do not cancel out with a partner in the antiparallel state. (Plewes and Kucharczyk, 2012)

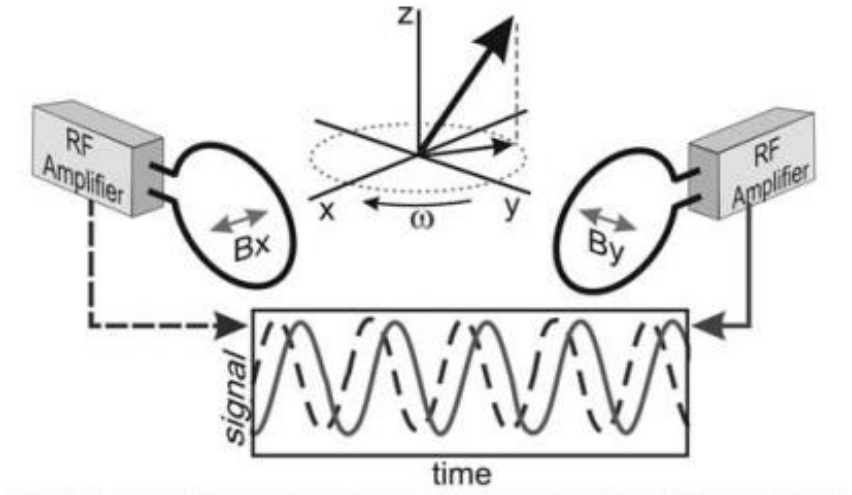

Figure 4: Two receiver coils for detecting the precessing magnetization.
(Plewes and Kucharczyk, 2012)

When irradiating the sample with exactly its ν, the net magnetization is flipped by a flip angle, e.g., of 90 °. After turning of the excitation, which is in general a radio frequency pulse, the atoms start to align again with B_0 which is shown in Figure 5 (B_0 in z-direction).

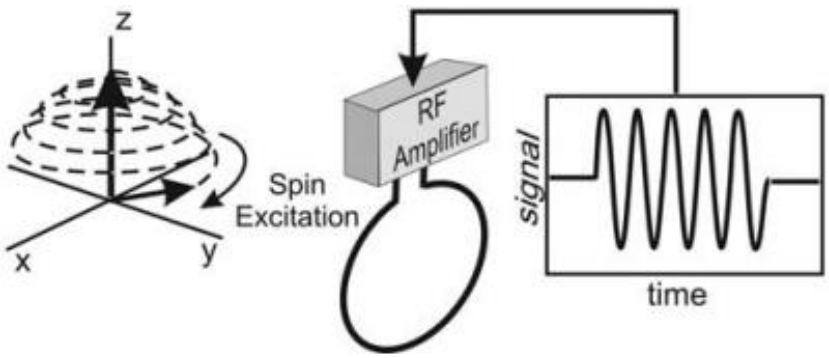

Figure 5: Irradiation of the net magnatization with ν results in precession in the transverse plane. (Plewes and Kucharczyk, 2012)

This realignment can be measured via free induction decay, which describes the radio frequency signal which is now emitted by the atoms when spinning back to their original aligned position. This is called *relaxation* and is of different duration depending on the tissue. Thus, this difference can be used for imaging purposes.

Up to now, we assumed that the magnetization is spatially homogeneous. Even with a perfect magnet, this is not a realistic assumption. Hence, the magnetization toward the tissue is heterogenous. This means that different spins precess with different ν. Using a rotating frame of reference with a rotation of the average of all spin rotations for description, we find that the magnetization vectors fan out in the transverse plane and hence, lose their alignment. This also leads to a decrease of the net magnetization and thus, a drop in the signal. This mechanism has a time constant T2* of the time when the signal drops to 1/e of its original value. The inhomogeneities have different origins. Some are intrinsic whereas others are extrinsic. The extrinsic inhomogeneities result from the magnet and its imperfection which can be accounted for by a constant T2'. In contrast to that, there are intrinsic factors contributing to T2*. The spins that are excited together have an effect on each other. Hence some precess faster and some are slowed down. This is characterized by the constant T2. For all these constants Equation (3) holds.

$$\frac{1}{T2^*} = \frac{1}{T2'} + \frac{1}{T2} \tag{3}$$

Thus, the T2* decay is always faster or equal to the T2 decay. This T2 relaxation is also called s*pin-spin relaxation* or *transverse relaxation*.

Besides this T2 relaxation, there is also the T1 relaxation which is also called *spin-lattice relaxation* or *longitudinal relaxation* and describes how the excited spins return to their lower energy state – most parallel to the outer magnetic field. The total magnetization is constant. Thus, the transverse magnetization decreases with the increase of longitudinal magnetization. The following formulae hold

$$M_z = M_0\left(1 - e^{-\frac{t}{T1}}\right) \text{ and} \tag{4}$$

$$M_{xy} = M_0 e^{-\frac{t}{T2}}. \tag{5}$$

In general, the phenomena of MRI can be described by a single equation called the *Bloch equation* (after Felix Bloch – see Section 2.1.1.1). This equation reads

$$\frac{dM}{dt} = \gamma\, M \times B + \frac{1}{T1}(M_0 - M_z) - \frac{1}{T2}\left(M_x + M_y\right). \tag{6}$$

It describes how a net magnetization M of a spin system evolves over time with a present total magnetization B, with T1 and T2 being the relaxation times, M_0 the original magnetization and M_x, M_y and M_z the magnetization in the spatial directions.

The following Figure 6 shows the different behaviors for M_z and M_{xy} depending on T2 and T1, respectively.

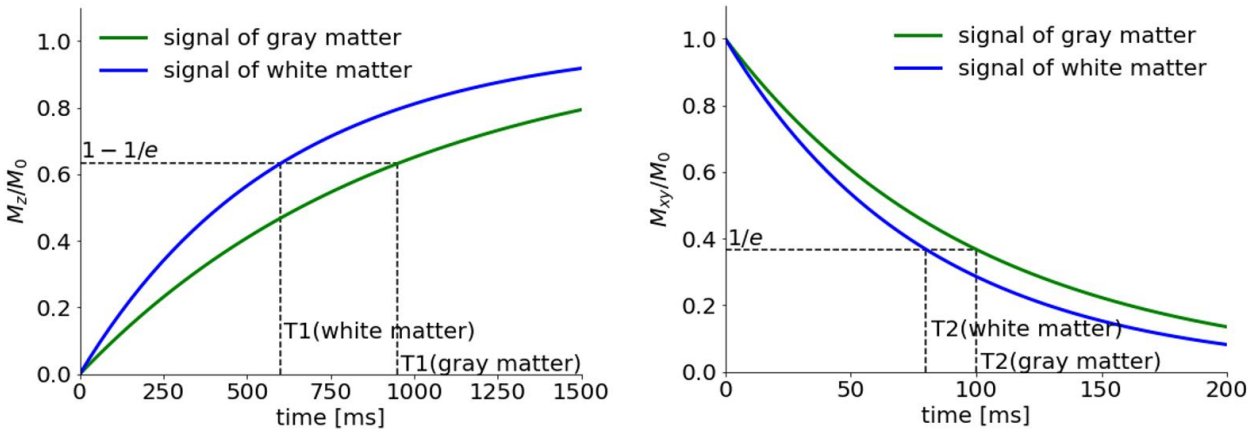

Figure 6: Behavior of M_z and M_{xy} depending on T2 and T1 respectively for different tissue types.

The following Table 3 shows some examples of different tissue types and their relaxation times T1 and T2 for a magnetic field strength of 1.5 Tesla.

Table 3: Examples of T1 and T2 relaxation times for different tissue types at 1.5 Tesla (Plewes and Kucharczyk, 2012)

Tissue	**T1 [ms]**	**T2 [ms]**
Gray matter	950	100
White matter	600	80
Muscle	900	50
Cerebrospional fluid	4500	2200
Fat	250	60
Blood	~1400	~180-250

Despite the fact that T1 is in general larger than T2, the two constants do not fulfill any proportionality. This is because the underlying molecular dynamics are fundamentally different.

2.1.1.3. Encoding techniques for MRI

What is unique to MRI, in comparison to other imaging techniques, is that the signal is created by the entire object and not just by a single point in space. Hence, some form of spatial encoding is needed to determine the location of the origin of the signal. This is done by nonuniform magnetic fields so that the spin locations are encoded in the different ν values. A key task for encoding is *selective excitation*. The following Figure 7 illustrates the combination of NMR, magnetic field gradient, and a band pass filtered radio frequency excitation pulse. In order to get an axial image of a specific region (the shaded area in Figure 7 a) the first step is to apply a field gradient in z-direction (the direction of B_0). This results in a ν of the atoms which is dependent on the location in z-direction. The shaded part consists of ν values from f1 to f2 (Figure 7 b). Then a radio frequency pulse, which is band pass filtered to f1 to f2, is applied (Figure 7 c). After turning off the radio frequency pulse, a transverse magnetization remains in the desired area whereas the other areas (the not shaded ones) are not changed (Figure 7 d).

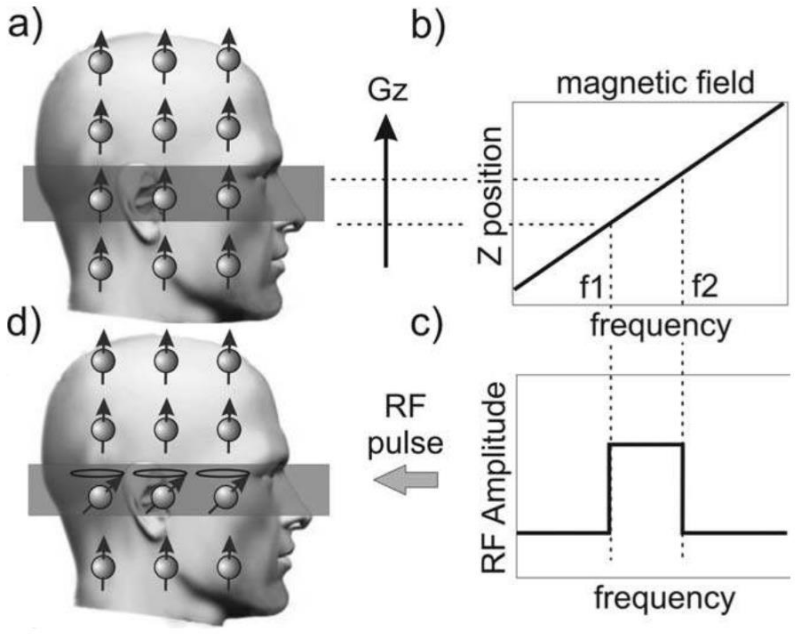

Figure 7: Selective excitation: a) The shaded area is transversely magnetized. b) A field gradient in z-direction is applied which results in a location dependent field and Larmor frequency between f1 and f2 c) a band pass filtered radio frequency pulse from f1 to f2 is applied d) just the protons in the shaded area are excited. (Plewes and Kucharczyk, 2012)

Now, what remains is to determine the location of the signal in the slice. The two missing steps are the so-called *frequency encoding* and the *phase encoding*. The phase encoding step is the one that is performed first. It is also a spatial gradient, applied in y-direction. By applying it, the protons start to precess at different frequencies. Hence, after some time they are not in phase anymore, which can later on be used for encoding. The last one is the frequency encoding, which is also a spatial gradient (in x-direction). It is simultaneously applied during signal acquisition. The name frequency encoding is due to the fact that this gradient changes the frequencies of the protons which, by that time, are already phase shifted. Thus, now we have a 3-dimensional encoding of the space.

For further details on MRI see, e.g., (Haacke et al., 1999; Huettel et al., 2008; Jin, 1998; Slichter, 1996).

2.1.2. FMRI and its physiological basis

In this chapter we follow the descriptions of (Uludag et al., 2015) Chapter 8 and (Huettel et al., 2008) Chapter 7.

In 1990, Seiji Ogawa and colleagues (Ogawa et al., 1990) described for the first time the possibility of measuring physiological activity of the brain indirectly using BOLD contrast. Since the introduction of fMRI in 1992 (Bandettini et al., 1992; Kwong et al., 1992; Ogawa et al., 1992) there has been a lot of progress – not only in the hardware but also in the software and analysis tools which made fMRI a widespread tool nowadays. BOLD does not measure neural activity itself but rather a series of indirect effects, i.e., it measures changes of magnetic properties of water which reflect changes of deoxygenated hemoglobin (dHb) content. While the first fMRI was recorded using a contrast agent, the main contrast used nowadays is BOLD. It is an endogeneous contrast and as such does not have the same problems as exogeneous contrasts sometimes face. In order to measure the BOLD contrast, one has to consider the oxygenation supply of the brain. Hemoglobin is what transports oxygen through the body. Linus Carl Pauling (28.02.1901 – 19.08.1994) and his student Charles DuBois Coryell (21.02.1912 – 07.01.1971) studied hemoglobin in 1936 and made some interesting discoveries, namely oxygenated and deoxygenated hemoglobin have different magnetic properties (Dunitz, 1996; Times, 1971). Thus, oxygenated hemoglobin (hemoglobin saturated with oxygen) is diamagnetic and has a susceptibility similar to the one of tissue whereas dHB (hemoglobin with no bound oxygen) is paramagnetic, i.e., it distorts surrounding magnetic fields. Hence, the protons in the vicinity are exposed to different field strength during the MRI measurement which

results in different precessing frequencies. T2* sensitive pulse sequences show more signals in regions with highly oxygenated blood in comparison to regions with deoxygenated blood.

When a brain region is active the energy demand increases in this region. Hence, the inflow of oxygenated blood is increased. However, the oxygenation demand is overcompensated and thus leads to a local change in the magnetic field. Thus, the increase in oxygenation leads to an increase in the signal of this region. The three main sources for measuring a BOLD signal are the cerebral blood flow (CBF), cerebral metabolic rate of oxygenation consumption ($CMRO_2$) and the cerebral blood volume (CBV) - see Figure 8 for a schematic view. This figure shows, how the different parts interact with each other. Neural events, e.g., action potentials or synaptic activity need oxygen (measured in the $CMRO_2$) and glucose (measured in the cerebral metabolic rate of glucose consumption). Hence, an increase of neural response leads to an increase in CBF. This blood inflow has an effect on the CBV, the dHb, and the blood outflow of the specific area, i.e., the CBV and blood outflow increase with the inflow whereas the dHb decreases. The blood outflow has an influence on the dHb and the CBV which both affect the BOLD response.

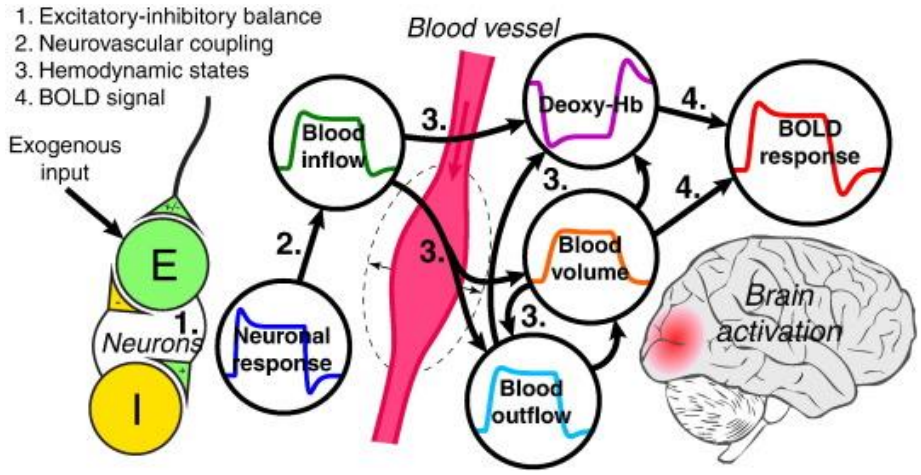

Figure 8: Physiological and physical processes for fMRI measurement. Arrows indicate the direction of influence. On the left-hand side two neurons are shown that try to keep a balance between excitation and inhibition. On the right-hand side a blood vessel with different influences is shown. The neural response has an influence on the blood inflow which itself influences the deoxy-Hb, the CBV, and the CBF which then have an direct or indirect influence on the BOLD response. (Havlicek et al., 2015)

The problem one has to face when dealing with BOLD, is that similar BOLD signals can be generated from different underlying changes. If the CBF rises also the blood oxygenation rises and hence a

bigger signal intensity is observed. The opposite holds for $CMRO_2$, i.e., if the $CMRO_2$ increases, the blood oxygenation and hence the signal intensity decreases. Considering CBV both of the following can hold: if it increases, the blood oxygenation can increase or decrease.

The change in signal is referred to as hemodynamic response which has a time variation given by the hemodynamic response function (HRF), shown in Figure 9. This figure shows two examples of the HRF, which is dependent on the stimulus and hence the underlying neuronal activity. Figure 9 (A) shows the HRF for an event stimulus whereas Figure 9 (B) shows the HRF for a block design (longer lasting stimulus). Some studies have reported an initial dip, i.e., a short-term decrease in the signal. This is not shown in Figure 9 because it is not always reported and not fully understood up to now.

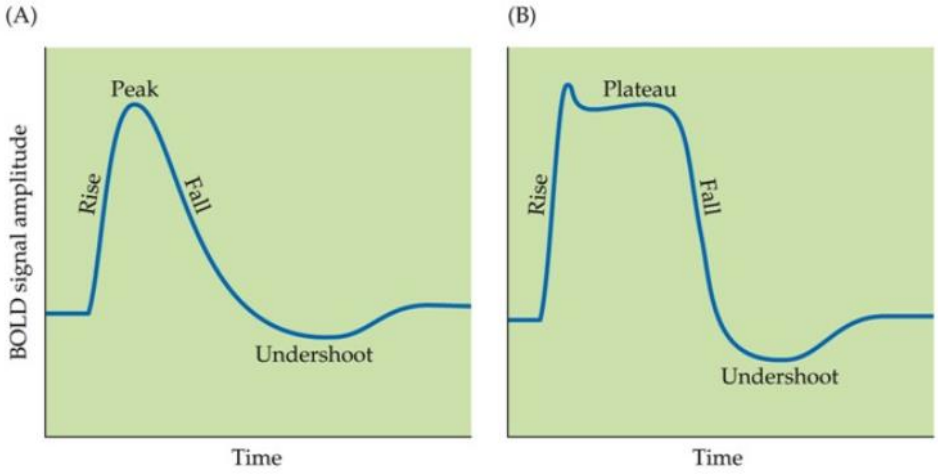

Figure 9: BOLD HRF: response to a single event (A) and response to a block of events (B) (Huettel et al., 2008)

Figure 10 shows the initial dip for different events of very short duration. The initial dip has in general a duration of 1 or 2 seconds. As mentioned above, the initial dip is not easy to detect especially in not so high field strength and it seems that the initial dip scales with field strength. Hence, it was reported that the initial dip at 1.5 T was just one third of the proportion magnitude measured in 4 T experiments. It seems that the initial dip results from small vessels which are more sensitive to field strength. Nevertheless, the initial dip is not fully understood up to now and needs further investigation. After the initial dip the HRF rises to its peak at around 4 to 6 seconds after the stimulus onset. This rise is due to the inflow of oxygenated blood and a hyper compensation of the used oxygen. If the stimulus has a longer duration, i.e., the neuronal activity lasts longer, the HRF reaches some plateau which is slightly below the peak of the function (see Figure 9). After the stimulus and the neuronal activity

stop the HRF experiences some undershoot. There are different explanations for this undershoot. The following 3 are the most plausible ones:

1. Balloon or Windkessel model: The dHb content is evaluated due to higher CBV, i.e., the CBV returns slower to baseline than CBF (Buxton et al., 1998; Mandeville et al., 1999, 1998).
2. Less oxygenated hemoglobin: CBF sinks under the baseline after the stimulus stops. This might be due to neuronal inhibition or other unbalanced excitation-inhibition activity after the stimulus (Logothetis et al., 2001; Uludağ et al., 2004).
3. Sustained oxygen consumption: More dHb is produced because the oxygen consumption goes on after the stimulus stopped. Thus, CBF recovers before $CMRO_2$ does (Frahm et al., 1996; Lu et al., 2004).

It is worth mentioning that these three causes do not exclude each other but rather cause the undershoot all together.

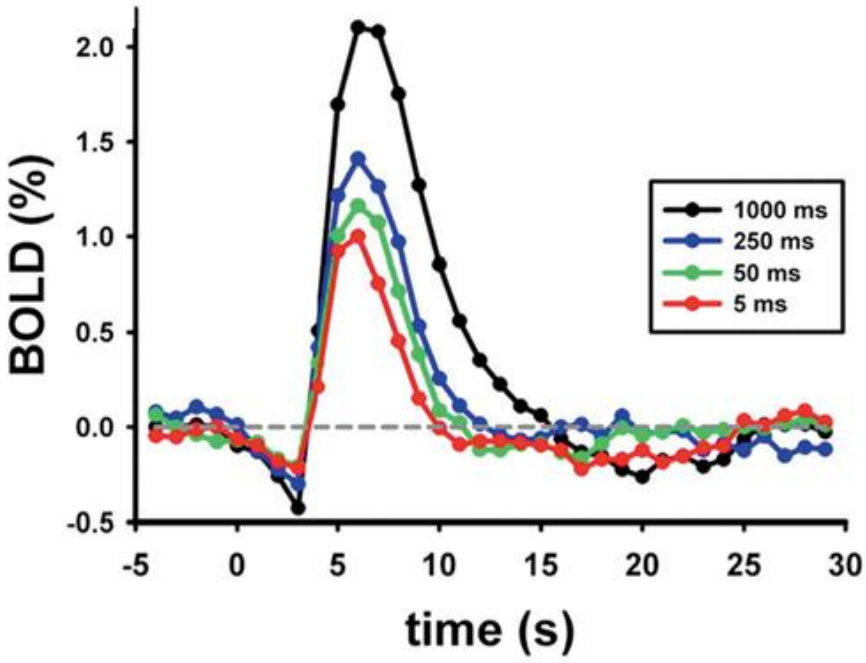

Figure 10: fMRI courses for single events of very short duration showing the initial dip at a field strength of 3 Tesla (Uludag et al., 2015)

For further details see standard literature of fMRI, e.g., (Huettel et al., 2008; Uludag et al., 2015).

2.2. Experimental design in fMRI

The main goal of fMRI is to localize specific brain functions caused by some stimuli, e.g., sensory motor or cognitive stimuli. This localization is often referred to as ‘brain mapping’. The fact that the amplitude change of the BOLD signal is as low as 1-5% of the MRI signal and the fact that there are many confounding effects, such as head movement or signal drifts, make brain mapping not an easy task. Hence, a lot of mathematical and computational methods are required to find the right regions. These different methods will be described in this chapter.

The state-of-the-art scanner nowadays operates with 3 Tesla. Most fMRI use echo planar imaging (EPI) with a matrix of 64x64 voxels and 40 slices. The time between the scan of one voxel to the next scan of the same voxel is called repetition time (TR) and gives the temporal resolution of the fMRI. A standard protocol takes a few seconds to scan the whole brain. Such an image is referred to as functional image. Several functional images scanned uninterrupted are referred to as run. As a rule of thumb, it is said to best ‘acquire the data perpendicular to the longest axis of the structure of interest.’ (Amaro and Barker, 2006) p. 8. Beside these functional runs, in general also a T1 weighted MRI, which has a very good white-gray matter contrast with a resolution close to 1 mm^3, is acquired. This image is mainly used for visualization but can also serve for restricting the statistical data to cortical voxels.

For a more detailed description of the following see, e.g., (Amaro and Barker, 2006).

Now let us have a look at the paradigm design. A paradigm is defined as ‘construction, temporal organization structure, and behavioral predictions of cognitive tasks executed by the subject during an fMRI experiment.’ (Amaro and Barker, 2006) p. 4. This is the most important part when conducting an experiment and has to be addressed in the very beginning.

2.2.1. Comparing methods for different paradigm

The first and most traditional way is the so-called *subtraction* approach where two images (one with a control condition and the other with the active condition) are subtracted from each other (Friston et al., 1996). Such an approach assumes that two conditions can be added and do not interact among each other, an assumption which does not hold true in general. Nevertheless, it is useful as simple

model of the BOLD response and moreover, gives robust and reproducible results (Friston et al., 1999).

The next approach is called *factorial* approach and allows, other than the subtraction approach, also to test for interactions of components (Friston et al., 1996). The main idea behind this is to test the components separated but also mixed in the paradigm. The underlying principle is linearity of the BOLD response from different conditions. This approach is very useful to investigate cognitive interactions (Gurd et al., 2002).

The next is the *parametric* strategy which can be used for tasks with different levels of difficulty. Thus, the underlying idea is to increase the cognitive demand without changing the nature of the task. The approach is that the increase of the cognitive demand would also increase the BOLD (Büchel et al., 1998). Even though this strategy is very interesting in theory it is hard to perform in practice . It is very challenging to increase one parameter without using other cognitive processes.

The last one is the so-called *conjunction* approach which is similar to the factorial one, but just involves two or more conditions at the same time, i.e., no stimulus is tested by itself but always at least paired with one other stimulus (Bremmer et al., 2001). What distinguishes this approach from others is that it searches for commonalities rather than difference in tasks, i.e., it tries to find the common pattern of the BOLD response given by the different stimuli (Friston et al., 1999).

Nevertheless, all of these four approaches can, and in general are, combined. An overview of all four different methods can be found in Figure 11.

2.2.2. Event-related and block design of stimuli

Considering the experimental stimuli there are two mayor types, namely *event-related* and *block design*. See Figure 12 for the different types of stimuli.

Block design refers to a stimulus presentation that is clustered together in blocks and these blocks, of several seconds up to minutes, are repeated after an interblock interval. This design together with the subtraction approach (see Section 2.2.1) has dominated in the beginning of the fMRI years because of the simple fact that it was applied in PET and thus, people were familiar with it. Despite all of the

drawbacks and criticism, it is still very common. This is mainly because of its robustness, increased statistical power and large BOLD signal changes (Buxton et al., 1998; Friston et al., 1999).

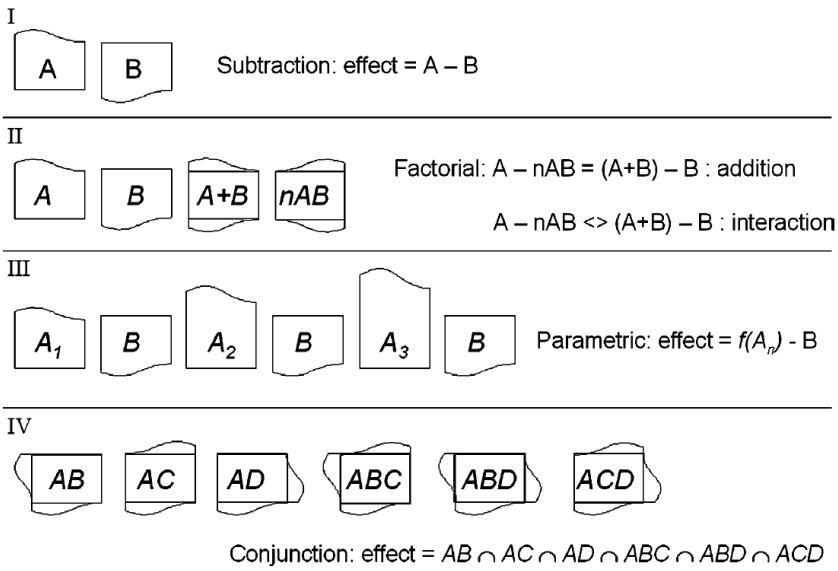

Figure 11: Overview of the different experimental strategies. I) Pure subtraction approach assumes that the conditions A and B do not interfere with each other. II) Factorial design also allows to test for interactions between conditions A and B. III) Parametric strategy showing two main tasks A and B with one task, A, changing the level of difficulty from easy A_1 to most difficult A_3. IV) Conjunction analysis where always two or more conditions, i.e., a combination of A, B, C, and D, are present at the same time and commonalities are searched for.
(Amaro and Barker, 2006)

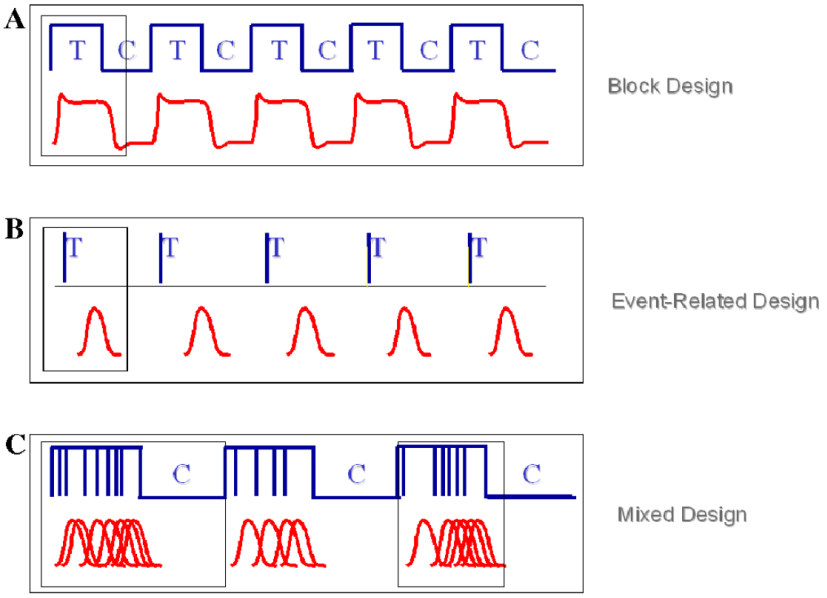

*Figure 12: Different types of stimuli: **A** block design: the tasks are presented in a block T which alternate with interblock condition C. **B** event-related design: very short stimuli T just occur once in a while. **C** mixed design: mixture of event and block design: there are blocks during which event-related stimuli are presented. These blocks are again intermitted by a rest condition C.*
(Amaro and Barker, 2006)

On the other hand, there is also event-related design. This design method describes stimuli which are of very short duration and just occur once in a while. The main advantage of this type of stimulus is that it makes use of the higher temporal resolution fMRI has in comparison to PET. It is even possible to detect transient variations in the HRF. What is also important is that different brain areas associated with the same stimulus may have different HRF (Kruggel and von Cramon, 1999). Moreover, using this event design it is also possible to analyze results of individual trials and hence maybe find out errors in challenging tasks (Braver et al., 2001; Kiehl et al., 2000; Schacter et al., 1997). Another important advantage is that event-related design is less sensitive to head motion (Birn et al., 1999; Huang et al., 2002). In general, this design type has a minimal interstimulus duration of the time of the HRF. This can be overcome by so-called rapid event-related MRI. However, the main problem with this technique is issue of linearity or non-linearity of the BOLD interaction in overlapping HRFs (Friston et al., 1998b; Glover, 1999; Hinrichs et al., 2000). What is best for all these designs is always to keep the interstimulus interval different so that the subject cannot predict when the next stimulus comes and pays more attention to the experiment.

The last type shown in Figure 12 is mixed design. This term describes a combination of blocks which consist of single events. It helps to investigate which neural activations are maintained and which are transient neural activations during paradigm performance (Donaldson et al., 2001; Otten et al., 2002). Nonetheless, it has the huge drawback that the HRF shape cannot be estimated that well.

Block designs as well as event-related designs have advantages and disadvantages and it depends on the specific research question which one is most suitable for the experiment. The main advantage of event-related over block designs is that there are no adaptation effects. Nevertheless, one has to keep in mind that the response function has a delay of several seconds. Hence, the individual trials should be separated by at least that interval in order to prevent overlaps. Otherwise, complex mathematical methods need to be applied to separate the overlaid signals. As a general rule, it holds that if one wants to optimize detection power it is better to use a block design whereas an event-related design is better for estimation efficiency.

Nevertheless, a substantial problem remains, namely that the measured brain activity is not an absolute quantity and hence quantitative interpretation is difficult. Thus, most fMRI experiments also record a baseline. Having such a baseline gives a control condition to which changes in BOLD can be compared.

2.2.3. Temporal and spatial resolution of fMRI

As mentioned above, the temporal resolution is given by the TR, which is the time between two excitation pulses. It holds: the shorter the TR, the less time to collect slice data. This is due to the characteristics of the HRF that there is no use for imaging at a TR lower than 1 s (Constable and Spencer, 2001). On the other hand, a high TR will result in a longer experiment time which can become uncomfortable for the subject. Guidelines for clinical fMRI studies are given by Amaro and Barker as: 2 min per condition but each run should not exceed 12 minutes and the session should not exceed 40 minutes (Amaro and Barker, 2006).

When it comes to the spatial resolution one would wish to get the smallest possible voxel size and image boundaries which includes the whole brain. Nonetheless, one has to keep in mind that a smaller voxel size will lead to a longer time to obtain the scan. Sometimes increasing the voxel size is desirable, e.g., when trying to detect sensitive BOLD effects. This is because an increase in the voxel size also leads to an increase of tissue in the voxel and thus to an increase of the BOLD signal (Howseman et al., 1999). On the other hand, reducing the voxel size is unfavorable for the signal-to-noise ratio of the image. A good guide for setting the optimal voxel size is the cortical thickness, i.e., 3-4 mm (Amaro and Barker, 2006).

Put together, most of the time, it is a challenge to find a tradeoff between spatial and temporal resolutions as well as total scanning time. Two techniques, that assess this problem, are jittering and parallel imaging. Jittering means that the delays between the starting times of sampling the brain volume and the starting times of the stimulus presentation are different. This results in different time points (relative to the start of the experiment) being sampled each time. There are two main approaches to jittering. The first is to use a so-called *fixed jittering scheme,* i.e., the interscan interval is not a multiple of the TR. The second approach is the so-called *variable jittering scheme,* which means that the interscan interval is varied each time. Amaro and Barker advise to use jittering when a high temporal resolution as well as a full brain coverage is needed but scanning time and behavior analysis are not so important. The next approach, addressing the spatial and temporal resolution issue, is parallel acquisition which is highly dependent on the hardware of the used scanner. This technique is often used nowadays and can reduce the scanning time by a factor of, generally, 2 to 3. Using parallel imaging, susceptibility artefacts are reduced. Furthermore, signals from mesial temporal and basal frontal regions are improved. Nevertheless, the signal-to-noise ratio is reduced (Amaro and Barker, 2006).

2.3. FMRI signal analysis

After this introduction to the different methods and challenges when measuring brain signals, we now turn to the signal analysis. This section follows standard books like (Huettel et al., 2008; Strother, 2006; Uludag et al., 2015).

Setting up the right measurement protocol for fMRI is very challenging and so is its analysis. The signal of interest measured by fMRI is very low in comparison to the noise also contained in the signal. The analysis procedure now faces the problem of extracting exactly the signal of interest from the whole signal, which contains also these huge amounts of noise. There are many steps needed to find the signal of interest. In the following an overview over some of these procedures is given.

2.3.1. Preprocessing

Computational steps following the image reconstruction, but before the statistical analysis, are in general known as *preprocessing*. With the introduction of new high field scanners, not just images get better, but also artefacts get more pronounced. Hence, preprocessing and especially artefact removal gets more and more important.

As mentioned before, a lot of preprocessing has to be done before the data of fMRI experiment can be analyzed. There are a lot of different preprocessing steps depending on what analysis is aimed for. All these steps are included in the most common software packages like Statistical Parametric Mapping (SPM, https://www.fil.ion.ucl.ac.uk/spm/), FMRIB software library (FSL, https://fsl.fmrib.ox.ac.uk/fsl/fslwiki/), Analysis of Functional NeuroImages (AFNI, https://afni.nimh.nih.gov/), and BrainVoyager (https://www.brainvoyager.com/).

2.3.2.1. Quality control

Before starting the whole preprocessing pipeline, it is crucial to perform an initial quality control check on the raw data. This includes, first of all, a visual inspection of the recorded data which can be done by using one of the common software packages mentioned in the last paragraph. This first visualization is important to get an overall impression of the quality of the scanned data and to check whether there are any major artefacts, e.g., scanner noise. Such an inspection is most easily done by visual inspection of a time-series movie. This is offered by most of the software packages mentioned

above. The human visual system is good at finding changes between successive images. One example that might be detected during this step, is radiofrequency noise, which shows repetitive patterns on top of the data. On the other hand, head motion appears as a rapid jerk. Besides this visual inspection, also other computational initial quality assurance steps should be performed. These may include calculating the raw signal-to-noise ratio or the mean image intensity (Huettel et al., 2008).

Moreover, the image orientation should also be checked. The check for orientation is important because there are two main orientations used these days, namely the neurological and the radiological orientation. In the neurological orientation image left corresponds to the patient's left whereas radiological convention means that the image's right side is the patient's left. This often leads to problems.

Another issue is about simple slice artefacts. Sometimes it happens that the most of the brain image is fine except for some slices where artefacts are found These scans have to be sorted out in the beginning (Strother, 2006).

2.3.2.2. Head motion and realignment

One of the most important steps when analyzing fMRI data is to get rid of head motion. Even if the subject tries to lie without moving, it is inevitable that the head moves several millimeters. Because of the high resolution of fMRI, this displacement could lead to a voxel being shifted into another voxel. Nevertheless, it should be kept to a minimum, e.g., by using foam pads to fixate the head as much as possible. Another option to prevent head movement is the so-called bite bar. This is a dental mold which the subject has to wedge in between his or her teeth. Such an immobilization of the jaw reduces head movement to a minimum. Furthermore, there is the option of creating a mask around the subject's head. This is in general more tolerated by subjects because it passively restricts head movement instead of requiring active participation of the subjects. Nevertheless, creating such a mask for every single subject is very time consuming and thus, it is generally not done in praxis. A good tradeoff is using vacuum-pack systems. After placing the subject in the scanner, the pack filled with soft beads is fitted around the subject's head and the air is pumped out, which hardens the pack. Such a system combines good motion prevention as well as patient comfort. Nevertheless, it is quite expensive. Hence, a cheaper and easier version of this is the aforementioned use of foam pads, which are just squeezed and then placed around the subject's head. Moreover, it is useful to train the subjects, so that they are used to the scanner environment and can relax more easily.

There are several head motion correction tools but because of the severe impact on the data, a subject is in general excluded if the head motion in any direction exceeds about 5 mm or a rotation of more than 5 degrees in any direction. The reason for this is that the magnetic field is sensitive to the head position. Before starting the functional scan, the field is optimized (called shimmed) for the head position at this instant and hence moving the head leads to inhomogeneities in the magnetic field and thus to a bad data quality. Sometimes, also field maps are used. Such field maps show the actual static magnetic field. It is created by acquiring two images of the signal phase with slightly different echo time (TE). Field maps can also be incorporated into the preprocessing analysis to correct for geometric distortions.

During head motion correction one volume scan is used as reference (this can be any scan, e.g., the first, the middle, or an averaged one) and all the other scans are realigned to this one fixed target scan. Most algorithms use a rigid body transformation. Such a transformation consists of six variables. Three of those are for translations on the three axes (mostly named x, y and z), whereas the other three are for rotations along the three axes (named as pitch, yaw and roll). Such a rigid body transformation is sufficient because the motion of the brain can be fully described by translations and rotations around the three spatial axes. The values of the aforementioned parameters are estimated iteratively. An error measure gives the best goodness of fit. Often, a sum of squared intensity differences of two corresponding volume elements is used as an error measurement. This search is iterated until a minimum of the error measure is found. Nevertheless, the choice of this cost function and the way it is optimized is what differentiates the implementation in the different software packages. What is known, up to now, is that intensity-based cost functions give in general better results than fiducial-marker-based or land-marker-based algorithms (Strother et al., 1994; West et al., 1997). After a minimum of the error measure is determined, the found motion parameters are applied to the source volume by making use of an interpolation method. Such an interpolation creates new values at spatial locations. A tradeoff between speed and residual interpolation error has to be found. The sinc interpolation gives most of the time good results.

Most fMRI preprocessing software packages visualize the time course of the six parameters which can later on be used as confounds in the general linear model (GLM). Nonetheless, one has to keep in mind that a head motion can occur at any moment of a scan. As mentioned above, a scan is not acquired instantaneously and thus, some slices of a scan may be acquired before and some after the head motion. That is why the rigid body model is not totally accurate for fMRI. Figure 13 shows an example of a six parameter rigid body transformation – the time course of the six parameters as well

as a difference image before and after head motion (Huettel et al., 2008; Strother, 2006; Uludag et al., 2015).

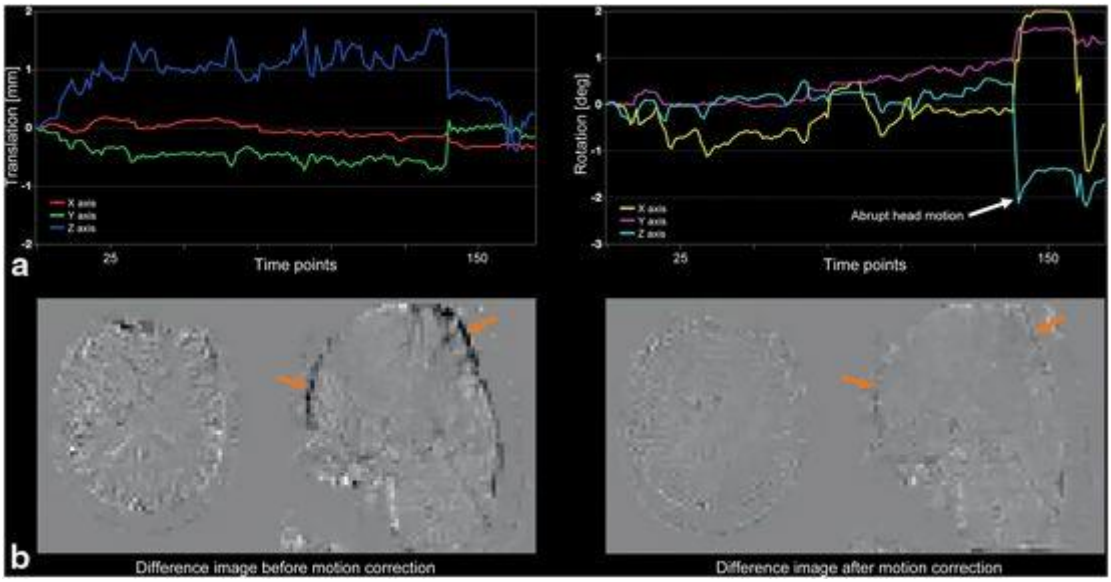

Figure 13: Rigid body transformation **a** *showing the time series of the motion in the three spatial directions x, y, and z, as well as the rotations around the three axes. The white arrow indicates an abrupt head motion.* **b** *difference image from the target to the volume image before and after motion correction. The arrows indicating the improvement achieved by motion correction, namely a reduction in contrast at the border of the brain. (Uludag et al., 2015)*

2.3.2.3. Slice timing

Another very important point to consider is that one volume is not scanned instantaneously but takes a certain time. Hence the voxels in one scan are not scanned at exactly the same time instant. Considering descending or ascending acquisition, the first and the last scanned slice have a time difference of one TR. For interleaved scanning two neighboring slices are TR/2 apart. This is crucial especially in event-related designs, while it is still discussed if it is needed for block design. The aim is to preprocess the data in order to get a scan in which all voxels are scanned at the same time. This procedure is called slice timing because one slice (or in multiband sequences several slices) is recorded at the same time and the other slices have to be brought in accordance to this slice (or these slices). Hence, the time series of the other slices are shifted to a specific time point of the reference slice. This reference slice can be any slice. Most of the time it is the slice acquired at the middle of the time interval. After shifting the time series to the right time points, the series is resampled. During this process data points that have not been sampled in first place, need to be considered. These points are interpolated. The most used algorithms are linear, sinc, or cubic spline algorithms. What is crucial

for this process is the acquisition order. It is possible to acquire the slices either in a descending or ascending manner or in an interleaved manner, which is often done in order to prevent so-called cross-talk between slices. This means that, e.g., all even slices are acquired followed by all odd slices. Otherwise, also the HRF could be shifted. But the above mentioned algorithm is the most frequently used one (Uludag et al., 2015).

There is no clear consensus whether slice timing should be done first or whether realignment should be done first. Huettel et al. proposed some rules which say that slice timing should be done before realignment when having an interleaved slice acquisition with a long TR. On the other hand, realignment should be done first for sequential acquisition or short TRs (Huettel et al., 2008).

2.3.2.4. Coregistration

One of the main aims of researchers is, in general, to find how the activation pattern fits to the neuroanatomy. This is not possible by just looking at the functional scan because its resolution is mostly very poor. Hence, a high-resolution image is acquired. This has to be aligned with the functional image. Figure 14 shows a comparison of structural and functional scans of the same subject of one of our studies. As can be seen, the upper row (structural image) shows high resolution images of the three main views, i.e., coronal, sagittal, and axial. They have high contrast which means all the brain structures can be seen easily. Moreover, it is easy to distinguish gray matter (GM) and white matter (WM) in these images. On the other hand, the second row shows functional images (again coronal, sagittal, and axial view of the same subject). These images seem very blurry and have low contrast. The sulci and gyri that could be easily seen in the structural image can hardly be identified here. Thus, it is necessary to overlay the identified functional activation with the structural high-resolution image, in order to define the exact location of the activation. This procedure is called coregistration.

Even when taking from the same subject, there are always differences in the functional and the structural images. Thus, sometimes not the same slices are acquired, or the subject moved slightly between the two scans. Moreover, the structural image has in general a smaller voxel size. In order to coregister these two images, cost functions using mutual information are most often used.

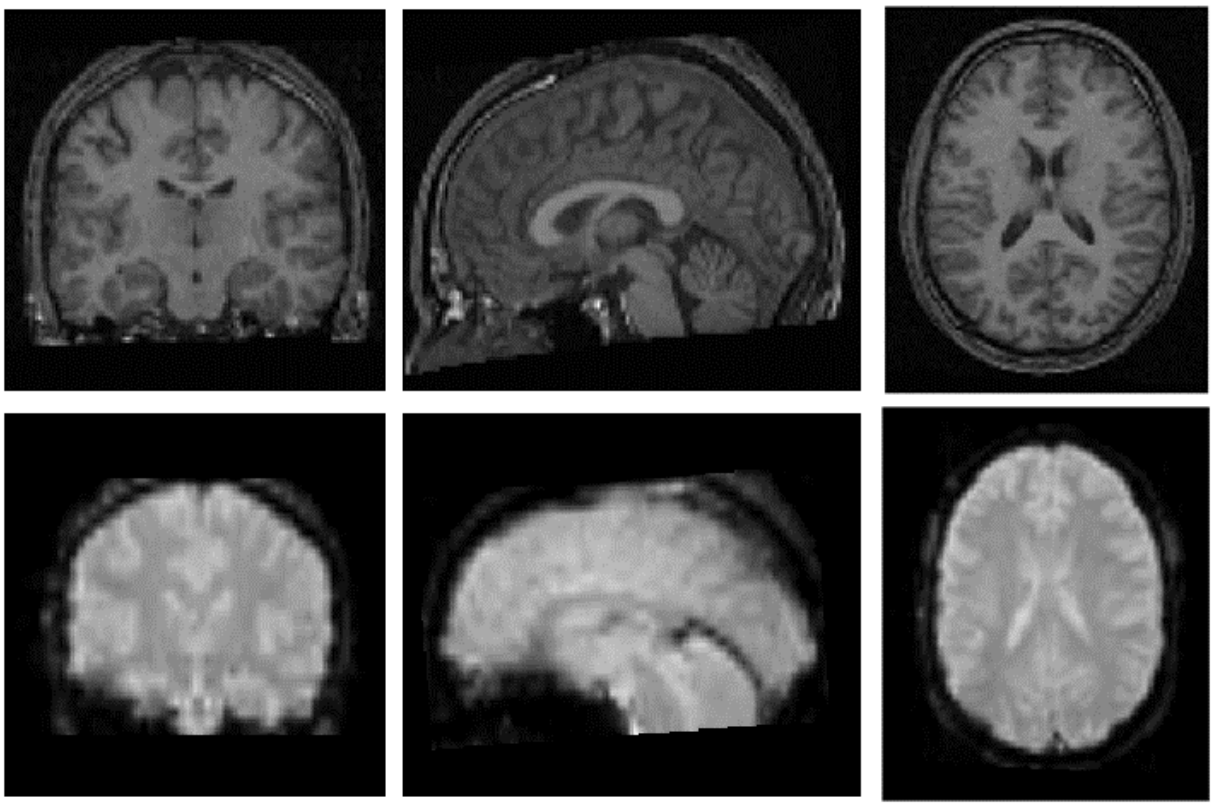

Figure 14: Comparison of structural (upper row) and functional (lower row) data of the same subject from one of our studies.

2.3.2.5. Normalization

The aim of a study is often, not just to find results for one specific subject, but to compare different subjects or to perform a group study which allows generalization to the general population. A normalization step is necessary when comparing different subjects with each other. The brain shape of every person is different like the general body shape. This diversity starts with the overall shape of the brain and goes down to fine-grained cortical folding patterns. Thus, it is not possible to directly compare them. A standard brain is needed for this step. The most common ones are the Talairach (from a single post mortem female human brain) (Talairach and Tournoux, 1988) and the Montréal Neurological Institute (MNI) atlas, which was derived by averaging 305 brains (Evans et al., 1993). Nevertheless, it is also possible to create a reference brain, e.g., an average brain over the subjects included in a specific study.

The Talairach atlas has as origin the midpoint of the anterior commissure (AC). After rotation of the brain, the posterior commissure (PC) is supposed to be in the same axial plane as the AC. The connection of these two points (AC and PC) is the y-axis of that coordinate system. The x-axis goes

from left to right through AC and is orthogonal to the y-axis. The last axis, the z-axis, goes from inferior to superior through AC and is orthogonal to the xy-plane. In order to perform a full Talairach transformation, one creates a cuboid which is parallel to all three axes and encompasses the outer boundary of the cortex. This is further separated by planes into 12 sub-cuboids which are each linearly expanded or shrunken to match the Talairach standard brain sub-cuboid. Altogether, this transformation ensures that the AC and PC are located at the same coordinates in every brain. Furthermore, the sub-cuboids defined by the AC, PC, and borders of the cortex have the same size in every brain. Nevertheless, this does not ensure that same coordinates point to corresponding brain areas in different individuals. This is especially true for cortical regions but not so pronounced for areas close to the AC-PC line (De Martino et al., 2013; Frost and Goebel, 2012).

When comparing the results of the MNI alignment with an intensity driven automatic algorithm, one finds that the result is not much better than that with Talairach, even when using nonlinear spatial transformations. This is because the template brain of the MNI has been averaged extensively and thus has lost anatomical details. It is also possible to directly transform the functional data to the MNI space because also EPI templates exist. However, it is recommended to first coregister the structural and functional data, and then use this transformation for normalization (Uludag et al., 2015).

After a reference brain template is chosen, mathematical methods like stretching, warping, or squeezing are used to transform all other brain images to the reference brain. Hence, the size of the brain is transformed, but also some landmarks like, e.g., major sulci are used for the transformation (the exact landmarks depend on the algorithm used).

Further quite new approaches are the surface-based or cortex-based algorithms. During this approach the brain is inflated to a sphere. Hence, it has just two dimensions, i.e., longitude and latitude, instead of having three dimensions, as in volumetric space. The information of gyri and sulci is preserved indirectly by curvature maps which are calculated prior to inflation. The cortical meshes are aligned by increasing the overlap of curvature information. Thus, it aligns corresponding sulci and gyri across the brains (Uludag et al., 2015). Frost et al. showed that this approach increases the statistical power and spatial specificity of group analyses because it not only increases the overlap of macroanatomical regions but also of corresponding functionally defined specialized brain areas (Frost and Goebel, 2012). Surface-based algorithms are especially good to separate activations which are near in volumetric space but not in neural space, for example, if two voxels on opposite sides of a sulcus are active (Huettel et al., 2008).

Moreover, there is a method, where the functional information is used directly for normalization. Hence, first a standard stimulus is performed in order to help to identify a specific region of interest (ROI) in each subject. These ROIs are later on used to extract specific time courses. This approach seems to be the perfect solution to the problem of correspondence in different subjects. It also allows to detect very small differences in various subjects at group level, even with a high statistical accuracy. The main problem with this technique is to find a suitable localizer experiment. It is also important to notice that this approach just looks at specific brain regions, and thus it can happen that activity in other brain regions are totally overlooked. This can be avoided by a new approach proposed by Frost and Goebel which is an approach integrating whole-cortex macroanatomical and ROI-based functional alignment (Frost and Goebel, 2013). Another approach by Haxby et al. is called hyperalignment and describes a method where subjects watch the same movie and then correspondence between voxels is established (Haxby et al., 2011).

Normalization is an important and useful tool when comparing different subjects, especially for group studies. Nevertheless, one has to keep in mind that all the templates that are used are generally obtained from healthy college-aged neurologically normal subjects. It is known that many other subject groups differ from this group. For example, brains of elderly subjects generally have atrophy, i.e., ventricle enlargement and sulcal widening. On the other hand, children also have different brains, e.g., they have different contrasts due to less myelination. Furthermore, also male and female brains differ. These are all things to consider when performing normalization because it may be possible that normalization masks group differences. Besides these differences for healthy subjects, there are a lot of different brain structures in patients. This may lead to an inaccurate all-over normalization. Because of all the reasons mentioned above, some normalization techniques for subgroups have been developed. Another technique, to avoid all this, is to use subject-based ROI analysis (Huettel et al., 2008).

2.3.2.6. Segmentation

Segmentation describes the separation of the image into different tissue parts, i.e., GM, WM, and cerebrospinal fluid (CSF). This is done because, e.g., sometimes, it is convenient to restrict the activation pattern to the GM areas. Such algorithms use the intensity of different voxels to identify different brain areas. Hence, it is crucial that all these areas have the same intensity. Thus, bias correction is needed and necessary for segmentation algorithms (Smith et al., 2004).

What is also worth mentioning is that a lot of the algorithms for preprocessing work better when the brain is segmented from non-brain tissue, i.e., the scalp and skull.

2.3.2.7. Further common preprocessing techniques

Beside the above-mentioned steps, a lot of different other preprocessing steps are applicable. Nevertheless, these are not always used and sometimes have to be used with caution to not remove signals of interest. Two important ones are temporal and spatial filtering. A filter is a tool that tries to remove uninteresting noise but to keep as much as possible of the signal of interest. It is always a tradeoff and has to be used with a lot of caution to not remove too much of the signal. On the other hand, when used well it can improve the signal-to-noise ratio.

- Temporal filtering

The main aim of temporal filtering is to preserve interesting frequencies while getting rid of frequencies arising from noise. The signal is Fourier-transformed from temporal to frequency space after which a filter is applied. When talking about filtering, one always has to keep the Nyquist theorem in mind. This says that for the maximum frequency, called Nyquist frequency, the following equation holds.

$$2 \cdot \nu_{\mathrm{Nyquisst}} = sampling\ rate \qquad (7)$$

In other words, no frequency higher than 0.25 Hz is present for TR=2s.

When talking about temporal filters, it is, most of the time, more convenient to consider the frequency domain, i.e., the Fourier-transformation of the time domain. Then, we apply the filters in this frequency domain. Three main types of filters are distinguished, namely *low-pass filters*, *high-pass filters*, and *band-pass filters*. A low-pass filter cuts off all the high frequencies whereas low ones stay in the spectrum. A high-pass filter is the opposite of a low-pass filter and thus, cuts off low frequencies and keeps only the high ones. Finally, a band-pass filter is a combination of the before mentioned ones, meaning it cuts off low as well as high frequencies and just keeps a band in the middle range.

There are two main effects that are accounted for when performing temporal filtering. One is the removal of linear and nonlinear drifts, whereas the other is temporal smoothing. There is physiological and physical noise. Hence, time courses of a voxel are often nonstationary. The simplest case is a linear trend. This describes that the signal rises or falls with a constant slope over the entire experiment. If this is not the case, the trend is called nonlinear and is more difficult to correct. These drifts describe slow signal changes. Thus, they can be dealt with by using a high-pass filter. As mentioned above, first the signal is Fourier-transformed to the frequency space where it is filtered using a high-pass filter. After filtering an inverse Fourier transformation is applied to get it back into the time domain. This procedure is shown in Figure 15. The first line of this figure shows the raw signal and a schematic drawing of the frequency space, i.e., the signal after Fourier transformation. In the frequency space we see 3 frequencies belonging to low, middle and high frequency signals. The middle one is the one we are interested in and the low frequency one is the so-called drift, whereas the high frequency signal is noise. The drift can be removed by using a high-pass filter (see row three in Figure 15). After the inverse Fourier-transformation, we do not see the rising trend of the raw signal anymore. This removal of the drift is a crucial preprocessing step because it can essentially improve the statistical analysis of the data. On the other side of the spectrum, there are high frequency fluctuations, which can be considered noise. These high frequency fluctuations are also shown in Figure 15. The purple part in the first row represents this high frequency noise, which can be removed by using a low-pass filter, i.e., a filter removing high frequencies and letting low frequencies pass. In the second row of Figure 15 we see what happens when applying such a filter. Hence, the left-hand side (after inverse Fourier-transformation) has no high frequencies anymore and just shows the middle frequency signal and the low frequency drift. In order to cancel out both high and low frequencies we use in general a band pass filter which cuts off all the low and high frequencies we are not interested in. Such a band-pass filter is illustrated in the last row of Figure 15. This band-pass filter leaves us with the signal we are interested in. Removing the high frequency noise improves the signal-to-noise ratio but it is not recommended for event-related design because it may happen that the onset or width estimates of the responses become distorted. Moreover, one should also keep in mind that temporal smoothing increases the serial correlation between successive time points (Uludag et al., 2015).

Furthermore, one has to be aware of temporal autocorrelation. This describes that the amplitude of a future time point could be predicted by the amplitude of past time points. Hence, preprocessing software uses prewhitening algorithms to get rid of these autocorrelations before doing other preprocessing steps. Nonetheless, it is crucial to estimate the autocorrelation correctly in order to

eliminate it. Another approach, which is used when autocorrelation cannot be estimated well is precoloring. This introduces specific autocorrelations into the datasets (Huettel et al., 2008).

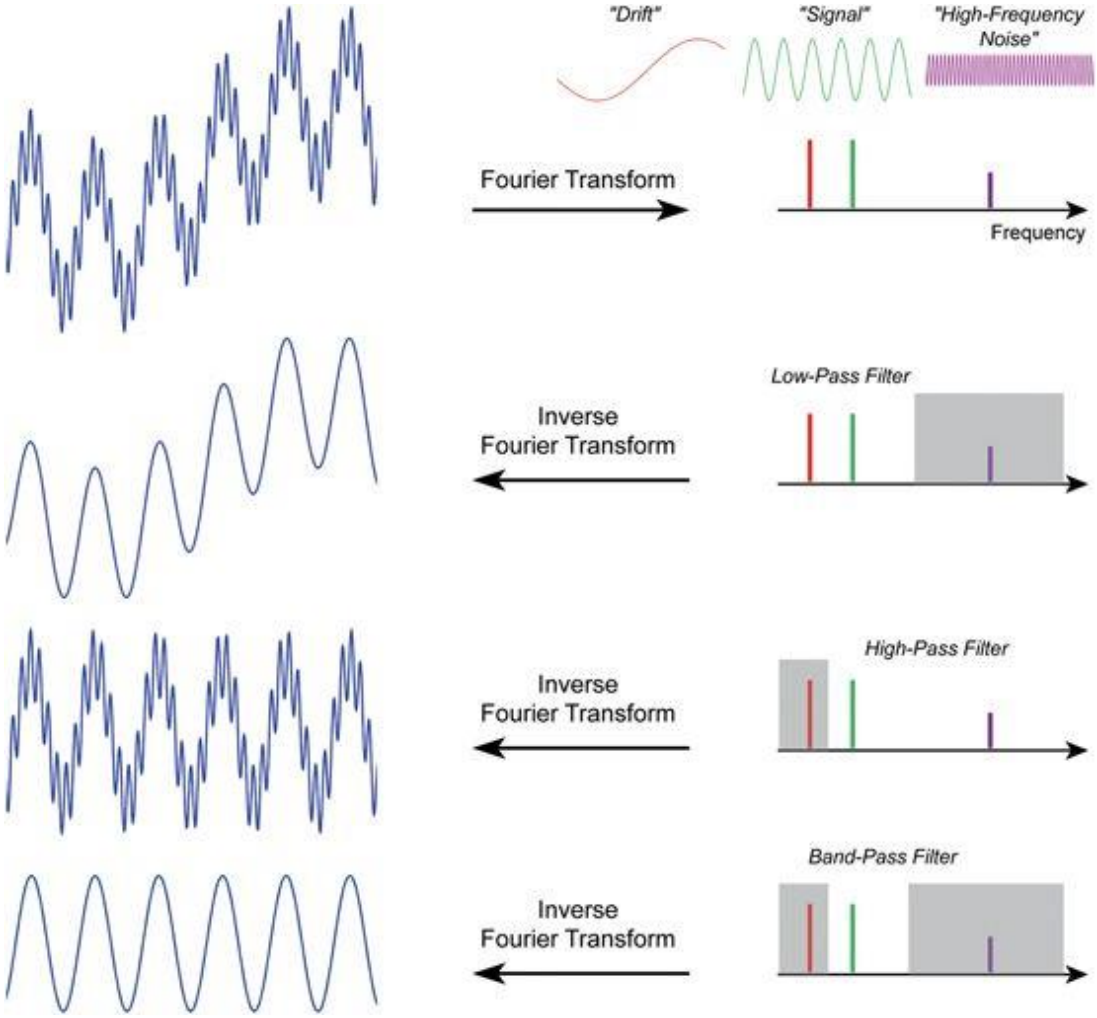

Figure 15: Example of filtering in the frequency domain with the help of Fourier transformation. In the first row on the left-hand side is the raw signal, which then is Fourier transformed. On the right-hand side one sees three frequencies of which the signal is composed. A low one (red), the drift, a middle one (green), the signal we are interested in, and a high frequency one (purple) which is noise. The next three lines show low-pass, high-pass, and band-pass filters and the results when transforming the signal back into time domain via inverse Fourier transformation. (Uludag et al., 2015)

- Spatial filtering

Spatial filtering is sometimes also just referred to as smoothing. When talking about spatial smoothing most of the time we refer to using a Gaussian filter. This is a filter having the well-known bell-shaped Gauss curve. It smears the results over each voxel to his neighbors. The neighboring voxels involved in spatial filtering depend on the size of the kernel, measured in full width half maximum (FWHM).

A larger number includes more neighbors, whereas a small number just includes the nearest neighbors. The biggest advantage is that using a filter of a similar size as the area of the signal of interest gives a better signal-to-noise ratio and is similar to the band-pass filter described in the last section. It increases the signal-to-noise ratio because all fMRI data have a spatial correlation resulting from two main aspects, namely similar functional participation of neighboring brain regions as well as blurring caused by the vascular system. Moreover, spatial correlation is introduced in group studies, where more subjects are compared. The fact that not all brains are equal and that normalization algorithms are not perfect results in activations recorded in slightly different voxels. Spatial smoothing becomes even more important when scanning using higher field strength, e.g., 7 T. Some studies showed that sampling data at higher resolution and then smoothing it gives better signal-to-noise ratio than sampling at the lower resolution. Another advantage of spatial smoothing is related to statistical significance. Because of the fact that a brain consists of a huge number of voxels, there are a lot of tests, which also results in many false positive results during statistical analysis. If the data is smoothed, there are fewer local maxima which are statistically significant. Furthermore, smoothing also improves the analysis by making parameter errors more normal distributed, which is assumed by many statistical tests. These advantages are especially important when dealing with regions with a low signal-to-noise ratio.

The biggest drawback is when the size of the filter does not match the size of the result. Thus, if the kernel is too large, significant results may be missed. This has to be taken into account when focusing on small regions.

The typical FWHM used is about 6 to 10 mm which are about two to three voxels. Nevertheless, also bigger and smaller FWHM are possible. Last but not least, it should be mentioned that such a spatial filtering is important and beneficial just for voxel-wise analysis but does not have any positive effect on ROI analysis (Huettel et al., 2008).

2.3.2. Statistical analysis

For the description in this section we follow (Uludag et al., 2015) Chapter 12 and (Huettel et al., 2008) Chapter 10. See these or similar textbooks for more details and fundamental statistical explanations.

During statistical analysis we aim to find those brain regions which exhibit greater or less response to a specific task when comparing to the control stimulus. One big problem is that there is always

physiological and physical noise which contaminate the signals. Hence, variations between diverse stimuli might just be due to chance. Hence, we need statistical tools to identify those results which did not just occur by chance. One also has to keep in mind that we just measure a sample of the data but want to find results which hold true for the whole population. If it seems very unlikely that a difference between two stimuli is just due to noise it can be seen as a real difference between those stimuli. These are variations we are interested in. When considering single-subject statistical fMRI analysis, the tests are usually performed independently for each voxel's time course, i.e., using a univariate analysis. Independent tests at each voxel raise the probability of finding some statistically significant voxel which just arises from noise fluctuations. Hence, multiple comparative adjustments have to be made.

In Figure 16 one can see a representation of the statistical analysis of the data of two brain regions **a** (left) and **b** (right). One common approach to deal with this problem is simply to subtract the two means, i.e., the mean of the rest condition versus the mean of the stimulus condition. The example shown in this Figure 16, would give the same result in brain regions **a** and **b**. Nevertheless, one has to also consider the noise. Thus, we would generally trust the result in brain region b more than that of brain region a because the former has less noise. Hence, it is important to know something about the noise fluctuation. This can be estimated from the data. The uncertainty of effects can be estimated by integrating the variability of measurements as well as the number of observations.

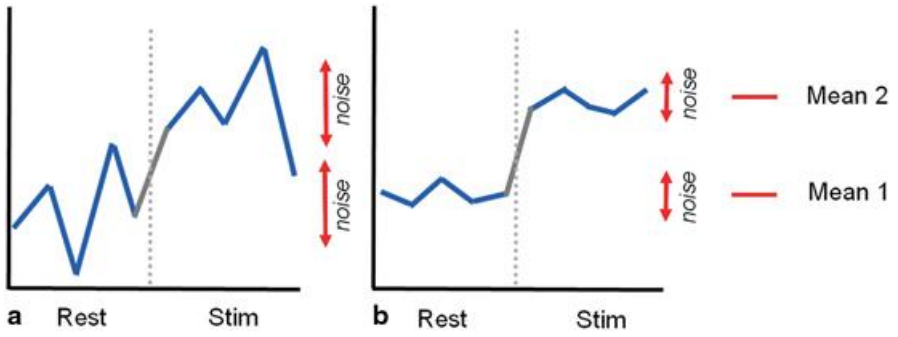

Figure 16: Representation of statistical data analysis for an experiment with two conditions, i.e., rest and stim (=stimulation). **a** *shows a time course for one brain region and* **b** *shows a time course for another brain region. (Uludag et al., 2015)*

Then, the general procedure is to simply formulate a null hypothesis and test for it by using a t-test. As a significance level most of the time a value of $\alpha=0.05$ is used. Nevertheless, a t-test is not always appropriate for fMRI because it does not capture the fall and rise of fMRI responses. Hence, often correlation analysis is used because one can incorporate a gradual increase and decrease of the

measured signal with this method. Each time course of a voxel is compared to the time course of a reference function which could be the expected ideal noise-free time course. This is done by calculating the *correlation coefficient* r given by

$$r = \frac{\sum_{t=1}^{T}(X_t - \bar{X})(Y_t - \bar{Y})}{\sqrt{\sum_{t=1}^{T}(X_t - \bar{X})^2 \sum_{t=1}^{T}(Y_t - \bar{Y})^2}} \quad (8)$$

with T being the number of time points, X_t the reference time course, and Y_t the data time course. Moreover, $\bar{X}$ is the mean of the time series of $X_t$and $\bar{Y}$ is the mean of the time series Y_t. We divide by $\sqrt{\sum_{t=1}^{T}(X_t - \bar{X})^2 \sum_{t=1}^{T}(Y_t - \bar{Y})^2}$ for normalization, i.e., if r = 1 we find that both time series are totally correlated. This means that the one time course goes up when the other also goes up, or down when the other goes down. r = -1 gives us the opposite, namely that one time course goes up while the other goes down, or vice versa. This behavior is called *anticorrelation*. A value of r = 0 indicates that both time courses are not correlated at all.

2.3.3.1. The general linear model

The general linear model (GLM) was introduced by Friston and colleagues (Friston et al., 1994b, 1994a) and is mathematically a multiple regression analysis which is suitable for multiple variables. This is the reason why GLM is the most important tool when it comes to univariate fMRI data analysis. We focus here on the use of the GLM regarding fMRI data, for a deeper explanation see for example (Draper and Smith, 1998; Kutner et al., 2004). It is worth mentioning that in the fMRI literature GLM refers to its univariate version whereas in other fields there are often multiple dependent variables. The dependent variables in such a model are the observed fMRI time courses. The reference functions, i.e., the time courses of the expected and noise-free fMRI signals, are also called *regressors, predictors, explanatory variables, basis functions,* or *covariates*. The time course of the regressor is in general obtained by convolving a box-car function with the HRF. The box-car function is set to 1 when the stimulus is on, whereas it is set to 0 when the stimulus is off. In general, the assumption is made that long stimulation periods can be predicted from known responses to short stimulation. We call the response function of the short stimulus the impulse response function which is in general modelled by two gamma functions (Friston et al., 1998a). Such two functions are plotted in Figure 17. Using appropriate parameters, the combination of $\gamma_1$and γ_2, shown in Figure 17, model the BOLD HRF, which has been observed empirically for short stimuli. The two different functions represent

the two parts of the HRF. The first one, γ_1, represents the shape and the peak whereas the second one, γ_2, gives us the discussed undershot (see Section 2.1.2).

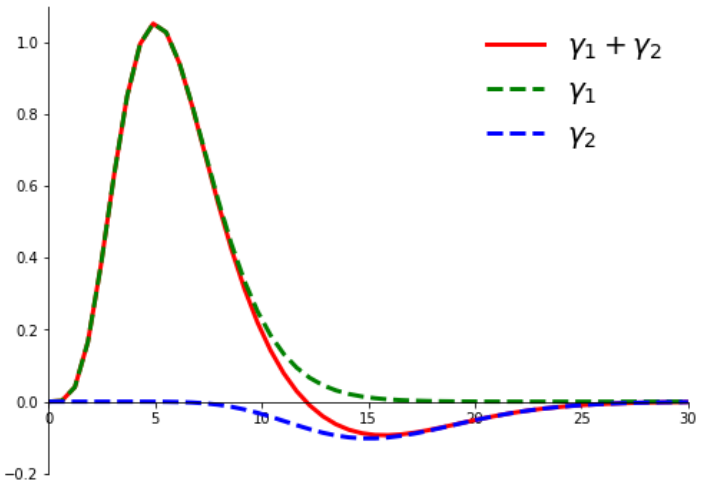

Figure 17: Two gamma functions model the HRF: $\gamma_1(x) = 6x^5 \frac{e^{-x}}{\Gamma(6)}$ *and* $\gamma_2(x) = -x^{15} \frac{e^{-x}}{\Gamma(16)}$. *The first* γ_1 *gives the general shape and the peak and* γ_2 *gives the undershoot.*

When considering a voxel time course *y*, one has to explain the variance. This is done by associating a weight β_i to each regressor time series X_i. Then, the time course of voxel *y* is modeled as the sum of all regressors, each multiplied by its weight β_i, as well as an error term ϵ (also called noise, residuals or prediction error). The GLM system for n data points and r regressors reads as follows

$$\begin{aligned} y_1 &= \beta_0 + \beta_1 X_{11} + \cdots + \beta_r X_{1r} + \epsilon_1 \\ y_2 &= \beta_0 + \beta_1 X_{21} + \cdots + \beta_r X_{2r} + \epsilon_2 \\ &\cdots \\ y_n &= \beta_0 + \beta_1 X_{n1} + \cdots + \beta_r X_{nr} + \epsilon_n \end{aligned} \tag{9}$$

or in matrix notation (the dot representing matrix multiplication)

$$\begin{pmatrix} y_1 \\ y_2 \\ \vdots \\ y_n \end{pmatrix} = \begin{pmatrix} 1 & X_{11} & \cdots & X_{1r} \\ \vdots & X_{21} & \cdots & X_{2r} \\ \vdots & \vdots & \ddots & \vdots \\ 1 & X_{n1} & \cdots & X_{nr} \end{pmatrix} \cdot \begin{pmatrix} \beta_0 \\ \beta_1 \\ \vdots \\ \beta_r \end{pmatrix} + \begin{pmatrix} \epsilon_1 \\ \epsilon_2 \\ \vdots \\ \epsilon_n \end{pmatrix} \tag{10}$$

or simplified as,

$$y = \mathrm{X} \cdot \beta + \epsilon. \tag{11}$$

Hence, *y* gives the voxel time course, i.e., the time course from time point 1 (y_1) to time point 2 (y_2) until time point n (y_n). β_0 gives the baseline and the regressors on the right-hand side of the equation model the time course expected by different stimuli and are scaled by β_i (i=1, …, r). The matrix X is called the *design matrix*. Figure 18 gives a graphical representation of the above equations.

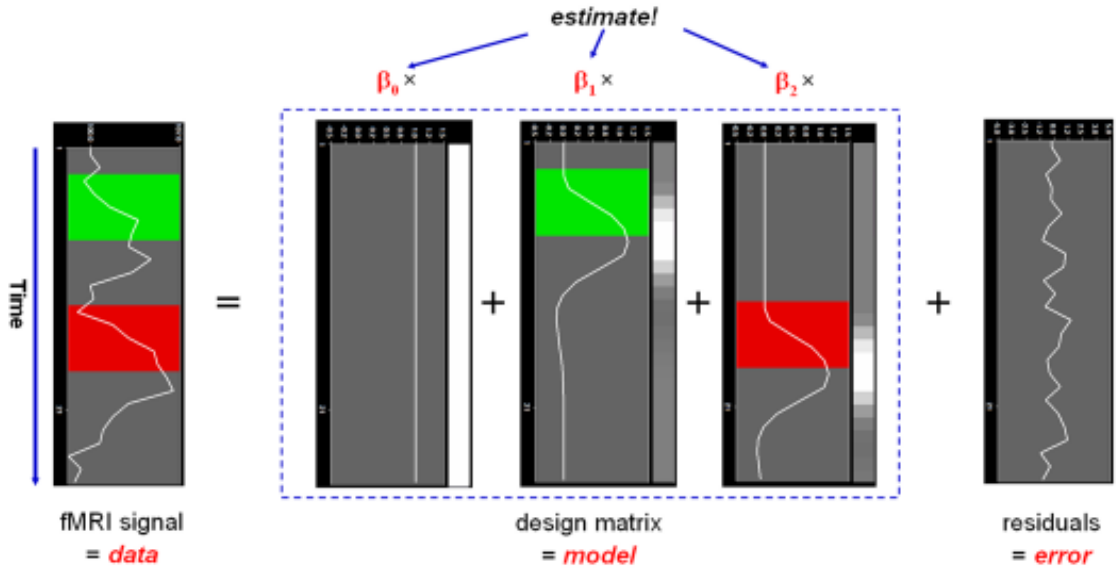

Figure 18: Figure of a GLM. The left-hand side gives the time course of a voxel (time passing from top to bottom. The right-hand side gives the weighted (beta values at the top) design matrix and the error term. The green and the red rectangles symbolize the on-condition in the experiment and the white curve gives the BOLD response. On the right-hand side of each predictor there is a grayscale-ccoded bar indicating the expected responses, i.e., white indicating high response and black indicating no response. (Uludag et al., 2015)

When performing an experiment, we get the data *y* and construct the design matrix *X*. Hence, the GLM serves for finding the beta values, while minimizing the error term. When constructing the design matrix special care has to be taken. If the design matrix is constructed in a wrong way, interesting effects are modeled as errors. In Figure 19 one sees three GLMs fitted to the same data but with different design matrices X. The various models give different results and different errors. The first column on the left-hand side of the figure represents a design matrix that just has a constant term and thus no stimuli. The residuals (top figure) are very high and also include the active phases of the fMRI. In the middle of Figure 19, a design matrix which models the constant as well as one stimulus term is shown. We find that the residuals are lower than in the first case but still include an active term which is not pure noise. The last column shows a design matrix with two active stimuli and a constant term. This is the only case where the data time course and the predicted time course are nearly the same. Moreover, the residuals are very small and just represent real noise and do not include any active phases from the fMRI experiment anymore. Thus, it is crucial to include all

expected effects into the design matrix, also those which are not of direct interest, like motion or drifting parameters. Only in the last case, the error represents real noise fluctuations of physical or physiological origin.

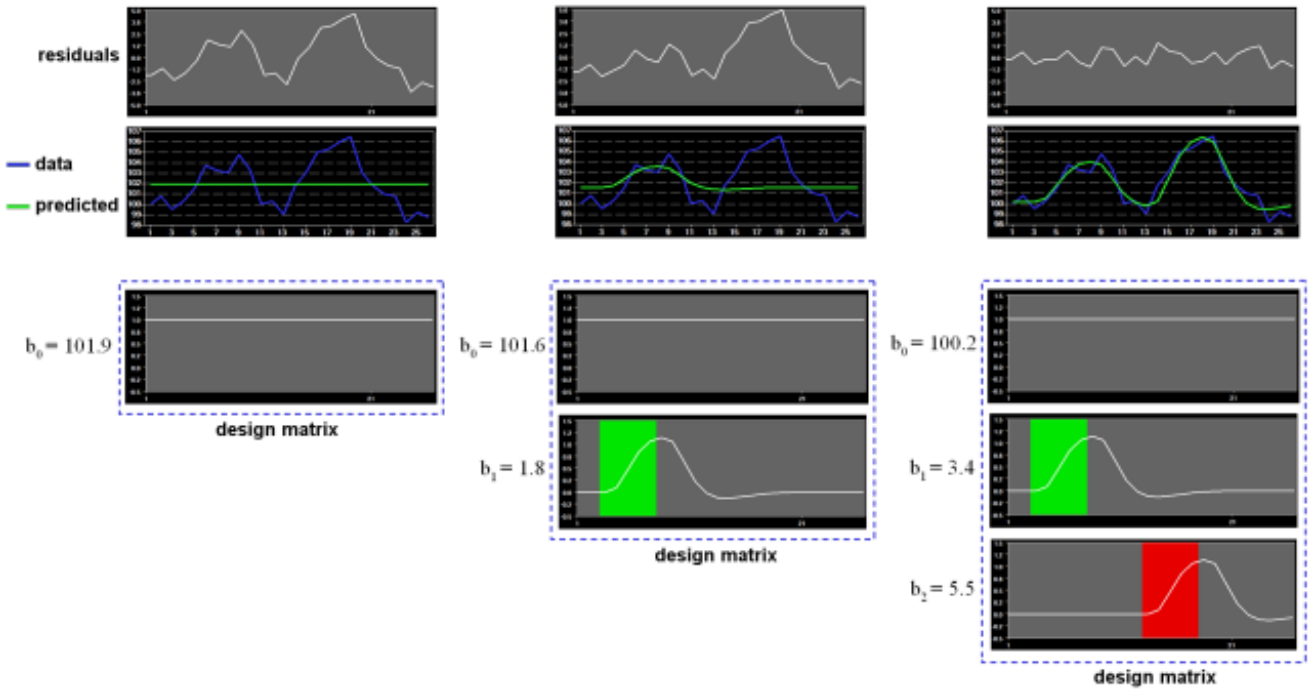

Figure 19: Three different GLMs fitting the same data. The first row shows the residuals, the second one shows the time course of the data (blue), and the predicted time course (green). The other figures show the three different design matrices. The design matrix on the left just models a constant effect. The one in the middle models the constant effects as well as one stimulus, and the one on the right models the constant effect as well as two stimuli. The colored rectangles again represent the onset time for the condition. (Uludag et al., 2015)

Everything described so far was for single voxels. Nevertheless, it also holds true for the entire brain because in general a univariate voxel-wise analysis is performed. Nonetheless, there are some aspects that have to be considered when analyzing the whole brain. A typical fMRI scan consists of several hundred thousand of voxels. Each of the analyses described above is done for every voxel and hence, results of the GLM are also available at each voxel. All these statistical tests are then integrated into a 3D data set, a so-called *statistical (parametric) map*. What is very important is to find an appropriate threshold for those maps. If we consider one voxel, we can use a classical threshold of, e.g., $p<0.05$. On the other hand, if we consider all voxels of an fMRI experiment, we get a massive multiple comparison problem. If we test one voxel with a probability of 0.05, we expect 5% of false positives when repeating the experiment several times. Assuming that there are no real effects in any time course of any voxel, testing spatially in parallel 100000 voxels is, from the point of statistics, equal to testing one voxel 100000 times, i.e., with a p value of 0.05 we expect 5000 false positive voxels.

This is a huge problem in fMRI. Luckily, several methods to control for this massive multiple comparison problem have been presented.

The first one is the *Bonferroni correction,* which is a basic multiple comparison correction approach. It controls the error across all voxels. Hence, it is also called *family-wise error* (FWE). The method yields single-voxel threshold values so that the error probability of 0.05 is reached for the global level. If we assume N independent tests, we get a probability of

$$\mathrm{p_{FWE}} = 1 - (1 - \mathrm{p})^{\mathrm{N}} \tag{12}$$

for one or more false positive results. Thus, for a given $\mathrm{p_{FWE}}$ we have to adjust p as

$$\mathrm{p} = 1 - (1 - \mathrm{p_{FWE}})^{1/\mathrm{N}} \approx \frac{p_{FWE}}{N} \tag{13}$$

with ≈ holding for small values of p_{FWE} (which holds in general). Using this method, we get p=0.0000005 for 1000000 voxels for $\mathrm{p_{FWE}} = 0.05$. This approach would be valid if neighboring voxels would be indeed independent from each other. However, neighboring voxels give similar responses. Hence, the Bonferroni correction is too conservative for fMRI, which leads to a drop in detecting truly active voxels.

Another approach which takes the fact into account, that neighboring voxels activate together was described by Worsley et al. (Worsley et al., 1992). The crucial point is the use of Gaussian random fields which are utilized to describe statistical maps. Nevertheless, this approach requires substantially smoothing the fMRI data which makes it less attractive.

A different way is controlling the *false discovery rate* (FDR) which was described by Benjamini and Hochberg in 1995 (Benjamini and Hochberg, 1995). This method describes all the positive results found that are actually false positives. It is calculated with an iterative approach. This method was introduced to fMRI by Genovese et al. in 2002 (Genovese et al., 2002) and is becoming more and more popular.

3. Severe chronic disorders of consciousness (scDOC)

This section follows partly the description found in chapter 2 of (Zeller, 2017). Over the past decades intensive care medicine as well as modern equipment in this field have improved the chances of surviving severe brain damage (Laureys, 2007; Giacino et al., 2009). The main question is always whether these patients are conscious or not. There is no official and widespread definition of consciousness (Zeman, 2001). The medical definition relies on arousal and awareness (Posner et al., 2007). Moreover, there is intentional behavior which describes the motivation to react intentionally to external or internal stimuli (Goldfine and Schiff, 2011). If the patient has his or her eyes open over a longer period (either spontaneously or after stimulation), it is interpreted as a sign of arousal. This is done more accurately using EEG. Nevertheless, consciousness is missing neuronal marker so that it needs an interaction with the outer world (Owen, 2013).

3.1. Different categories of scDOC

In this subsection we present different diagnoses of scDOC. These are coma, unresponsive wakefulness syndrome and minimally conscious state. Moreover, a definition of locked-in syndrome is given.

3.1.1. Coma

In 1972, Plum and Posner defined coma as a pathological state with severe and permanent disorders of vigilance and consciousness. Such a condition may be caused by severe brain damage (Laureys et al., 2004). It should not be confused with a syncope, delirium, or brain concussion which have a duration of less than one hour. Patients in coma cannot be woken up by any stimulation and do not show any signs of consciousness. An EEG mostly shows long waves in delta and theta bands (Giacino et al., 2009). The prognosis and care of the patient is influenced by various factors, e.g., etiology or age. Traumatic etiologies give in general better prognosis than non-traumatic ones. In general, coma takes two to four weeks. After that period the patient either dies or reaches a higher level of consciousness (Bernat, 2006).

3.1.2. Unresponsive wakefulness syndrome (UWS)

The impairment of consciousness was described as apallic syndrome (AS) (Kretschmer, 1940) and its remission was studied intensively (Gerstenbrand et al., 1963). Jennet and Plum introduced the term vegetative state (VS) for this condition characterized by no intellectual activity or social interaction (Jennett and Plum, 1972). In 1977, detailed results of scientific work were published in the field of AS concerning diagnosis and terminology (Gerstenbrand et al., 1977a; Gerstenbrand et al., 1977c; Mamoli et al., 1977; Peters and Gerstenbrand, 1977), treatment (Gerstenbrand and Lücking, 1977; Zhuber et al., 1977), symptomatology (Gerstenbrand, 1977; Lücking et al., 1977; Scherzer and Gerstenbrand, 1977) and etiology (Avenarius and Gerstenbrand, 1977; Gerstenbrand et al., 1977a; Gerstenbrand et al., 1977b). Currently, diagnostic criteria defined by the United States Multi-Society Task Force on Persistent Vegetative State (The Multi-Society Task Force on PVS, 1994) are widely applied.

The term VS was soon replaced by unresponsive wakefulness syndrome (UWS) (Laureys et al., 2010). It is the first remission phase of coma. Autonomous functions, like the cardiovascular system, breathing and thermoregulation, are starting to work again. Moreover, these patients have a sleep and awake cycle meaning that they have phases when they spontaneously open their eyes and other phases when they close them again. Nevertheless, these patients do not sleep like healthy patients (Cologan et al., 2013) as the EEG shows monotonous and slow waves with closed as well as opened eyes (Bekinschtein et al., 2009; Kobylarz and Schiff, 2005). The occurrence of sleep spindles is a sign for recovering from UWS (Cologan et al., 2013; Urakami, 2012).

UWS is defined (The Multi-Society Task Force on PVS, 1994) as a life

- without evidence of awareness of self or environment, and an inability to interact with others
- without evidence of sustained, reproducible, purposeful, or voluntary behavioral responses to visual, auditory, tactile, or noxious stimuli
- without evidence of language comprehension or expression
- with intermittent wakefulness manifested by the presence of the sleep–wake cycle
- with sufficiently preserved hypothalamic and brainstem autonomic functions permitting survival with medical and nursing care
- with bowel and bladder incontinence
- with variably preserved cranial nerve and spinal reflexes.

3.1.3. Minimally conscious state (MCS)

Another form of scDOC is the MCS which is generally the next stage after UWS when recovering from coma but may also be seen during progressive degradation of neurodegenerative diseases (Giacino et al., 2002). Patients in MCS show one or more signs of consciousness either of themselves or their environment. Such signs of consciousness may be following easy commands, yes/no answers to simple questions, smiling, or crying in response to emotional but not neutral stimuli, grasping towards objects in the field of view or manually manipulating objects given to the patient's hand. Nevertheless, these reactions are typically shown inconsistently. The damage is mostly diffuse axonal with multifocal cortical contusions. Comparing MCS to UWS lesions of the thalamus are found rarely (Giacino et al., 2014).

MCS is defined diagnostically as global impaired responsiveness with limited but discernible evidence of awareness of self and the environment as indicated by the presence of one or more of the following behaviors (McQuillen, 1991; Giacino et al., 2002):

- following simple commands
- gestural or verbal responses to yes/no questions
- intelligible verbalization
- purposeful behavior: movements or affective behaviors that occur in contingent relation to relevant environmental stimuli and which are not simply reflexive movements, e.g.,

    - smiling or crying in accordance to visual or linguistic stimuli
    - answering linguistic content via vocalization or gestures
    - grasping towards objects in the right direction or position
    - touching or holding objects by adjusting to its size or form
    - visual fixation or following as reaction of moving stimuli.

In general, visual following is an early sign for transiting from UWS to MCS (Giacino, 2005). A clear sign of consciousness is following commands, yes/no answering, or understandable linguistic verbalization. In comparison with UWS patients who also cry or smile, MCS patients do this according to appropriate stimuli. All these signs may be fluctuating but at least one has to be reproducible during a clinical examination in order to diagnose a patient as MCS. It is important to keep in mind that

aphasia and apraxia may falsify the results of such an examination and always have to be included into the diagnosis (Giacino et al., 2015).

Recovery from MCS is given if the patient can communicate verbally or via gestures to yes/no questions and can use two objects accordingly (Giacino et al., 2002).

3.1.3.1. MCS+ and MCS-

As the above described group is a very big and heterogenous. Bruno and colleagues proposed in 2011 to distinguish between two subgroups, MCS+ and MCS–. They describe patients who can follow commands and are able to express non-functional communication as MCS+ patients. On the other hand, patients who are able to follow with their eyes, or localize painful stimuli and show contingent reactions to emotional stimuli, like smiling or crying, are defined as MCS- (Bruno et al., 2011b).

3.1.4. Locked-in syndrome (LIS)

The LIS is no disorder of consciousness but can be confounded with such a disorder because patients in LIS have problems communicating. The first to describe this syndrome were Plum and Posner in 1982. They characterized these patients as being incapable of speaking or moving (neither the face nor the body). The only way of communication is vertical eye movement or blinking using the upper eyelid. In extreme cases these patients are not even able to move their eyelids. Nevertheless, they are totally awake and conscious. Moreover, most of their cognitive, sensory, and emotional functions are intact. Especially in the first few months after brain damage it is often misdiagnosed as UWS or MCS (Majerus et al., 2005; Posner et al., 2007). In 1995, the American Congress of Rehabilitation Medicine described the LIS as a neurological impairment which is characterized by open eyes, quadriplegia or quadriparesis, aphonia or severe hypophonia, as well as resisting cognitive functions.

Bauer, Gerstenbrand, and Rumpl (Bauer et al., 1979) distinguished three types of LIS:

- Classic LIS: These patients suffer from quadriplegia and aphonia but can move their eyes vertically and are able to blink.
- Incomplete LIS: These patients can move parts of their body besides their eyes and eyelids.
- Complete LIS: These patients cannot move anything – not even their eyes or eyelids.

Most of the time the acute LIS is caused by a stroke. There are often bilateral ventro-pontine vascular lesions in the brainstem with disconnections of the corticospinal and corticobulbar tracts (Plum and Posner, 1972). Other causes may be different neurological diseases like infections, central pontine myelinolysis or hypo- or hyperglycemia (León-Carrión et al., 2002). A slowly progressive form of LIS can be found in progressive diseases of motoneurons like amyotrophic lateral sclerosis (ALS) (Birbaumer et al., 1999; Birbaumer and Schmidt, 1999; Bruno et al., 2008; Sorger et al., 2009). The mortality in acute state is very high. Nevertheless, there are cases where patients lived up to 20 years in a stable state of LIS (Laureys et al., 2005; León-Carrión et al., 2002). These patients are the ones benefiting most from so called brain-computer interfaces (BCIs) or brain-machine interfaces (BMIs). This kind of devices works just with brain activity and is able to translate it into communication or for controlling other devices for the patient (Birbaumer et al., 1999; Chatelle et al., 2012; Kübler et al., 2009; Lulé et al., 2013; Naci et al., 2012). The LIPS is a newly defined form which is a combination of the above two forms of LIS and scDOC (Seidl et al., 2013).

3.1.5. Summary of the different stages of consciousness

Summing up, one can say that there are many different categories of scDOC which are partly overlapping. Another way to describe the different stages of consciousness is via awareness and vigilance. Awareness stands for the level of contents of consciousness whereas vigilance describes the awake behavior, i.e., for example open eyes. Figure 20 from Boly at al. (2013) gives an overview of the different stages of consciousness as well as other stages of differing consciousness. One finds that coma is indicated by a low level of awareness and vigilance, which is similar to general anesthesia. UWS (in the figure Vegetative state) shows a high level of vigilance and a low level of awareness, namely the patient appears to be awake but does not have any signs of being aware neither of himself nor of the environment. In this figure, MCS is slightly above UWS, i.e., the level of vigilance of MCS patients is the same as that of UWS patients but the level of awareness is slightly higher. Hence, MCS patients show, as described above, some signs of awareness. The state conscious/wake is shown in the upper right corner, i.e., a normal conscious person has a high level of awareness as well as arousal. locked-in syndrome is shown close to conscious/wake because these patients are fully conscious like a healthy person – they just cannot move their bodies. Moreover, this chart shows stages of sleep which are located along the first median from slow wave sleep to drowsiness. This shows that both the level of awareness and the level of vigilance become lower, the deeper we sleep.

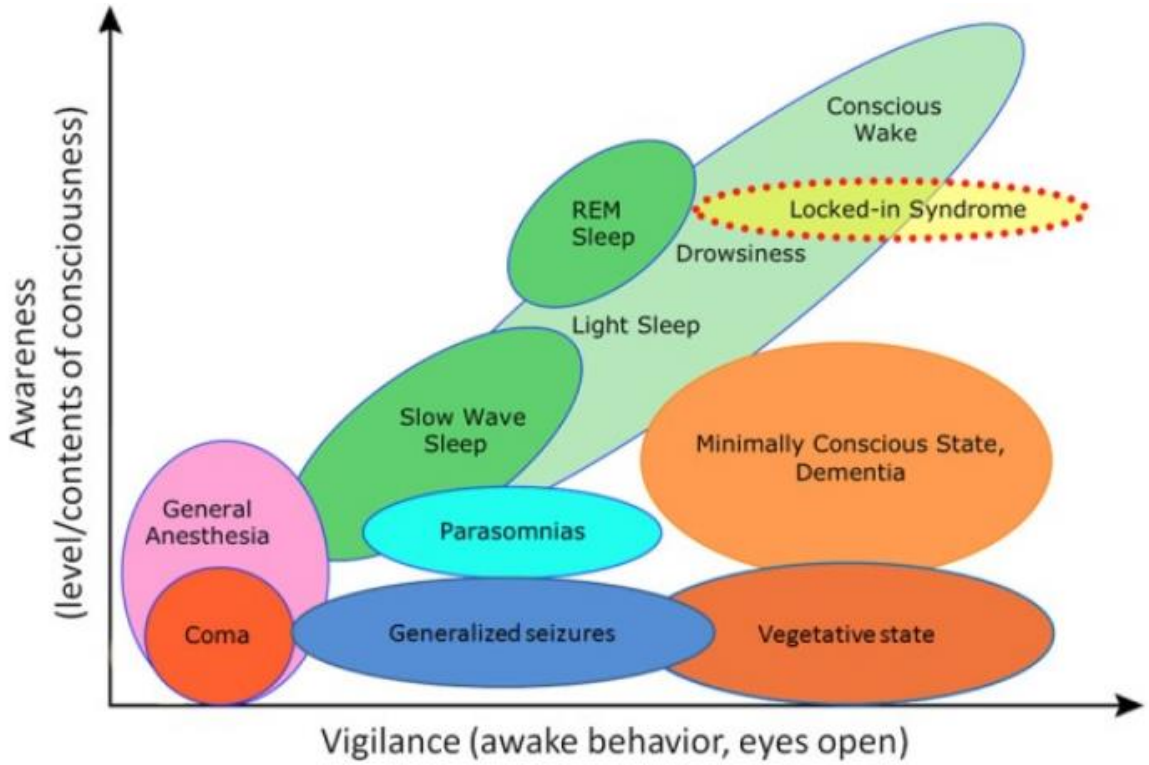

Figure 20: Different stages of consciousness with respect to awareness (y-axis) and vigilance (x-axis). Coma and general anesthesia are found near the origin of the coordinate system because they both have low awareness and vigilance. On the other side, Conscious/Wake is found in the upper right corner showing a high level of both awareness and vigilance. UWS (Vegetative state in the figure) is shown on the right-hand side, i.e., it has a high level of vigilance but a low level of awareness. MCS is located slightly above UWS representing a higher level of awareness. (Boly et al., 2013)

3.2.Behavioral testing

There are still no clear physiological markers for consciousness so that the diagnosis of patients with scDOC relies on behavioral testing. There are a lot of different scales and criteria for the diagnosis of these disorders. Hence, in 2010, Seel and colleagues (Seel et al., 2010) choose 13 different diagnosis procedures in order to evaluate the content, standardization, psychometric features and clinical applicability. They especially evaluated the scales for

- differentiation between UWS, MCS, and remission of MCS
- interrater and retest reliability
- validation of diagnosis, and
- prognosis of functional remission.

The scales included were (in alphabetical order)

- Coma/Near-Coma Scale CNC (Rappaport et al., 1992)
- Coma Recovery Scale-Revised CRS-R (Giacino et al., 2004)
- Comprehensive Levels of Consciousness Scale CLOCS (Stanczak et al., 1984)
- Disorders of Consciousness Scale DOCS (Pape et al., 2005)
- Full Outline of UnResponsiveness Score FOUR (Wijdicks et al., 2005)
- Glasgow-Liege Coma Scale GLS (Born, 1988)
- Innsbruck Coma Scale INNS (Benzer et al., 1991)
- Loewenstein Communication Scale LOEW (Borer-Alafi et al., 2002)
- Sensory Modality Assessment Technique SMART (Gill-Thwaites, 1997)
- Sensory Stimulation Assessment Measure SSAM (Rader and Ellis, 1994)
- Swedish Reaction Level Scale-1985 RLS85 (Stålhammar et al., 1988)
- Wessex Head Injury Matrix WHIM (Shiel et al., 2000) and
- Western Neuro Sensory Stimulation Profile WNSSP (Ansell and Keenan, 1989).

Of the above mentioned CNC, CRS-R, DOCS, SMART, SSAM, WHIM, and WNSSP have been found acceptable with CRS-R being the only one that fulfills all criteria of the Aspen Workgroup (Giacino, 2004; Giacino et al., 2002). On the other hand, the scales CLOCS, FOUR, GLS, INNS, LOEW, and RLS85 are at the moment not recommended by Seel and colleagues (Seel et al., 2010).

In the following we will focus on the scales that are most commonly used nowadays. These are the Glasgow Coma Scale (GCS) , which had not been investigated by Seel and colleagues, and the CRS-R.

3.2.1. Glasgow Coma Scale (GCS)

The GCS is the golden standard in the acute medicine and intensive care. It was published by Teasdale and Jennett in Lancet in 1974 (Teasdale and Jennett, 1974). The scale is so popular because it is easy and quick to perform. It measures whether the patient shows responses via their eyes, or verbal or motor signs to external stimuli. The best reactions are given a point which are added up in the end. The highest grade is 15. A total number of under 8 points indicates that the brainstem is not intact. There is also a lot of criticism on this scale especially because it is not able to distinguish between UWS and MCS (Laureys, 2006; Laureys and Tononi, 2008; Teasdale and Jennett, 1974).

3.2.2. JFK Coma Recovery Scale-Revised (CRS-R)

The JFK Coma Recovery Scale was first developed in 1991 at the JFK Johnson Rehabilitation Institute (Giacino et al., 1991). In the year 2004 this scale was revised (Giacino et al., 2004). The scale consists of 23 items which are categorized into six subscales and investigate audio, visual, motor, and oromotor functions, as well as the ability to communicate and arousal. See Table 4 for a full representation of all 23 items.

*Table 4: JFK CRS-R, * denotes MCS, ** denotes emergence from MCS. (Giacino et al., 2004)*

AUDITORY FUNCTION SCALE	OROMOTOR/VERBAL FUNCTION SCALE
4-consistent movement to command *	
3-reproducible movement to command *	3-intelligible verbalization*
2-localization to sound	2-vocalization/oral movement
1-audotory startle	1-oral reflexive movement
0-none	0-none
VISUAL FUNCTION SCALE	MOTOR FUNCITON SCALE
	6-functional object use **
5-object recognition *	5-automatic motor response*
4-object localization: reaching*	4-object manipulation*
3-visual pursuit*	3-localization to noxious stimulation*
2-fixation*	2-fexion withdrawal
1-visual startle	1-abnormal posturing
0-none	0-none/flaccid
COMMUNICATION SCALE	AROUSAL SCALE
3-oriented**	3-attention*
2-functinal: accurate**	2-eye opening without stimulation
1-non-functional: intentional*	1-eye opening with stimulation
0-none	0-unarousable

The lowest points are equal to reflexes. On the other end, the highest points are given to behaviors which need cognitive processing. What is especially important for this scale is the consistence and retest ability. Hence there is a baseline examination followed by retesting of the same item. This guarantees with high security that the behavior is not just caused by reflexes (Giacino et al., 2004). Moreover, this scale is especially useful when testing whether a patient is in UWS or MCS. Hence, a

fixation lasting longer than 2 seconds leads to a diagnosis of MCS (Schnakers et al., 2006). Most of the time signs of the patient being in MCS are shown in the visual subscale. The next is the motor subscale whereas finding non-reflexive behavior via the oromotor subscale is seldom (Estraneo et al., 2015).

Schnakers and colleagues compared the scales of GCS, CRS-R, and FOUR. 60 patients were investigated. The GCS found that 29 where in UWS. The FOUR found four of these patients to be in MCS, whereas the CRS-R even found seven more patients to be in MCS (Schnakers et al., 2006). This indicates that the CRS-R is the most sensitive scale of these. This is of special importance for the patient because a wrong diagnosis can be devastating.

3.2.3. Limits of behavioral testing

When investigating patients with scDOC, most of the time consciousness is set equally to behavior but this is just an indirect measure of consciousness. In clinical assessment consciousness is seen as the adequate behavior according to external stimuli. Thus, consciousness without adequate behavior is not detected in clinical praxis. This fact leads to a lot of misdiagnosis. In 1976 Teasdale and Jennet investigated the misdiagnosis rate between conscious and unconscious patients and found that one out of five diagnosticians gave a wrong diagnosis (Teasdale and Jennett, 1976). In 1991, Tresch and colleagues found that 18% of patients who were diagnosed as UWS were able to communicate with a trained investigator (Tresch et al., 1991). In 1993 Childs and colleagues investigated 193 patients being diagnosed as UWS and found that 37% were in MCS (Childs et al., 1993). Another study done in 1996 by Andrews and colleagues found that 43% of 40 patients diagnosed as UWS were misdiagnosed. 70% of these could spell messages, over 60% were even abele to perform simple calculations and were oriented with regard to time, place, and person. Moreover nearly 90% were able to give preferences when it came to quality and every day life. Some of these patients have been diagnosed as being in UWS over several years (Andrews et al., 1996). A similar study was conducted in 2004 when 45% of 60 patients were found to have signs of consciousness (Gill-Thwaites and Munday, 2004). In 2006, Schnakers and colleagues found inconsistent diagnoses because of the use of different diagnostic tools at different sites (Schnakers et al., 2006). The misdiagnosis rate is also nowadays about 40% (Schnakers et al., 2009). A new study from Russia, which was conducted in 2017, even found that about 55% of UWS and 80% of MCS patients are initially misdiagnosed (Legostaeva et al., 2017). Moreover, also LIS is often misdiagnosed as UWS or MCS (Bauby, 1998; León-Carrión et al., 2002; Majerus et al., 2005; Ostrum, 1994). Nevertheless, a misdiagnosis can also be made the other way around. Hence automatic reflexes are misinterpreted as conscious reactions

(Majerus et al., 2005). The reasons for this may be that stimuli reach the subcortical centers and are processed there without reaching the cortical centers. Even if using standardized and structured diagnostic tools there are still some confounding factors. Some of these are for example fluctuation of consciousness, sensory or motor deficits, or side effects of medication (Bekinschtein et al., 2009; Candelieri et al., 2011; Giacino et al., 2009). Up to now there are no national or international consistent diagnostic tools. Hence, the quality of the diagnosis varies a lot according to the investigation sites (Coleman et al., 2009).

3.2.4. Summary of behavioral testing

Despite all these problems, there are some clear signs for different stages of consciousness. Recovering from coma is marked by reflex movements and opening of the eyes. Remission from UWS into MCS is marked by oriented movements and command following, while recovery from MCS is marked by functional communication and functionally usage of objects (Bruno et al., 2011a). Nevertheless, these do not take into account deficits, like aphasia, agnosia or apraxia, which are often found in this patient group (Schnakers et al., 2015). If these or other deficits are noted, the total score of the coma scale cannot be reported. Besides the above-mentioned issues there are also other factors interfering with a right diagnosis like the compliance of the patient, unexperienced diagnosticians, or the time taken for diagnosing. Of these the last one is the most severe one because the patient is not always at his best consciousness when being assessed (Andrews et al., 1996; Candelieri et al., 2011). Hence, it is advised to use an interdisciplinary team, different diagnosticians, medical and physiotherapeutic interventions, and to include relatives for the diagnosis of these patients (Gill-Thwaites, 2006).

4. Experiments under anesthesia

4.1.Case report 1: MCS patient

4.1.1. Introduction to case report 1

As mentioned before, emergency treatment and intensive care have improved in the last years, which results in more people surviving severe brain injuries (Giacino et al., 2009; Laureys et al., 2006). However, not all of those patients totally recover and some stay with scDOC whose diagnosis is still challenging (see Section 3 for details). Neuroimaging tools like PET, DTI, or fMRI have been gaining more importance for the diagnosis and prognosis of scDOC in the last decades. This is because it was found that some patients do not show any signs of consciousness when they are tested behaviorally, but indeed show signs of consciousness when using imaging techniques for the examination (Gosseries et al., 2014). Studies on patients with scDOC using fMRI have been published and interesting and promising results have been found. For example, Staffen et al. reported on a patient in persistent vegetative state (another term for UWS) who showed clear responses in fMRI when hearing his own name in comparison to someone else's name. Owen and colleges detected awareness in a patient who was diagnosed as VS using fMRI (Di Perri et al., 2014; Monti et al., 2010; Owen et al., 2006; Staffen et al., 2006; Vanhaudenhuyse et al., 2010).

When focusing on the clinical practice one will experience that sometimes it is very challenging to examine patients with scDOC. Some of these patients develop various movement disorders, such as parkinsonism, myoclonus, chorea, rigidity, dystonia, seizures and status epilepticus which may overlay and contaminate the clinical examination and moreover make high quality imaging nearly impossible because of too large movement artefacts (Venkatesan and Frucht, 2006). Huang et al. examined patients with scDOC as well as subjects under anesthesia. They found that signal synchronization as well as temporal variability of spontaneous brain activity are changed in similar ways in the two groups (Huang et al., 2016). However, they did not anesthetize patients with scDOC. Hence, up to now it is not fully understood in which way narcotic drugs affect the BOLD activity in these patients or whether it is even possible to find BOLD activity in this patient group when anesthetized. Different anesthetics have different effects on the brain. Dueck at al. have shown that the use of Propofol decreases the BOLD response (Dueck et al., 2005). This finding makes Propofol

useless for our experiment because such a decrease could lead to false negative findings when investigating the response of patients with scDOC, i.e., if we do not find any activity in a specific brain region it is not clear whether this is because there is indeed no brain activation or whether this is due to the decrease of the BOLD effect caused by the anesthetic drug. On the other hand, there is Sevoflorane. It has been shown that low concentrations of Sevoflorane enhance BOLD signals, i.e., it is easier to detect brain activity which at first sight may seem useful to us, but one has to keep in mind that this may lead to false positive findings in our experiment. Hence, we decided to keep the Sevoflorane concentration at about 0.75 minimum alveolar concentration (MAC) which is most appropriate according to Marcar and colleagues (Marcar et al., 2006).

The next challenge was to find a suitable subject for our experiment. In the following a case study on a patient in MCS or Remission Phase II on the Modified Innsbruck Remission Scale (Gerstenbrand et al., 1977; Giacino et al., 2002) will be described. The patient described had complex sudden tonic extension and flexion movements of legs and arms. Moreover, sudden tonic opisthotonic retroflexion of the trunk and head, which lasted for several seconds, occurred. Thus, it seemed impossible to perform an fMRI investigation on this patient unless the patient was put under anesthesia.

4.1.2. Clinical Case of the MCS patient

In September 2012, a 16-year-old boy was admitted to the Christian Doppler clinic in Salzburg after near-drowning and cardiopulmonary resuscitation. He suffered from hypoxic encephalopathy and showed initially a full picture of an AS and remained after three months in an early remission state I – II according to the Innsbruck Remission Scale, fulfilling the criteria of an MCS according to Giacinio et al., (Gerstenbrand et al., 1977; Giacino et al., 2002). Three years later (November 2015) he was brought to our center for reevaluation of his status. In the following an overview of his clinical status is given.

The patient could perform gaze fixation and following. He was partially conscious. Hence, he demonstrated cognitively mediated behavior. This behavior occurred, however, inconsistently but reproducibly. Moreover, it sustained long enough so that it could be differentiated from reflexive behavior. In case of simple commands and appropriate environmental stimuli he blinked or moved a finger which was not merely a coincidental behavior. Furthermore, the patient seemed to be – at least partly – aware of himself and the environment. Nevertheless, verbal or gestural yes/no responses or reasonable verbalization were not possible. Moreover, the patient also smiled and cried appropriately in response to emotional visual or linguistic content, but not to neutral topics or stimuli. He also

showed no vocalizations or gestures in direct response to the linguistic content of questions. Besides, the patient was able to reach for objects and there was a clear relationship between object location and his direction of reach. Furthermore, he demonstrated pursuit eye movement and sustained fixation which was found in direct response to salient stimuli or motion. The patient also had a spastic tetra paresis with long tract signs as well as a positive Babinski sign on both sides due to a cross sectional injury of the medulla. Muscle reflexes in all levels were found to be hyperreflexive. Moreover, the patient showed a directed and adequate reaction to painful stimuli on all extremities. He was in a decerebrate posture with extension of the lower and flexion of the upper extremities. The patient showed bilateral spastic contractures in the ankle and wrist. Furthermore, choreatiform and athetotic paroxysmal ballistic movements of arms, legs, and trunk occurred. Besides, he was provided with a tracheostomy, a urine catheter, and percutaneous transdermal gastric probe. His bowel function was spontaneous and occurred every three to four days. Moreover, he had a myelopathy C4 to T1 with additional transverse spinal cord syndrome. Besides, the patient had a burst fracture of C6 and C7 and spinal fusion C4 to T2. He also showed symptomatic epilepsy with complex focal as well as secondary generalized seizures (Wutzl et al., 2018).

An MRI scan was also performed while the patient was under anesthesia. A severe hypoxic encephalopathy with pronounced outer and inner cerebral atrophy was seen. Furthermore, the scan showed extensive post hypoxic gliosis, cortically and sub cortically. This was especially found frontally and parieto-temporo-occipitally within both hemispheres but with a preponderance on the left hemisphere. Moreover, post hypoxic signal changes were seen in the corpus callosum and on both sides in the basal ganglia. Signs of a Wallerian degradation occurred in the brainstem. However, no signs of diapedesis of the liquor could be seen. In comparison to the initial MRI scan which was taken in October 2012 deterioration of the findings was seen. Thus, increase of the outer and inner brain atrophy and also a rise of the post hypoxic signal changes in the left as well as in the right hemisphere were observed. In Figure 21 slices of the MRI scans are shown. The subfigures are all axial T2-weighted images which are shown in radial convention. a) and b) show the time of the onset whereas c) and d) show the state when the experiment was performed. What can be seen is that at the onset there were global cortical hyperintense signal changes in both hemispheres which were due to hypoxic brain damage which also lead to cortical laminar necrosis. Nevertheless, no brain atrophy could be detected. Moreover, also subcortical hyperintense signal changes occurred within the basal ganglia of the right as well as the left hemispheres which were due to hypoxic brain damage. The MRI at the time point of our experiment showed global cortical and subcortical WM hyperintense signal changes in the right as well as in the left hemisphere which were due to hypoxic brain damage.

Furthermore, three and a half years post onset it was possible to detect extensive brain atrophy within the MRI image. Besides, extensive enlargement of the third as well as both lateral ventricles was found (Wutzl et al., 2018).

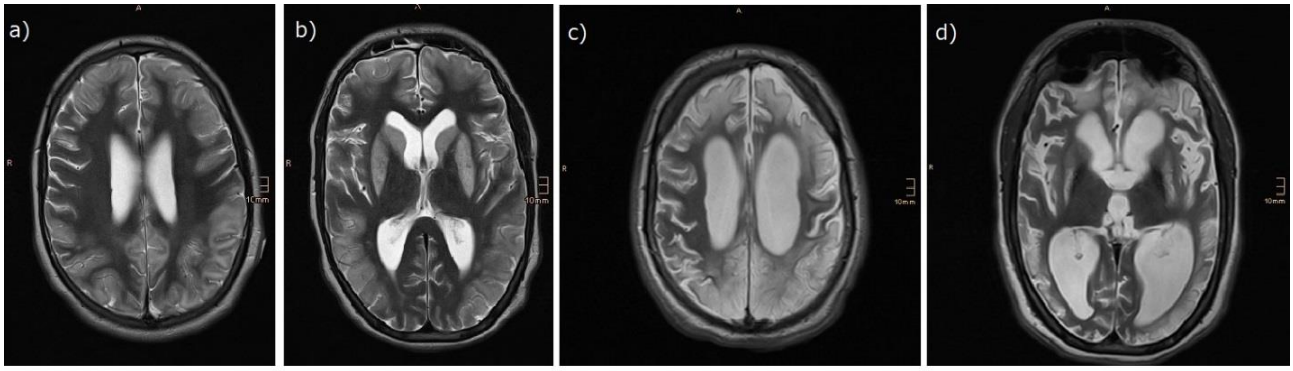

Figure 21: Shown in radiological convention: a) MRI at onset: axial T2-weighted image showing global cortical hyperintense signal changes in both hemispheres due to hypoxic brain damage leading also to cortical laminar necrosis. At the time of onset, no brain atrophy can be detected. b) MRI at onset: axial T2-weighted image showing subcortical hyperintense signal changes within the basal ganglia of both hemispheres due to hypoxic brain damage. Again, no brain atrophy can be detected within the MRI image. c) MRI at time point two (three and a half years later): axial T2-weighted image showing global cortical and subcortical WM hyperintense signal changes in both hemispheres due to hypoxic brain damage. Three and a half years post onset extensive brain atrophy can be detected within the MRI image. d) MRI at time point two (three and a half years later): axial T2-weighted image showing global cortical and subcortical basal ganglia WM hyperintense signal changes in both hemispheres due to hypoxic brain damage. Again, extensive brain atrophy can be detected within the MRI image with extensive enlargement of both lateral ventricles and the third ventricle. (Wutzl et al., 2018)

4.1.3. Methods used for the fMRI measurement of the MCS patient

4.1.3.1. The FMRI experiment

The fMRI was performed using a 12-channel head coil on a 3 Tesla Siemens Magnetom Tim Trio machine (Siemens Erlangen, Germany). We performed four functional runs during each of which we focused on one extremity. As paradigm we chose stimulation with expected response in the somatosensory cortex. This was done because such a stimulation is known for its stability and robustness (Rath et al., 2016) which were of special importance. When evaluating whether an examination of anesthetized patients in scDOC was possible, it is crucial to have a good working paradigm. If the paradigm is not robust one may get false-negative results which are just due to a poor choice of the paradigm and not caused by the effects of anesthesia. Hence, a well-trained operator stimulated all four extremities with a brush. A self-paced frequency of about 2Hz was used for the stimulation. He stimulated one extremity per functional run. The locations of the stimulation were the dorsa manuum

and pedum. The experiment started with 6 dummy scans. After that 89 whole brain images were acquired using a T2*-weighted single-shot EPI sequence. The parameters used were: TR 2.2 s, TE 30ms, matrix 64x64, field of view FOV 210mm^2 and flip angle FA of 70°. The first 9 images served as the first block of the resting condition i.e. no stimulation was performed. This first block was followed by four blocks of each 10 images of stimulation alternating with 10 images of rest.

Besides these experiments, a high-resolution anatomical image was also acquired. A 3D magnetization prepared rapid gradient echo (MPRAGE*)* T1-weighted sequence was used. The parameters were: TR 2.3 s, TE 2.91 ms, time of inversion TI 900 ms, 160 slices, slice thickness 1.20 mm, in-plane resolution 1.0 mm x 1.0 mm, generalized autocalibrating partial parallel acquisition (GRAPPA)=2, and FA of 9° (Wutzl et al., 2018).

4.1.3.2. The used anesthesia

As mentioned above (cf. Section 4.1.1), Dueck at al. found that BOLD response decreases with Propofol (Dueck et al., 2005), Hence, Propofol was not a useful drug for our experiment. Therefore, our anesthetist started the anesthesia by letting the patient inhale Sevoflurane until the patient's end-tidal concentration reached 4%. Analgesia was also provided, namely by Fentanyl 0.15 mg intravenously. A laryngeal mask size 5 was inserted. The anesthetist ventilated the patient to end-tidal 36 mm Hg CO2. Based on Marcar's findings anesthesia for fMRI investigation is most suitable with Sevoflurane MAC 0.75. Hence, this is what was used during the entire examination (Marcar et al., 2006). After finishing the experiment, the patient recovered uneventfully from anesthesia (Wutzl et al., 2018).

4.1.3.3. Data analysis

We used one of the most common software for the data analysis, namely SPM8 (http://www.fil.ion.ucl.ac.uk/spm/). During the pre-processing the functional data were first realigned, then unwarped, and co-registered to the structural image. Moreover, the functional data were smoothed using a Gaussian kernel with 8mm FWHM. After pre-processing, the data were analyzed using a GLM. During this analysis, the blocks, during which the patient was stimulated, were convolved using a synthetic HRF. Furthermore, the six parameters of the realignment process were included as covariates. Such covariates correct for head motion. Besides, a high-pass filter (of 128 s) was applied. In order to find significant voxel clusters, each run was analyzed by using a one-sample

t-contrast checking for that were higher during the stimulation with the brush compared to those during the time of rest. The voxel clusters were thresholded for clusters with more than 50 voxels. The p-value for each analysis was thresholded as $p<0.001$, uncorrected (Wutzl et al., 2018).

4.1.4. Results found from the fMRI experiment of the MCS patient under anesthesia

The most important result was the one corresponding to stimulation of the left hand, i.e., this is where the strongest and widest activation was found (see Figure 22b). The result shows an activation pattern in the right motor cortex, namely within the post central gyrus - in other words, in the somatosensory cortex which is contra lateral to the left hand. When comparing this finding to the behavioral testing of the patient, one finds that it was also the left hand which he used to move a lot, especially also for goal-directed activities of daily life. This observation from daily life made us believe that the right motor cortex was intact. On the contrary, the patient did not use his right hand so much and on the MRI it seems as if the left motor cortex is totally damaged (Figure 22a). However, the results of the statistical analysis of the other three extremities, i.e., right hand, left and right foot, did not give any conclusive findings. Actually, this is a result that often occurs when trying to analyze fMRI data of patients with scDOC. Hence, the fact that activation was found in one out of the four stimulated extremities leads to the conclusion that the non-finding in the other three extremities is not directly correlated to the anesthesia but rather to the nature of the data when dealing with patients with scDOC (Wutzl et al., 2018).

4.1.1. Summary of case report 1

FMRI will gain more importance and will play a crucial role in the evaluation of brain function of scDOC patients in the future. Nonetheless, a regular fMRI examination is often impossible when dealing with these patients because of different reasons, e.g., patient movement, autonomic decompensation, spastic contractures, or an intolerable stress burden. Thus, it is more than likely that an investigation under anesthesia will be favored in the future. According to our results presented above, we conclude that an fMRI investigation of patients with scDOC under anesthesia is doable and that at least a somatosensory perception can be detected. Nevertheless, further work has to be done in order to clarify whether other fMRI paradigms also lead to a robust BOLD response in anesthetized scDOC patients (Wutzl et al., 2018).

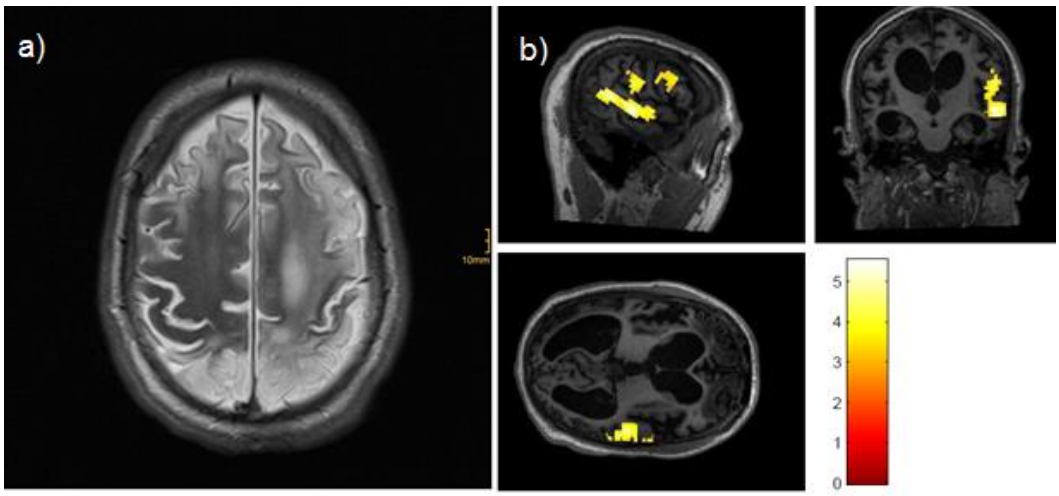

Figure 22 a) Axial T2-weighted MRI shows extensive post hypoxic cortical gliosis, especially frontally and parieto-temporo-occipitally in both hemispheres with a preponderance on the left hemisphere. (Image shown in radiological convention.) b) fMRI of the patient during brushing with a frequency of about 2 Hz onto the dorsum of the left hand- overlaid on an T1 image for visualization. A clear activation of the right motor cortex was found. Color bar indicates t-statistics. (Image shown in neurological convention.) Modified from (Wutzl et al., 2018).

4.2. Case report 2: patient with Creutzfeldt-Jakob disease

4.2.1 Introduction to case report 2

The second case report is about a 62-year old male patient, who had a blunt neurological history. He had the diagnosis of a UWS, via CRS-R, in a rapidly progressive disease which was the Creutzfeldt-Jakob disease (CJD). MRI images showed hyperintensive abnormalities in basal ganglia and cortex. magnetic resonance spectroscopy (MRS) revealed decreased level of N-acetyl-aspartate (NAA) and other metabolites. In order to further investigate the consciousness of the patient, an fMRI investigation was performed. This investigation showed a clear response within the sensorimotor cortex. After this fMRI, the patient lived for three more weeks before he died. The diagnosis of *sporadic CJD* (sCJD) was pathologically confirmed postmortem. Up to now, as far as we know, there are no reports on fMRI for investigating patients with CJD. We report an fMRI investigation of a somatosensory paradigm. A clear BOLD response was found within the sensorimotor cortex. This response indicates that there was still residual cortical function in the final stage of CJD. Hence, for the first time, to our best knowledge, we report results showing persistent cortical activity in the final stage of CJD (Golaszewski et al., in prep.).

4.2.2 Creutzfeldt-Jakob disease

sCJD is a lethal disease which occurs very seldom (de Villemeur, 2013; Gasparini et al., 2013). It is characterized by rapidly progressive dementia, memory loss, as well as motor disturbances. The incidence of sCJD was 1 - 2 : 1 000 000 during the last decades (Ladogana et al., 2005). A reliable diagnosis can just be given postmortem via autopsy. MRI, Diffusion-Weighted Imaging (DWI), EEG, and 14-3-3 protein in the CSF allow to narrow-down the differential diagnosis during lifetime (de Villemeur, 2013; Gasparini et al., 2013). The final state of CJD is believed to be characterized via total absence of cortical functions of the patient, i.e., the patient is in AS. Since the radiologic diagnosis is heavily based on MRI, a short review of the main results of MRI for CJD patients is given in the following.

Many studies of serial MRIs of individuals with CJD as well as retrospective studies have been published. The main consensus is that MRI is useful for premortem diagnosis of CJD. This is especially true for sequences with a long TR, i.e., fluid-attenuated inversion recovery (FLAIR), DWI, or proton-weighted sequences (Schröter et al., 2000). Some classical changes have been found in GM, variable with phenotype of the prion protein and the disease progression (Furukawa et al., 2014; Krope et al., 2011). Four types of CJD are distinguished. The first one is the sCJD, characterized by new abnormal protein folding, which results in proteinaceous infectious particles or prions. The next one is the genetic or *familial CJD*. This form describes the case when a gene mutation, which leads to abnormal protein folding, is inherited. The third form of CJD is called *iatrogenic*. This form results from the transmission of prions, e.g., via transplantation of dura mater of the cornea. The last type of CJD is the new *variant CJD* (vCJD), which is transmitted to humans from cattle suffering from bovine spongiform encephalopathy (de Villemeur, 2013; Sikorska et al., 2012). The different forms of CJD show different changes in the MRI.

First, we consider sCJD which has six subtypes depending on codon 129 of the prion protein gene. Hence, valine and methionine (MM, MV, VV) are distinguished. Furthermore, two pathological isotypes of the prion protein exist, i.e., PrPSc 1 and PrPSc 2. This results in a total number of six combinations, namely MM1, MV1, VV1, MM2, MV2, and VV2. Krope et al. found that the location of the signal hyperintensities are slightly different in these six subgroups (Krope et al., 2011). An MRI, which is suggestive of sCJD, has signal changes in the GM in the basal ganglia (striatum) but also in the thalamus, where one finds the so-called *pulvinar sign*, which describes bilateral pulvinar hyperintensity, or the *hockey stick sign*, which refers to hyperintense signal in the pulvinar and dorsomedial thalamic nuclei bilaterally (Casimiro et al., 2012). Moreover, such an MRI shows

changes in the cerebral cortex, known as *cortical ribboning sign* (frontal, parietal, and temporal lobes, cingular gyrus, hippocampus and insula), and also in the cerebellar cortex (Abdulmassih and Min, 2016; Furukawa et al., 2014; Krope et al., 2011). The lesions in the thalamus and basal ganglia are generally found to be bilateral and symmetric (Schröter et al., 2000), but sometimes also appear asymmetrical (Cammaroto et al., 2015).

Now we turn to the vCJD. This type of CJD has just one subtype known, i.e., Methionin homozygote and PrPSc type 2B (Kobayashi et al., 2005). The pulvinar nucleus of the thalamus appears hyperintensely bilateral and in one third of the patients the striatum is hyperintense (Fukushima et al., 2004; Urbach et al., 2001).

In the past, serial MRI studies of patients with CJD have been made and these have been able to correlate images with pathological cellular changes. In the early stage of CJD, bilateral hyperintensities of the putamen and nuclei caudate were found in T2-weighted images whereas in later stages cortical atrophy is developed and the basal ganglia hyperintensities increase (Hutzelmann and Biederer, 1998). In 2014, Fukushima et al. published their work showing initial hyperintense lesions in thalamic nuclei like ventral lateral, ventral anterior, and lateral dorsal nucleus instead of the pulvinar nucleus. These initial hyperintensities spread later on to the entire thalamus (Furukawa et al., 2014). Another study of serial MRI of a CJD patient showed the progression from bilateral hyperintensity in the thalamus, cortex, and caudate nuclei, two months after the onset of the symptoms, to cortical ribboning, diffuse signal abnormalities, and enlargement of the lateral ventricles, 14 months after the first scan and one week before death. These findings were assumed to be cortical vacuolizations which was pathologically confirmed, namely cellular loss, spongiform changes and hypertrophic astrocytosis (Cammaroto et al., 2015). Moreover, Kulkarni reported that the hyperintensities which can be observed in MRIs at later stages of CJD can also be found (more subtly) retrospectively at early stage MRIs (Kulkarni, 2015).

Comparing the CSF markers like 14-3-3 to DWI findings, Forner et al. stated that the DWI is more specific and also give better predictive values for CJD (Forner et al., 2015).

Furthermore, also MRS has shown to be useful for the diagnosis of CJD. A study conducted with 14 patients with prion disease found, with the help of spectroscopic analysis, a reduction of NAA compared to myo-inositol (mi) in the cerebellum and compared to creatine (Cr) in the striatum and the thalamus, when contrasting patients with the prion disease versus patients without it. The sensitivity was 79% and the specificity was 100% when considering the NAA/mi ratio and the

sensitivity was 100% and the specificity was 73% when considering the NAA/Cr ratio (Lodi et al., 2009). Another study could demonstrate a relationship between NAA/Cr ratio and the duration of the disease; the shorter the disease the lower the NAA/Cr ratio (Kim et al., 2011).

4.2.3 Clinical case of the CJD patient

A 62-year old male was admitted to the Christian-Doppler Clinic with cognitive and psychological degradation. The onset was about five months prior to admission. He had a blunt neurological history and also an unremarkable family history. The first symptoms had been social regression and irritability. After that the patient had begun to have problems finding words and had shown memory deficits, executive dysfunctions, disturbed emotional reactions, behavioral disturbances, as well as disinhibited sexual desire.

The first neurological examination found parkinsonian symptoms with rigidity, an intention tremor at both upper extremities and additional spastic symptoms of the extremities, bulbar muscles, and the trunk. Moreover, a severe ataxia was shown in gait and targeted movements. Myoclonic jerks, namely systemic rhythmic myocloni, including the face and trunk muscles, were seen. Considering frontal signs, perceptive and expressive aphasia, with symptoms of higher brain function disorders such as agraphia and acalculia, was noted. The patient's state of consciousness was awake but reduced.

The state of the patient worsened over the following two months. The myoclonic jerks expanded to the upper extremities, more pronounced on the right side. Furthermore, the patient was found in a stretched position of both legs. He had also flexion of the upper extremities and hence, was confined to bed. The speech problems increased and also understanding problems occurred more often. The patient developed primitive motor reflexes, namely rooting, grasping, and sucking reflex. Moreover, the sexual disinhibition rose which lead to more interest in the genital region. He was still conscious but with disoriented episodes, day-time sleeping, and tiredness.

The patient fell into UWS, diagnosed via the CRS-R, seven months after the first symptoms appeared. He developed spasticity of the extremities with a flexed position, severe oculomotor disturbances and additional signs of rigidity. Moreover, severe vegetative dysregulations were observed. Primitive reflexes of grasping as well as oral tendencies – in form of the Klüver Bucy pattern – were noted. Then, respiratory failure occurred. The patient died eight months after the first onset of symptoms which was four weeks after onset of coma (Golaszewski et al., in prep.).

4.2.4 Paraclinical investigations

An initial CT revealed enlarged cortical sulci but no other abnormalities. A T2-weighted MRI, which was performed one week later, showed minimal hyper intensive signals in the left caudate and right thalamus. Moreover, DWI could detect hypo-intensities, which were a sign of restricted diffusion of all lobes (Kim et al., 2011; Kumaran et al., 2012). MRS presented a decreased NAA/choline ratio (Newey et al., 2013). EEG showed, besides a general slowing, Rademaker's complexes, a left temporal focus and an encephalopathic pattern. 14-3-3 and τ protein were elevated when analyzing the CSF. Single photon emission computed tomography (SPECT) detected cortical malperfusion in parietal lobes, which could not be detected in temporal lobes. Hexamethylpropylenaminooxim (HMPAO) and Ioflupan SPECT could not confirm Parkinson disease or Alzheimer disease. Hence, CJD was suspected.

A post mortem histology revealed immunohistochemical proof of prion protein in cerebellar vermis and cortex. The diagnosis of sCJD was confirmed in the histological examination of the autopsied brain. The brain was 1355 grams and had no specific gross-anatomical changes. However, mild spongiform changes were noted in the basal ganglia, temporal cortex, cerebellum parietal cortex, and thalamus. On the other hand, the frontal cortex, the occipital cortex, and the hippocampal formation showed moderate changes. Moreover, the substantia nigra and the pons were unaffected. Diffuse synaptic deposits in the temporal cortex, the frontal cortex, parietal cortex, occipital cortex, basal ganglia, and cerebellum showed immunohistochemically the presence of pathological prion protein. Mild to moderate neuronal loss was found in the investigated brain regions. Reactive microgliosis and astrogliosis were severe to moderate. Amyloid plaques, α-synuclein-positive inclusions, or neurofibrillary tangles were not present in the immunohistochemical investigation (Golaszewski et al., in prep.).

4.2.5 Methods used for the fMRI experiment for the CJD patient

4.2.5.1 The fMRI experiment

An fMRI was performed one week after onset of coma and three weeks before death. The scan was conducted using a 12-channel head coil on a 3 Tesla Magnetom Trio Tim (Erlangen, Germany). We obtained 110 whole brain images (including 6 dummy scans) during the 3 functional runs with a T2*-weighted single-shot EPI. The matrix was 64x64, FOV 210 mm^2, TR 2200 ms, TE 30 ms and FA 70°. Moreover, a high-resolution MRI was acquired. A 3D MPRAGE T1-weighted image with 160 slices,

slice thickness 1.2 mm, in-plane resolution 1x1mm^2, GRAPPA=2, TR 2300 ms, TE 2.91 ms, TI 900 ms, and FA 9°. As a paradigm we chose again a vibrotactile paradigm (see also Section 4.1.3.1). As seen before, this paradigm also shows responses when scanning scDOC patients under anesthesia. We started and ended each run with an epoch without stimulation. Seven of these rest episodes altered with six vibrotactile stimulation epochs whitch each lasting for 16 s. Further details on the used paradigm can be found in (Gallasch et al., 2006; Golaszewski et al., 2002a, 2002b), (Golaszewski et al., in prep.).

4.2.5.2 The used anesthesia

The patient was unresponsive and suffered from agitation and myoclonic. Hence, the patient was scheduled for fMRI under anesthesia. Moreover, we expected airway difficulties after extubation. This is why the patient was scheduled for fully monitored overnight surveillance. The set-up for the anesthesia followed In's descriptions (In et al., 2011) as well as the infection control guidelines of the Australian government (Australian Department of Health and Aging, 2008). All staff members, who were involved in the examinations, wore face masks with plastic transparent shield visors, liquid repellent gowns, and double gloves. Then, we used non-ferromagnetic standard monitoring (Precess, Invivo corp., Orlando, FL 32826, USA). Non-ferromagnetic plastic laryngoscope, face mask, O_2 flow meter, ventilation bag, stethoscope, and endotracheal tube were of single-use type. Moreover, single-use filters were fit in between the valve and the endotracheal tube. We protected the MRI suitable ventilator (Parapac, Pneupac LTD, Luton LV34BU, UK) against contamination with a plastic overlay. The infusion pumps were ferromagnetic. Hence, they were deposited outside the MRI room with an extended line to 4.5 meters.

Our anesthetist induced anesthesia with Propofol 200 mg and then maintained it with 5.5 mg/kg. This was done because Sevoflorane, another common anesthetic, modulates higher-order connections (Martuzzi et al., 2010). Analgesia was also provided, initially by Fentanyl 0.15 mg and then two repetitive doses of Fentanyl 0.1 mg. Rocuronium 80 mg was used to facilitate intubation. Systolic blood pressure was kept over 100mmHg with an infusion of Phenylephrine 10 mg solved in 500 ml Ringer's solution. The ventilation of the patient was with an FiO_2 of 0.45 to end-tidal CO_2 of 37 mmHg. Moreover, SpO_2 was 99% during the whole anesthesia.

The patient recovered uneventfully from anesthesia. After we finished, we incinerated the whole equipment for anesthesia except the infusion pump and ventilator (Golaszewski et al., in prep.).

4.2.5.3 Data analysis

The preprocessing was done using SPM8 (http://www.fil.ion.ucl.ac.uk/spm/), beginning with head motion correction and unwarping, followed by coregistration of the functional and structural image, and then normalization to MNI space. This was done first by normalizing the structural image and then applying the parameters to the functional data. Finally, the data were smoothed with a Gaussian kernel with FWHM of 8 mm. The fMRI data were analyzed using a GLM. This included also convolving the stimulation epochs with an HRF in block design. Moreover, the six realignment parameters (three from translation and three from rotation) were used as covariates to control for noise due to head movements. A high-pass filter of 128 s cutoff was applied. Furthermore, a movement algorithm (Woods et al., 1993) was also used to control for serial correlations. Then, a one-sample t-test was performed to find the voxels with higher signals during the vibration task when compared to rest, all thresholded with $p<0.005$, uncorrected. We are only reporting clusters that were significant at FWE $p<0.05$ (Golaszewski et al., in prep.).

4.2.6 Results found from the fMRI experiment of the CJD patient under anesthesia

We could find a clear BOLD response in our patient in the final stage of sCJD when using a vibrotactile paradigm. The response found was within the primary sensorimotor cortex SM1 contralaterally to the hand which was stimulated. The responses in the pre- and postcentral gyrus show preserved cortical function in these cortical areas of the patient in the final stage of sCJD. The results of the fMRI investigation can be seen in Figure 23 (Golaszewski et al., in prep.).

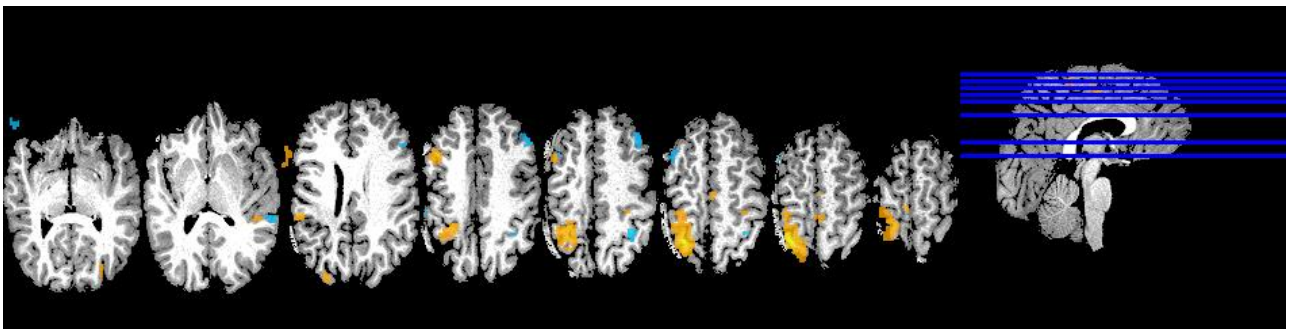

Figure 23: fMRI results of the CJD patient during pneumatic finger vibration. Stimulation was on the right thumb and index finger. BOLD responses are visible in the contralateral primary sensorimotor cortex SM1. (Golaszewski et al., in prep.)

4.2.7 Summary of case report 2

sCJD is a disease which shows very different radiological and clinical presentations. We presented a patient in the final stage of sCJD, who presented the clinical picture of an UWS or AS. Nevertheless, we were able to detect activation of the primary somatosensory cortex when examining the patient using a task fMRI. This finding is highly surprising because the cortex is already involved in the early stages of the disease. Hence, the cerebral cortex of the patient maintained activity also in the later stages of the disease. We have to point out that we just found activity in the primary somatosensory cortex because we could not investigate other functions in this study. The findings presented here suggest the persistence of plasticity and thus, the theoretical possibility of functional recovery. The initial diagnosis via the CRS-R did not prove true and the patient was not in an AS when undergoing the fMRI investigation. Hence, our findings should be taken into account by treating therapists, physicians, caregivers and relatives.

5. Analysis of resting state fMRI data

5.1. Introduction to resting state fMRI

Resting state fMRI describes the form of fMRI acquisition when no specific task is performed, for a detailed review of resting state fMRI see, e.g., (Smitha et al., 2017). This paradigm has been gaining more and more popularity because of different reasons. One is that there is nearly no compliance of the subject or patient needed. Moreover, it is easy to acquire, does not need any further tools or equipment, and there are a lot of analysis methods available. Another huge advantage is that studies showed that resting state fMRI can also be undergone by difficult patient groups like pediatric patients or patients with scDOC. All this makes it more favorable when compared to task-based fMRI. Resting state signals are low frequency signals in the range of 0.01-0.08 Hz and its basis lies in studies of Biswal and colleagues who investigated the transfer function in the motor cortex and sources of noise in the brain (Biswal, 2012; Raichle and Mintun, 2006). Resting state fMRI and task fMRI both have the same basic underlying principle. Nevertheless, there are some differences. These differences are listed in Table 5.

Table 5: Comparison of task-based and resting state fMRI. rs-fMRI: resting state fMRI , SNR: signal-to-noise ratio (Smitha et al., 2017)

Task-based fMRI	rs-fMRI
Analyses of spontaneous modulations in the BOLD signal in the presence of a particular activity (e.g. finger-tapping, eye-blinking, naming, memorizing, etc.)	Analysis of the spontaneous BOLD signal in the absence of any explicit task or an input
Task-related increase in neuronal metabolism are less than 5%	60-80% of brain's energy is consumed during resting state
During task-based activity the focus is only on a very small fraction of the brain's overall activity	In term of overall brain function, the resting state brain activity is far more significant than task-related activity

The signal during a task-related activity is very small compared to the noise, i.e. 80% of the BOLD modulation is discarded as noise	The signals which are discarded as noise in task fMRI is taken as signals in rs-fMRI as they are the low frequency spontaneous fluctuations in the BOLD signal
Due to discarding of signal as noise, task fMRI has a low SNR	Have improved SNR since it takes the overall spontaneous low frequency fluctuations
For the interpretation of results, a large number of trials are required in task fMRI	No need of more trials like task fMRI
If one wants to analyse the motor function and language function, a separate task may be required to analyze each function in task-based fMRI	In rs-fMRI, the acquired may be used to analyse one or more functions
Patient cooperation is essential to do task fMRI	Paediatric patients, patients with low IQ and even patients in the vegetative and coma state are able to do rs-fMRI
Repeated sessions of task-based activity to assess the disease prognosis, treatment effect etc. will result in familiarity with the task which will affect the output adversely	In rs-fMRI even we are taking different sessions, due to the absence of task, we are able to avoid the task-related confusions and uncertainties faced by task fMRI

An adult brain comprises about 2% of the body weight of the adult. However, it consumes 20% of the energy of the human body (Raichle, 2006). Of this energy the brain uses about 60 to 80% for communication between neurons and cell support. However, the brain uses just 0.5 to 1% for elicited activity (Raichle and Mintun, 2006).

5.1.1. Analysis methods for resting state fMRI data

The first method used for resting state network analysis was *seed-based analysis* (Biswal et al., 1995). This method uses an ROI as seed and searches for all the voxels that have a correlation to this seed. It is an easy approach which can be interpreted straightforward. Nevertheless, it is difficult to analyze the whole brain using this approach.

Another very popular approach is the *Independent Component Analysis* (ICA). This method is data-driven and relies on a blind separation algorithm (Bell and Sejnowski, 1995; Boly et al., 2008; McKeown et al., 1998). It simultaneously analyzes voxel to voxel interactions from different brain networks. A big advantage of this method is that there is no prior knowledge needed. Nonetheless, such prior knowledge is useful to distinguish the network components of the resting state from those components arising from noise.

The next method, which will also be discussed in Section 5.5, is *graph theory*. This approach is used to find mathematical models of network functions of the brain. The networks have connections between different regions and subregions. The main concept is the study of edges and nodes and their interaction (Butts, 2008).

5.1.2. Different resting state networks

Earlier studies showed that there are several resting state networks. Following (Smitha et al., 2017), the most important ones are briefly described,.

- *Salience network*

This network consists of the presupplementary motor area, bilateral insula, and the dorsal anterior cingulate cortex. It plays an important role in the regulation of other networks. Hence, its dysfunction influences a lot of other networks. Furthermore, it is important for rapid changes of behavior. Thus, its proper functioning is needed to commence and control cognition processes (Ham et al., 2013; Menon and Uddin, 2010; Uddin, 2015)

- *Auditory network*

The auditory network comprises the left and right primary auditory cortex, planum polare and temporale, Heschel's gyrus, posterior insular cortex and lateral superior temporal gyrus (Andoh et al., 2015; Schmidt et al., 2013).

- *Basal ganglia network*

This network involves the basal ganglia, subthalamic nucleus, striatum, substantia nigra, global pallidum interna and externa. Changes in the function of the basal ganglia is the basis of Parkinson's disease. The network plays a role in controlling motor areas as well as emotion or cognition (Afifi, 2003; Balasubramani et al., 2015; Rolinski et al., 2015; Szewczyk-Krolikowski et al., 2014).

- *Visual network*

The visual network describes the synchronous activation of the bilateral and medial calcarine sulcus and extrastriate regions, i.e., the inferior area of the precuneus, the lingual gyrus and the lateral geniculate nucleus of the thalamus. Of the aforementioned, the lateral geniculate nucleus connects the visual input and the primary visual cortex (Beckmann et al., 2005).

- *Visuospatial network*

This network involves the regions of the posterior parietal cortex of the occipitoparietal junction, the posterior cingulate cortex, the midline of the precuneus, and the frontal pole. As the name suggests, it is involved in orienting to salient visuospatial cues (Beckmann et al., 2005; Greicius et al., 2004, 2003; Gusnard et al., 2001).

- *Default mode network*

The default mode network is the most popular resting state network but discussing all the details would be beyond the scope of this work. Hence, just a short introduction is given here. It consists of the posterior cingulate cortex, the lateral parietal cortex, and the medial prefrontal cortex. This network is especially active during rest. Thus, it is a perfect candidate for resting state fMRI. Sometimes it is also referred to as the task-negative network because it becomes deactivated when the subject performs any task. This network is involved in social cognition, such as emotional processing, mind wandering, introspection, thinking, and other mental tasks (Blakemore, 2008; Gusnard et al., 2001; Sherman et al., 2014). The precuneus is a special part of the default mode network. It has a higher metabolic rate than other regions during resting state. It is involved in manipulating mental images or internally guiding attention, autobiographical memory retrieval, reward outcome monitoring, and emotional stimulus processing (Cavanna and Trimble, 2006; Maddock et al., 2003, 2001).

- *Language network*

The language network involves Broca's and Wernicke's area but also the prefrontal, temporal parietal and subcortical regions. It is mainly involved in speech, reading, mimicking, comprehension, interpreting, etc. Moreover, Broca's area is a known location of mirror neurons. These neurons are active when subjects perform goal-directed tasks or while observing such goal-directed movements performed by others (Ardila et al., 2016; Kilner et al., 2009; Lametti and Mattar, 2006; Skipper et al., 2007).

- *Executive network*

This network describes the dorsolateral prefrontal cortex and the posterior parietal cortex. It is involved in executive functions. It is also anticorrelated during the resting condition (Binder et al., 1999; Fox et al., 2005; Shulman et al., 1997).

- *Executive control network*

The executive control network comprises the medial and superior frontal gyrus, the anterior cingulate cortex, the ventrolateral prefrontal cortex, the paracingulate gyri, and the subcortical regions of the thalamus. It is active during cognitive control, tasks needing the working memory, control of intellectual activities and target-directed activities (Krmpotich et al., 2013; Seeley et al., 2007).

- *Sensorimotor network*

The sensorimotor network is special because it was the first one studied by Biswal et al. There is a high correlation between the right and the left motor cortex (Biswal et al., 1995, 1997; Biswal, 2012).

Figure 24 and Figure 25 show seed-based analyses resulting in the resting state networks. Hence, Figure 24 shows coronal, sagittal, and axial images of the salience network, the auditory network, the basal ganglia network, the higher visual network, the visuospatial network, and the default mode network. Figure 25 shows the other networks, namely the language network, the left executive control network, the right executive control network, the precuneus network, the primary visual network and the sensory motor network.

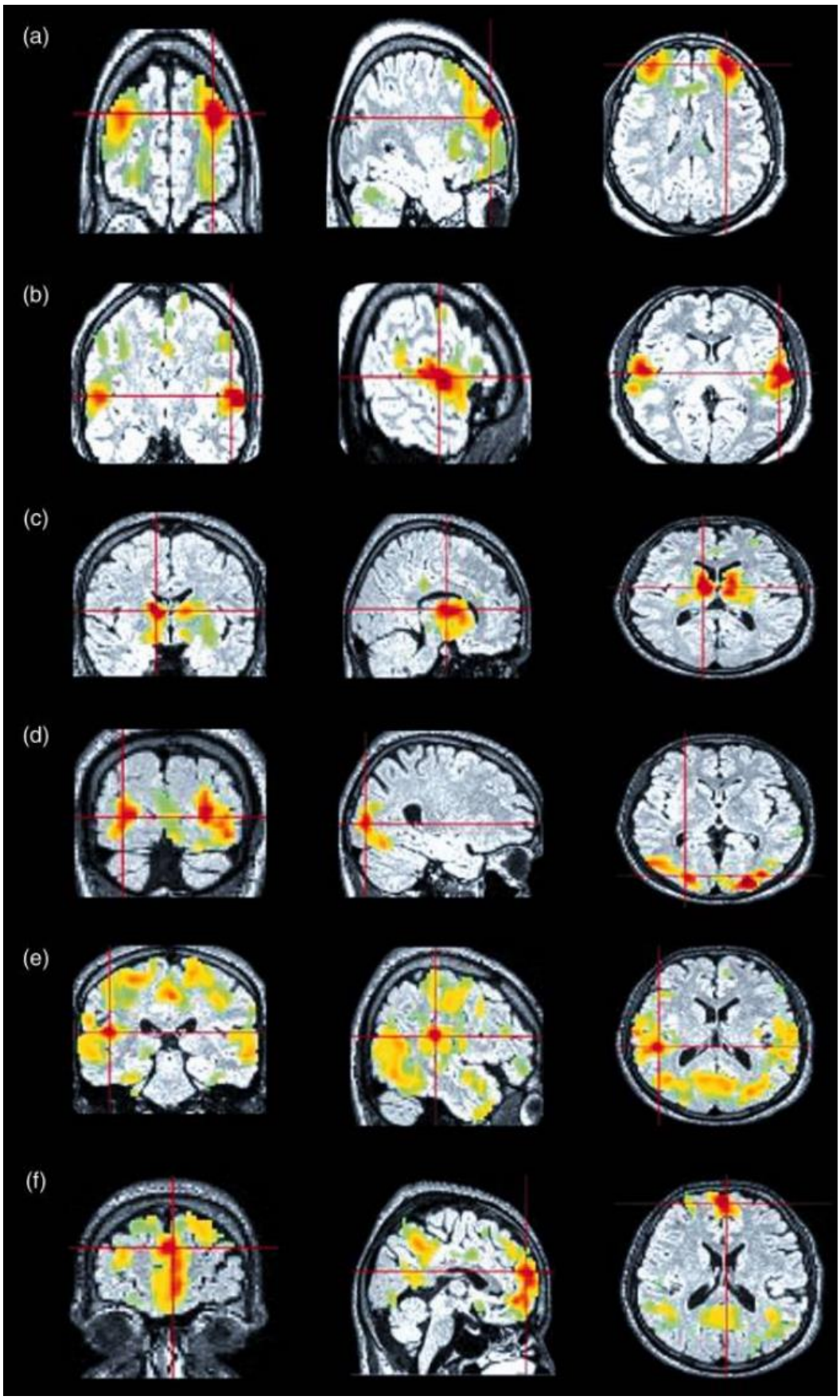

Figure 24: Resting state networks from seed-based analysis, showing coronal, sagittal and axial images of (a) salience network, (b) auditory network, (c) basal ganglia network, (d) higher visual network, (e) visuospatial network, and (f) default mode network. (Smitha et al., 2017)

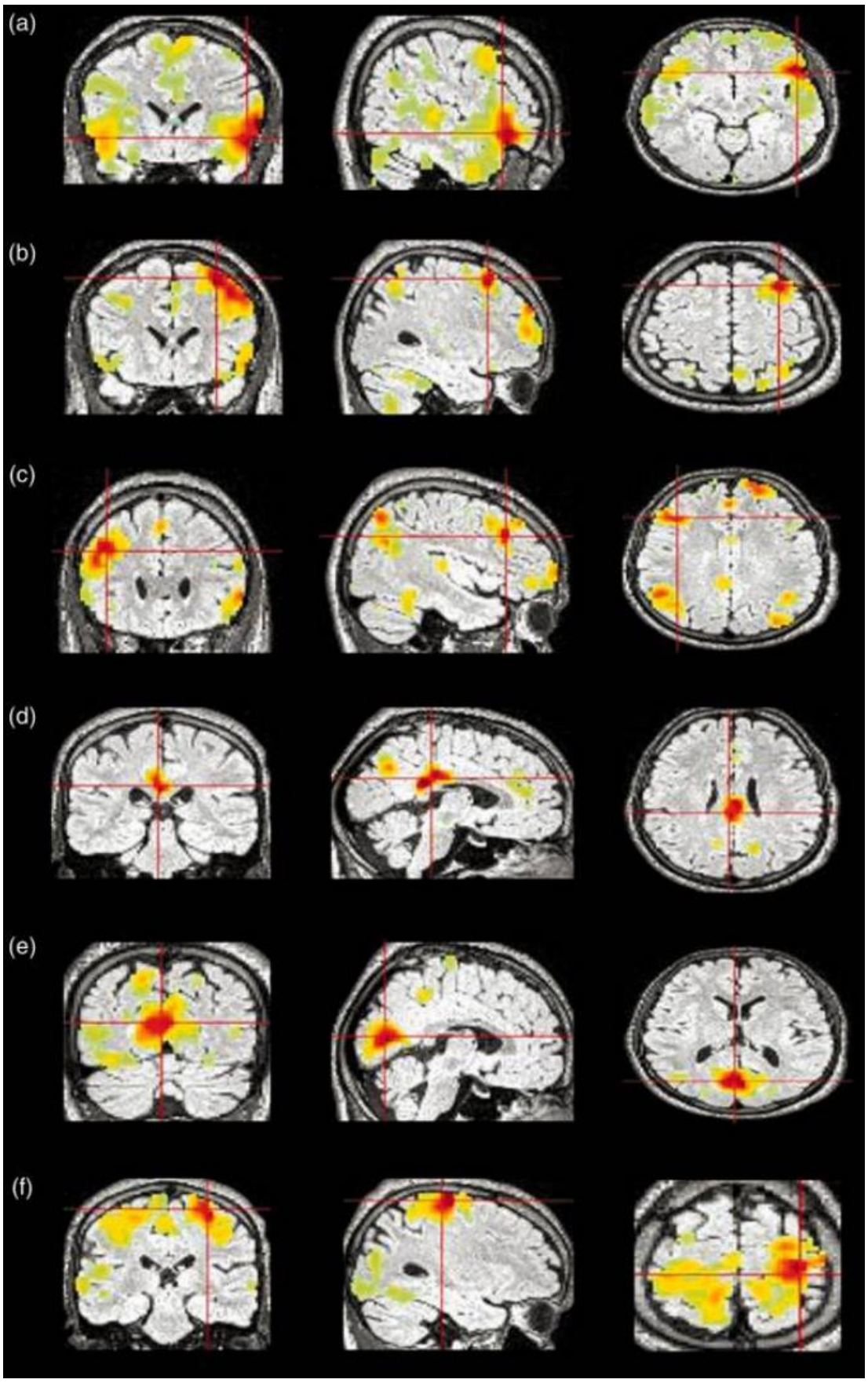

Figure 25: Resting state networks from seed-based analysis, showing coronal, sagittal and axial images of (a) language network, (b) left executive control network, (c) right executive control network, (d) precuneus network, (e) primary visual network, and (f) sensory motor network. (Smitha et al., 2017)

5.2. Experimental details for the resting state fMRI measurement

Before starting the experiment, we obtained the approval of the Ethics Commission Salzburg (Ethikkommission Land Salzburg, number 415-E/952). In the following, we focus on the separation of healthy controls and patients with either UWS or MCS. We included patients of different ages and etiologies (see Table 15). The healthy subjects were of mean age 44.17 (standard deviation 19.45, range 20-79) with 8 female und 22 male, and had no history of neurological or psychiatric disorders. The data for this experiment were acquired over several years. During this time there were hardware updates made in the clinic which resulted in two different scanners being used for the experiments, namely a 3 Tesla Philips Achieva (Philips, Amsterdam, Netherlands) and a 3 Tesla Siemens Tim Trio (Siemens, Erlangen, Germany). A total number of 58 patients were included in the study. Among those subjects, 34 were in UWS, 22 in MCS and 2 were not defined. 13 UWS patients and 4 MCS patients were scanned using the 3 T Philips and the rest using the 3 T Siemens scanner. Of the healthy subjects, 12 were scanned using the 3 T Philips and the rest using the 3 T Siemens scanner. The 3 T Philips scanner acquired T2*-weighted images in the axial plane with EPI sequence. The TR was 2.2 s and the TE was 45 ms. 25 slices with a slice thickness of 4.5mm and an inter-slice gap of 0.5 mm were acquired. The FOV was 210 mm^2, the matrix size 64x64, and the flip angle 90°. Finally, the parameters of the 3 Tesla Siemens scanner were as follows: T2*-weighted images with EPI sequence in the axial plane, 36 slices with a slice thickness of 3 mm but no interslice gap, FOV=192 mm^2, TR=2.25 s, TE= 30 ms, and a flip angle of 70°. Besides, a T1-weighted MPRAGE sequence was also acquired for all 88 participants. For the experiment the subjects were instructed to lie still and not to think about anything in particular (Wutzl et al., in prep., in prep.b).

5.3. Preprocessing of the resting state fMRI data

The data from the scans were preprocessed using the CONN functional connectivity toolbox (Whitfield-Gabrieli and Nieto-Castanon, 2012). We applied the default pipeline of the software but without smoothing (for more details on the different steps see Section 2.3.1). The CONN default pipeline starts with realigning and unwarping the functional data. After that the functional data are centered, slice-time corrected, and outlier detection was done based on the Artifact Detection Toolbox (ART) for which we used 97th percentiles in normative samples as thresholds. Moreover, functional direct segmentation was done simultaneously with GM, WM and cerebrospinal fluid. Then, MNI normalization was performed. The structural MRI data were also preprocessed in this pipeline, i.e., centered, segmented, and normalized. Furthermore, denoising was applied. Quality control was performed

throughout the preprocessing pipeline. Hence, some of the patients had to be removed, e.g., because parts of the brain were missing on the scans or because of too many moving artefacts. This resulted in a total of 29 UWS and 20 MCS patients (UWS1, UWS7, UWS14, UWS18, UWS19, MCS13, and MCS22 had to be excluded). None of the healthy subjects had to be removed. After the preprocessing, an ROI-to-ROI analysis using the CONN default atlas was performed and Fisher's Z transformed correlation matrices were obtained (Wutzl et al., in prep., in prep.b).

The CONN atlas consists of three parts: a cortical, subcortical, and a cerebellar part. The cortical part is divided into 91 ROIs by the FSL Harvard-Oxford Atlas maximum likelihood cortical atlas with bilateral areas being divided into right and left hemisphere. The subcortical part contains 15 regions from the FSL Harvard-Oxford Atlas maximum likelihood subcortical atlas where WM, cerebral cortex, and lateral ventrical areas are disregarded (Desikan et al., 2006; Frazier et al., 2005; Goldstein et al., 2007; Makris et al., 2006). Moreover, the cerebellar parcellation is taken from the AAL Atlas (Tzourio-Mazoyer et al., 2002). To avoid assigning multiple labels to some voxels, a precedence of cortical > cerebellar > subcortical is used. See Figure 26 for a representation of the different ROIs in sagittal, coronal and axial view. A 3D representation can be found in Figure 27. Table 16 gives all ROI numbers and the associated brain regions' names.

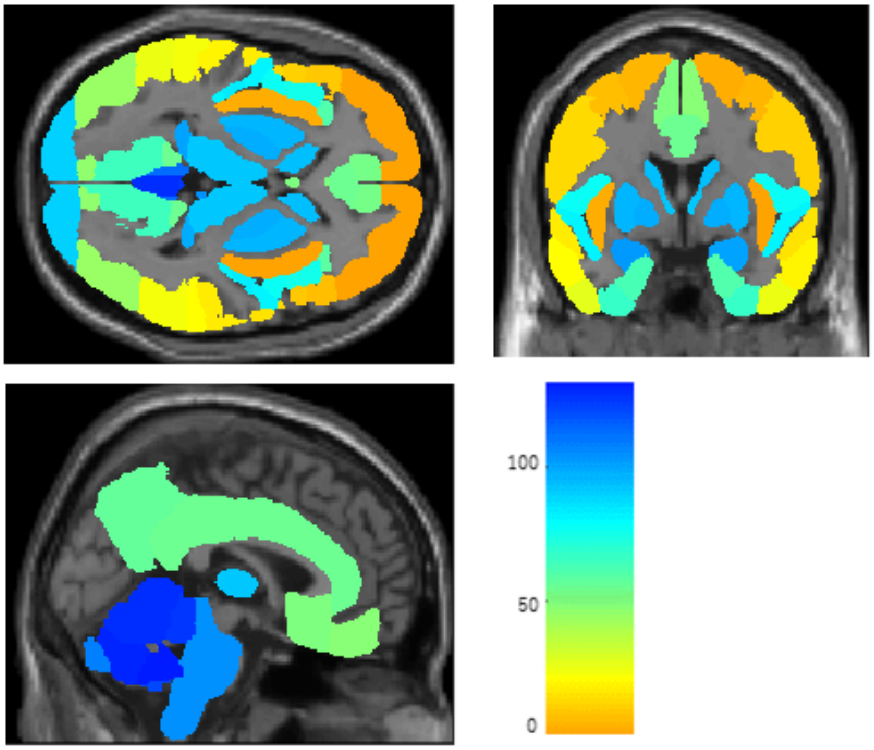

Figure 26: CONN atlas showing the 132 different regions of interest in sagittal, coronal and axial view. The colors indicate different ROIs. (Whitfield-Gabrieli and Nieto-Castanon, 2012).

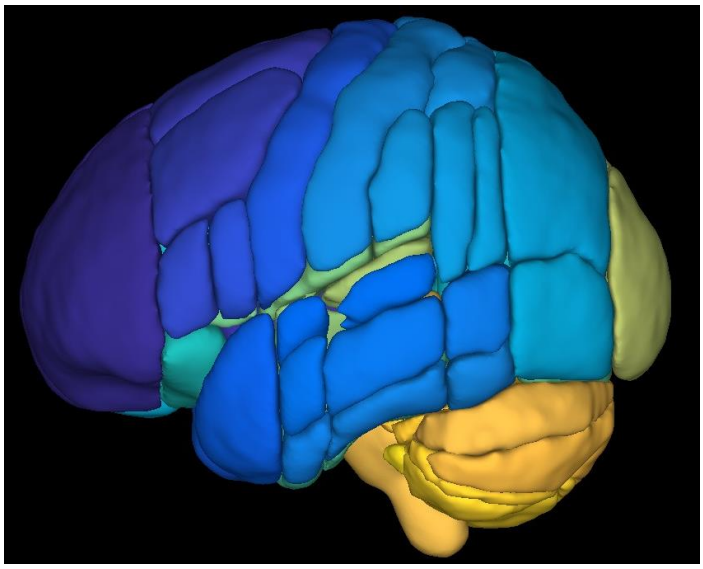

Figure 27: 3D view of the different ROIs of the CONN atlas. Different colors indicate different ROIs. (Whitfield-Gabrieli and Nieto-Castanon, 2012).

5.4. Connectivity analysis using the software CONN

5.4.1. Using the software CONN

First, we started with a connectivity analysis of the resting state paradigm for which we used CONN (Whitfield-Gabrieli and Nieto-Castanon, 2012). The different combinations of subject groups were analyzed, i.e., healthy subjects versus scDOC patients, healthy subjects versus MCS patients, healthy subjects versus UWS patients, and MCS versus UWS patients. We included all possible confounds gained by CONN's quality control, namely

- Number of valid scans
- Number of invalid scans
- Maximum motion
- Mean motion
- Maximum global signal
- Mean global signal
- GM volume
- GM eroded volume
- WM volume
- WM eroded volume
- CSF volume
- CSF eroded volume
- Average correlation GCOR of the rest condition.

This was done in order to make sure that the results are just due to the differences in the groups and not due to any of the above-mentioned confounding factors.

5.4.2. Results found with the software CONN

When testing which connections are stronger in healthy subjects than in patients, we find that eight regions are important. These are

- lateral occipital cortex, inferior division right (iLOC r)
- lateral occipital cortex, inferior division left (iLOC l)
- precentral gyrus right (PreCG r)
- precentral gyrus left (PreCG l)
- occipital fusiform gyrus right (OFusG r)
- occipital pole left (OP l)
- temporal pole right (TP r)
- temporal pole left (TP l).

All the connections, i.e., iLOC r to iLOC l, PreCG r to PreCG l, OFusG r to OP l and TP r to TP l are significantly (FDR corrected on analysis level with a significance level of 0.05) stronger in healthy subjects when comparing them to patients. A graphical representation can be found in Figure 28 and the statistics are shown in Table 6. The following Figures (Figure 29 and Figure 30) and Tables (Table 7 and Table 8) show the results of the comparison from healthy subjects to MCS and UWS patients, respectively. First of all, what can be found is that, the connection OFusG r- OP l is not significant for healthy subjects versus MCS patients whereas the connections PreCG r-PreCG l and TP r- TP l do not show up as significant when comparing healthy subjects to UWS patients. The comparison of MCS to UWS patients did not show any significant results at all.

5.4.3. Discussion of the results found with the software CONN

The results that we found show that there are four combinations of connections that are stronger connected when comparing healthy subjects to patients. Three of these are significant when comparing healthy to MCS. Hence, we conclude that the connection OFusG r – OP l may still be strong in MCS patients but not in UWS patients. Indeed, we find that this connection, together with the connection iLOC r-iLOC l, plays an important role when comparing healthy subjects to UWS showing that the connection is weaker in UWS patients than in healthy subjects. On the other hand, we do not find the connections PreCG r-PreCG l and TP r-TP l to be significant in this comparison. Thus, these connections may be important just for MCS patients. We hypothesize that the connections

OFusG r-OP l, as well as PreCG r-PreCG l, and TP r-TP l are different in MCS and UWS patients. However, this could not be found when comparing MCS to UWS patients. This does not mean that these connections are not different at all but just means that they are not statistically significant.

5.4.4. Summary of the connectivity analysis with the software CONN

We used the toolbox CONN (Whitfield-Gabrieli and Nieto-Castanon, 2012) to compare the connections between the different ROIs of resting state fMRI of healthy controls and patients with scDOC. After the standard preprocessing steps described in Section 5.3 we conducted an ROI-to-ROI analysis using all possible confounds generated by CONN to find significant connections. We found four brain connections to be stronger in healthy controls than in scDOC patients. Among these, three remain significant when analyzing healthy subjects versus MCS patients and two remain significant when analyzing healthy versus UWS patients. Hence, there seems to be a difference in the connection between MCS and UWS patients, but these did not show up as statistically significant (FDR corrected on analysis level with a significance level of 0.05).

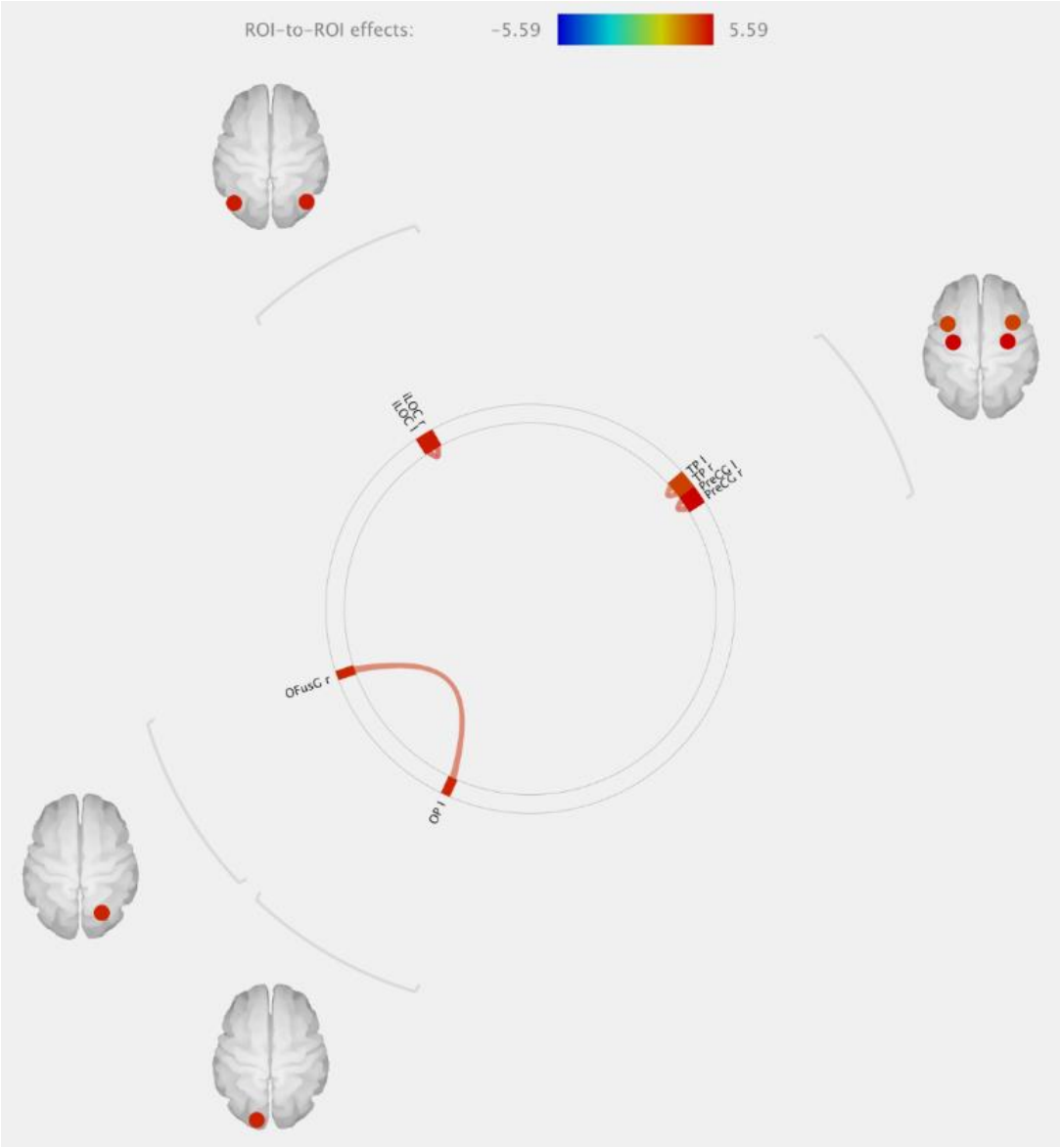

Figure 28: Graphical representation of the connections that are stronger in healthy subjects than patients (when taking the groups MCS and UWS together). The color code reflects t-statistics whose values can be found in the following Table 6.

Table 6: Table showing the statistics of the results when comparing healthy subjects to patients.

Analysis Unit	**Statistic**	**p-FDR**
iLOC r-iLOC l	T(67)=5.59	0.0039
PreCG r-PreCG l	T(67)=4.98	0.0203
OFusG r- OP l	T(67)=4.85	0.0226
TP r- TP l	T(67)=4.67	0.0321

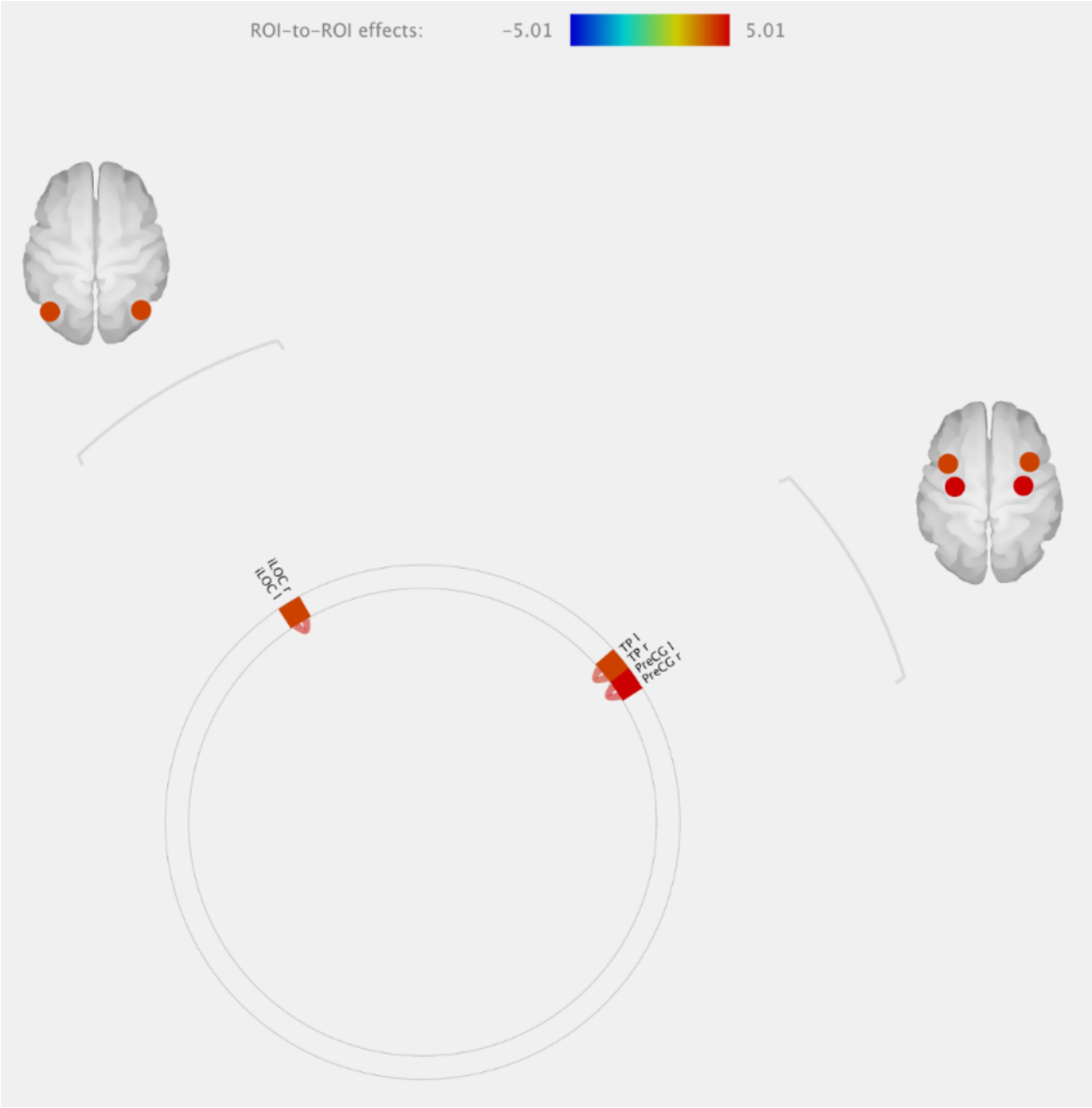

Figure 29: Graphical representation of the results when comparing healthy subjects versus MCS patients. The color code reflects t-statistics whose values can be found in the following Table 7.

Table 7: Table of results when comparing healthy subjects to MCS patients.

Analysis Unit	**Statistic**	**p-FDR**
PreCG r-PreCG l	T(67)=5.01	0.0257
iLOC r-iLOC l	T(67)=4.93	0.0257
TP r- TP l	T(67)=4.67	0.0441

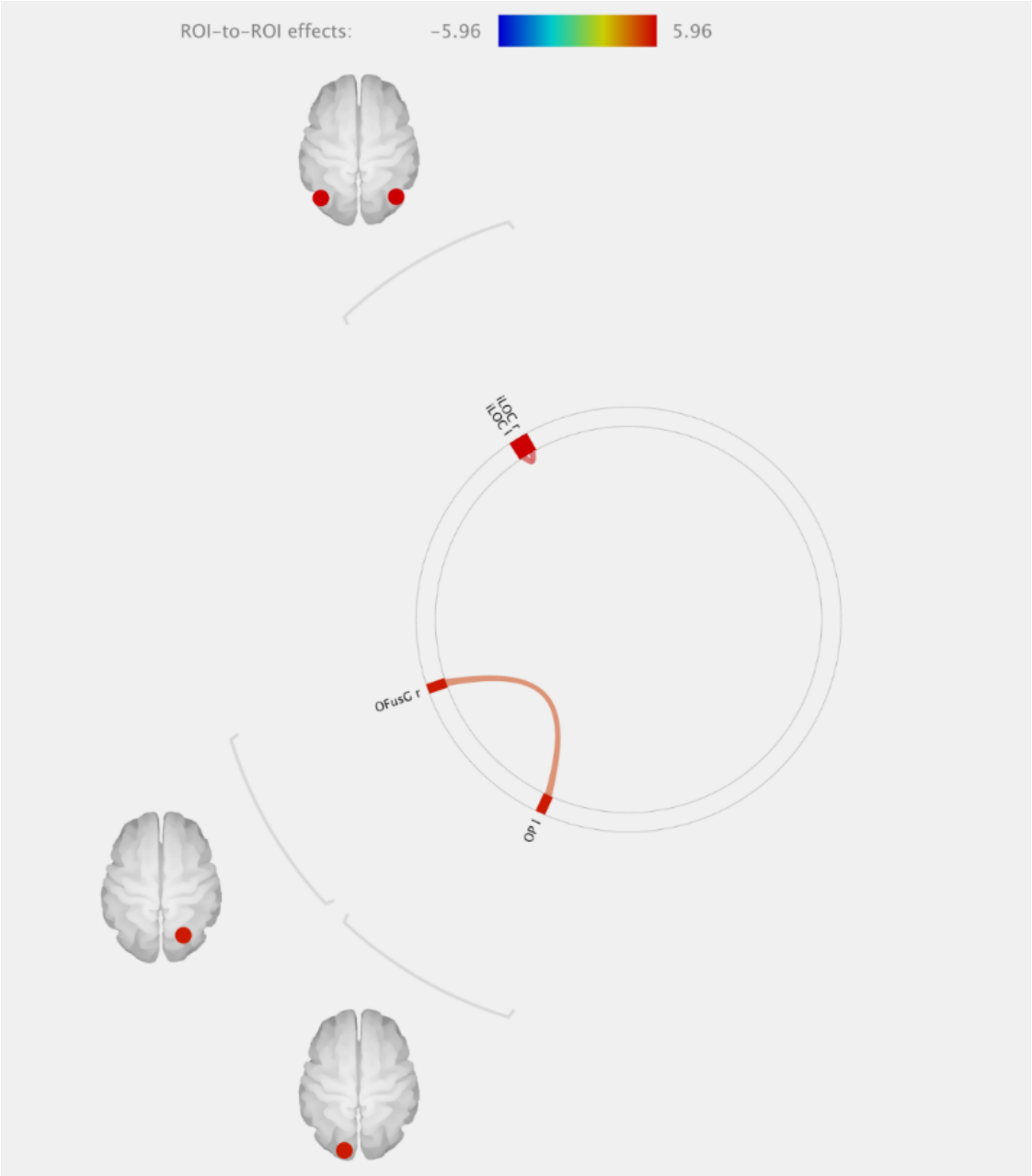

Figure 30: Graphical representation of the results when comparing healthy subjects versus UWS patients. The color code reflects t-statistics whose values can be found in the following Table 8.

Table 8: Table of results from the comparison from healthy subjects to UWS patients.

Analysis Unit	**Statistic**	**p-FDR**
iLOC r-iLOC l	T(67)=5.96	0.0010
OFusG r- OP l	T(67)=4.82	0.0384

5.5. Analyzing resting state fMRI data using networks and modularity

Before starting this subsection, we introduce some mathematical definitions which are needed later on.

5.5.1. Mathematical definitions of networks and modularity

Networks or graphs have been studied for a long time in disciplines like mathematics or sociology. However, its use in fields like neuroscience is quite new. In order to describe the basic mathematical models of graphs we follow (Estrada, 2011) and (Rubinov and Sporns, 2010).

First, we give a working description of a network, nodes, and links.

Definition 1: A diagrammatic representation of a system is called a network *or* graph. *Such a network or graph consists of* nodes *(*vertices*), which stand for the entities of the system, and* links *(*edges*) which connect the nodes and stand for the special interconnection of the nodes they combine.*

Now a more formal definition of a network or a graph is given in Definition 2.

Definition 2: The tuple G=(N, E) is called a network *or* graph *if N is a finite set of nodes and* $E \subseteq N \otimes N = \{e_{11}, e_{12}, \dots e_{ij}, \dots e_{nn}\}$ *a set of links.*

The links or edges can be multifold. The following Definition 3 gives an overview of the different possible types of links in a network.

Definition 3: A link is called

- Simple *or* undirected *link if it connects two nodes,*
- Directed *link if it starts in one node and ends in another,*
- Multi *link if there is more than one link between a pair of nodes*
- Self-loop *if a link connects a node to itself.*

Moreover, links can have weights associated to them. Such a (in general positive) number represents the strength of the link between the nodes.

Another important object, which is described in the next Definition 4, is the adjacency matrix.

Definition 4: The adjacency matrix $A = (A_{ij})_{nxn}$ *of G = (N, E) is given by*

$$A_{ij} := \begin{cases} 1 & if\ e_{ij} \in E \\ 0 & otherwise. \end{cases} \tag{14}$$

with e_{ij} being a link between node i and node j.

Considering brain networks, nodes represent in general ROIs while links stand for anatomical, functional, or effective connections (Friston Karl J., 1994). Anatomical connections represent most of the time WM tracts between ROIs whereas functional connections are temporal correlations between two ROIs, even if there is no structural connection between them. Finally, effective connections are direct or indirect causal influences which one ROI may have on another one.

When dealing with networks it is often useful to search for *modules* which are also called communities, clusters, classes, groups, etc. These modules are roughly speaking a group of nodes which are more tightly connected to one another than to the rest of the network. Different definitions are found in the literature, see, e.g., (Wasserman and Faust, 1994). Here we give the definition from (Radicchi et al., 2004), but first we define the term subgraph.

Definition 5: A subgraph *V of a graph G is a graph which is formed by a subset of the edges and vertices of G.*

Definition 6: Let A_{ij} be the adjacency matrix of the network G. The degree *of a node i is given by $k_i=\Sigma_j A_{ij}$. Let $V \subset G$ be a subgraph to which i belongs. Moreover,*

$$k_i^{in}(V) = \sum_{j \in V} A_{ij} \tag{15}$$

$$k_i^{out}(V) = \sum_{j \notin V} A_{ij}. \tag{16}$$

Then we define a module in strong sense *as the subgraph V if*

$$k_i^{in}(V) > k_i^{out}(V) \qquad \forall i \in V \tag{17}$$

holds. Furthermore, a module in weak sense *is defined as the subgraph V if*

$$\sum_{i \in V} k_i^{in}(V) > \sum_{i \in V} k_i^{out}(V) \qquad \forall i \in V \tag{18}$$

holds.

Subgraphs V which are either modules in the strong or in the weak sense are called *modules*. Where necessary, it will be specified about which type we are talking.

There are many methods to compare module partitions. Two of the most often used ones are the *variation of information* and the *mutual information* of two partitions or clusterings. We start with describing mutual information, i.e., how much information does one clustering have about the other.

Definition 7: Mutual information *of two clusterings C and C' is given by* (Meila, 2007)

$$I(C, C') = \sum_{k=1}^{K} \sum_{k'=1}^{K'} P(k, k') log \frac{P(k, k')}{P(k)P'(k')} \tag{19}$$

where P(k,k') denotes the probability that a node belongs to clustering C_k in C and to $C_{k'}$ in C', i.e., the random variables associated with the clusterings. P(k) is the probability mass function, and K and K' are the number of nodes in the clusterings C and C', respectively.

To describe the term variation of information we also need to define entropy.

Definition 8: Entropy *H of a clustering C is defined as* (Meila, 2007)

$$H(C) = -\sum_{k=1}^{K} P(k) log P(k) \tag{20}$$

with P the probability mass function and K the number of nodes in the clustering.

With these terms at hand, we can now turn to the variation of information.

Definition 9: The variation of information *of two clusterings C and C' is described as* (Meila, 2007)

$$VI(C, C') = H(C) + H(C') - 2I(C, C'). \tag{21}$$

In the following we define some of the most important features of graphs, see, e.g., (Rubinov and Sporns, 2010) for more details.

Definition 10: Let N be the set of all nodes in the graph G then the number of triangles *around a node i is given by*

$$t_i = \frac{1}{2} \sum_{j,h \in N} A_{ij} A_{ih} A_{jh}. \tag{22}$$

Definition 8: The clustering coefficient *C of the graph G is defined according to Watts and Strogratz* (Watts and Strogatz, 1998)*, with k_i being the degree of node i, N the set of all nodes, and n the number of all nodes in the graph, as*

$$C = \frac{1}{n} \sum_{i \in N} C_i = \frac{1}{n} \sum_{i \in N} \frac{2t_i}{k_i(k_i - 1)}. \tag{23}$$

C_i denotes the clustering coefficient of node i with $C_i=0$ for $k_i<2$.

Definition 11: The shortest path *between node i and node j is given by*

$$d_{ij} = \sum_{A_{uv} \in g_{i \leftrightarrow j}} A_{uv} \tag{24}$$

where A_{uv} is the adjacency matrix and $g_{i \leftrightarrow j}$ is the shortest (geodesic) path. If the nodes i and j are disconnected, then $d_{ij} = \infty$.

Definition 12: The global efficiency *is defined by* (Latora and Marchiori, 2001) as

$$E = \frac{1}{n}\sum_{i\in N} E_i = \frac{1}{n}\sum_{i\in N}\frac{\sum_{j\in N, j\neq i} d_{ij}^{-1}}{n-1} \tag{25}$$

with n the number of nodes, N the set of all nodes, E_i the efficiency of node i, and d_{ij} the shortest path between nodes i and j.

Definition 13: The characteristic path length *L is given by* (Watts and Strogatz, 1998)

$$L = \frac{1}{n}\sum_{i\in N} L_i = \frac{1}{n}\sum_{i\in N}\frac{\sum_{j\in N, j\neq i} d_{ij}}{n-1} \tag{26}$$

where again n is the number of nodes, N the set of all nodes, and d_{ij} the shortest path between node i and j. Moreover, L_i is the average distance from i to all other nodes.

Definition 14: The small worldness *is defined as* (Humphries and Gurney, 2008)

$$\mathrm{S} = \frac{\mathrm{C}/\mathrm{C}_{\mathrm{rand}}}{\mathrm{L}/\mathrm{L}_{\mathrm{rand}}} \tag{27}$$

with C and L being the clustering coefficient and the characteristic path length of the graph G and C_{rand} and L_{rand} being the clustering coefficient and the characteristic path length of a random network. A small-world network is characterized by $S \gg 1$.

Definition 15: Betweenness centrality *of node i is* (Freeman, 1978)

$$b_i = \frac{1}{(n-1)(n-2)} \sum_{\substack{h,j\in N \\ h\neq j, h\neq i, j\neq i}} \frac{\rho_{hj}(i)}{\rho_{hj}} \tag{28}$$

with ρ_{hj} giving the number of shortest paths between the nodes h and j, $\rho_{hj}(i)$ the number of shortest paths between the nodes h and j that pass through node i, n the number of nodes, and N the set of all nodes.

Definition 16: The assortativity *is given by* (Newman, 2002)

$$r = \frac{l^{-1}\sum_{(i,j)\in L} k_i k_j - \left[l^{-1}\sum_{(i,j)\in L}\frac{1}{2}(k_i + k_j)\right]^2}{l^{-1}\sum_{(i,j)\in L}\frac{1}{2}(k_i^2 + k_j^2) - \left[l^{-1}\sum_{(i,j)\in L}\frac{1}{2}(k_i + k_j)\right]^2} \tag{29}$$

where l is the number of links, L the set of all links, (i,j) a link between node i and node j, and k_i the degree of node i.

Another term, which often comes up when dealing with networks, is *hub*. However, there is no clear definition of this term. A hub can be characterized by different factors, e.g., as nodes with high degree or high centrality.

5.5.2.1. Mucha's multislice modularity

As mentioned above, modules are roughly speaking clusters of nodes that are more tightly connected to each other than to the rest of the network, always in comparison to a null model. One way to define modules is via a *quality function Q* which compares the intracommunity edges with what would be expected at random.

Definition 17: Such a quality function Q is given by (Newman, 2006)

$$Q = \frac{1}{2m}\sum_{i,j}\left(A_{ij} - \frac{k_i k_j}{2m}\right)\delta(g_i, g_j) \tag{30}$$

with m being the number of links, A_{ij} the adjacency matrix, k_i the node degree, and

$$\delta(g_i, g_j) = \begin{cases} 1 & if\ node\ i\ and\ j\ are\ in\ the\ same\ module \\ 0 & otherwise \end{cases}. \tag{31}$$

What is crucial is the choice of the null model. Mucha et al. defined such a null model for multislice networks, i.e., coupled adjacency matrices, see Figure 31 for a graphical explanation of a coupled adjacency matrix.

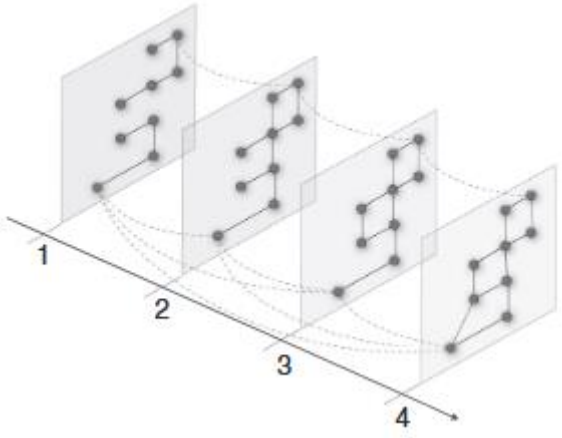

Figure 31: Graphical representation of a multislice network. Here four slices {1,2,3,4} are shown. The solid lines represent the intraslice connections given by the adjacency matrix A_{ijs} which gives the connection of node i to node j in slice s. On the other hand, the dashed lines represent the interslice connections given by $C_{jrs,}$ representing the connection of node j to itself from slice r to slice s. This interslice connections are just shown for two nodes. The upper one shows coupling just between neighboring slices, which is appropriate for ordered slices, whereas the lower one shows an all-to-all interslice coupling which is suitable for categorical slices. (Mucha et al., 2010)

Mucha et al. updated the quality function of Definition 17 to

$$Q = \frac{1}{2\mu} \sum_{i,j,s,r} \left[\left(A_{ijs} - \gamma_s \frac{k_{is} k_{js}}{2m_s} \right) \delta_{sr} + \delta_{ij} C_{jsr} \right] \delta(g_i, g_j) \tag{32}$$

with γ_s the resolution, δ_{ij} the Kronecker Delta, and C_{jsr} the coupling strength for node j between slices s and r which is for simplicity taken to be binary $\{0,\omega\}$, depending on whether the coupling is present with strength ω or absent, i.e., a strength of 0. Moreover, μ is given by

$$2\mu = \sum_{j,s} \left(k_{js} + \sum_{\mathrm{r}} C_{jsr} \right). \tag{33}$$

Now, modules can be calculated using heuristic methods (Mucha et al., 2010). One of the most used one is the Louvain Algorithm. This algorithm consists of two parts that are repeated iteratively. The starting point is a weighted network with n nodes. The first step is to assign different communities to every node of the network which results in n communities. After that the neighbors of each node are taken into account. It is calculated how much the quality function Q would gain if the node i is moved to the same community as its neighbor j. If there is a positive gain when moving i to the community of one of its neighbors this is done. If not, i stays in its community. This is done for all nodes until no positive gain can be achieved. During the second step a new network is built consisting of nodes

which are communities of the first step. Then the first step is repeated with the new nodes. This whole process is repeated until no more gain is possible. For more details see (Blondel et al., 2008).

5.5.2.2. Accuracy, precision and recall

The most common way how to describe if a classifier performs well is in terms of its accuracy, also called recognition rate. This term is described in Definition 18, see, e.g., (Abe, 2010).

Definition 18:

$$accuray = \frac{number\ of\ correct\ predictions}{total\ number\ of\ predictions} \tag{34}$$

Some other metrics which we are going to need later on are *precision* and *recall*. They describe, similar to the accuracy, how good a classification algorithm is. The next definition explains these two quantities, see, e.g., (Abe, 2010).

Definition 19:

$$precision = \frac{true\ positive}{true\ positive + false\ positive} \tag{35}$$

$$recall = \frac{true\ positive}{true\ positive + false\ negative} \tag{36}$$

Figure 32 shows a graphical representation of precision and recall. Imagine we have a group of subjects with some suffering from a certain disease whereas others do not. We will call the ones having the disease the positive group and the ones that do not have the disease the negative group. The light gray dots in Figure 32 represent all the positive values, namely all the subjects that have the disease. All the dark gray dots represent those who do not have the disease, i.e., the negative values. After the classification we got a result for every subject. The ones in the dark green area are the ones that are classified correctly as positives. Whereas the ones in the red area are classified as positive but are indeed negative, meaning that our classifier would tell us that the subjects have a certain disease although they do not. The light green ones are the ones that do have the disease but are classified as not having it. On the other hand, the orange ones are the ones that do not have the disease and are correctly classified as negative.

Precision gives the percentage of true positives of all positives, i.e., the true and false positive ones. It can be interpreted as a measure of how trustworthy the algorithm is: *can I trust that a positively identified subject really has the disease?* On the other hand, recall gives the percentage of the true positives from all positives, in other words, the false negatives and the true positives. Hence, recall can be seen as some sort of detection rate, namely the chance of detecting a subject of having the disease, if he/she really does. An algorithm with high precision and low recall labels very few subjects/samples as positive but the ones that are positive labeled are correctly positive, in our example subjects that have the disease. On the other hand, an algorithm with high recall and low precision marks a lot of samples as positive but a lot of them are labeled incorrectly as positive, hence those who do not have the disease. Thus, an ideal algorithm has high precision and high recall, which means it detects a lot of samples as positive and these are labeled correctly.

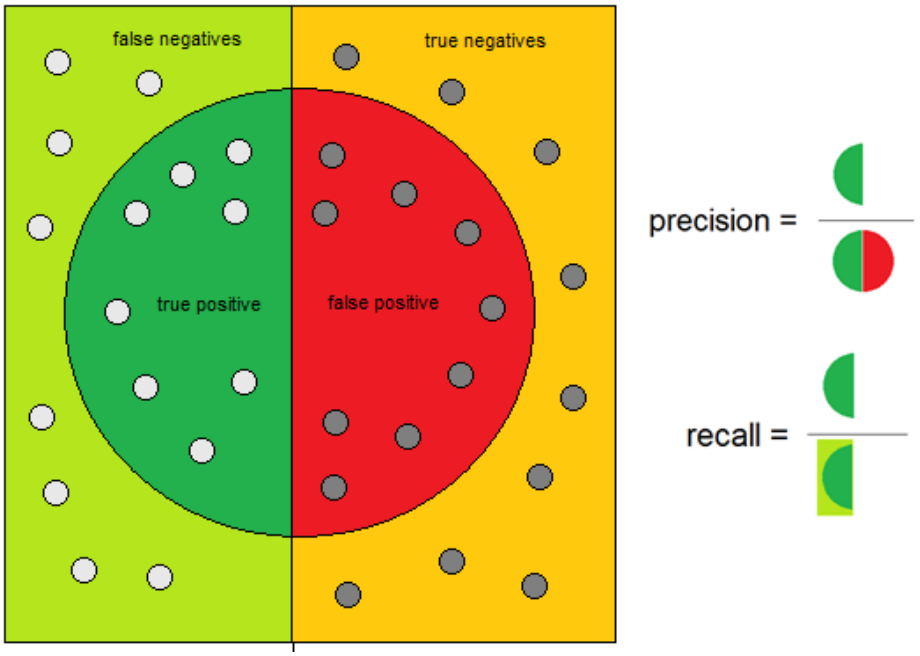

Figure 32: Graphical representation of precision and recall. The light gray dots represent the ones that are true in reality and the dark gray dots represent those who are false in reality. The big circle in the middle marks all dots that are classified as positive by the algorithm. Precision is given by the true positives divided by all positives given by the algorithm, i.e., true positives and false positives, whereas recall is defined as the quotient of true positive divided by all real positives, i.e., true positives and false negatives.

Using these two metrics we can calculate the F1-score. This is a metric that is suitable to compare the performance of a classifier when the sample sizes are imbalanced because, for imbalanced sample sizes, the frequently-used accuracy gives misleading results. The following Definition 20 explains how to calculate this metric.

Definition 20: The F1-score *is given by* (Powers, 2011)

$$F1=2*\frac{precision*recall}{precision+recall}. \quad (1)$$

5.5.2. Introduction to the analysis of resting state fMRI data with networks and modularity

As discussed in Section 3 the diagnosis and prognosis of patients with scDOC is very difficult. Hence, there is a need for new techniques. One new approach is the use of graph-theoretical tools. Using these methods, we focus on brain networks with ROIs as nodes and functional connectivities as edges. Considering human brain networks, it was found that they are generally modular, i.e., can be separated into modules (see Definition 6 in Section 5.5.1) and of small-world type (see Definition 14 in Section 5.5.1). Moreover, the modules consist of highly connected hubs (Bullmore and Sporns, 2009). Achard et al. demonstrated that these hubs were reorganized in comatose patients. They found that the fusiform gurus and precuneus, which are known to be hubs with high degree in healthy brain networks, were low-degree non-hubs in patients. On the contrary, the angular gyrus (normally a low-degree non-hub) was found to be a high-degree hub in patients. Clustering, modularity, global efficiency, and other global network measures (see Section 5.5.1 for mathematical definitions), were statistically not different when comparing healthy subjects and comatose patients (Achard et al., 2012). However, they just focused on patients in acute state (the maximal time between onset and scan was 32 days). Furthermore, they did not look at different subgroups of patients. However, Crone et al. found the same result as Achard et al. considering global network topology, but not for modularity. Indeed, they found a significant difference in modularity between healthy controls and patients (UWS and MCS together). In their work they present data from 59 patients with scDOC and found, besides the ones mentioned before, also alterations in connectivity and network properties of several regions in the cortico-thalamic and fronto-parietal regions. Moreover, differences between UWS and MCS were only reported for measures of segregation, namely in the right frontal and medial regions and in the precuneus. Furthermore, it is worth mentioning that most altered regions belong to highly connected nodes, also known as rich clubs (Crone et al., 2014).

Besides, Laureys and colleagues reported that the thalamo-cortical connectivity plays an important role for the recovery from coma. They stated that connectivity in that region was re-established in

some patients who recovered from UWS and thus regained consciousness (Laureys et al., 2000). Giacino et al. found that UWS patients have a global disconnection between higher-order cortices and primary cortical areas (Giacino et al., 2006). Large scale cortical networks associated with language and visual processing were advocated to be preserved in MCS patients (Schiff et al., 2005). Laureys et al. also proposed a biomarker to differentiate healthy controls from scDOC patients. They found the connectivity of the medial parietal cortex to be such a biomarker (Laureys et al., 2004).

5.5.3. Methods for the analysis of resting state fMRI data with networks and modularity

After preprocessing the fMRI data, we extracted the correlation matrices with Fisher's Z-transformed values from CONN (see Section 5.3). From now on the analysis was run in MATLAB (The MathWorks, Inc., Natick, Massachusetts, United States) Version 2018a using the Statistics and Machine Learning Toolbox Version 11.3, and the Brain Connectivity Toolbox (BCT), see (Rubinov and Sporns, 2010).

Before starting the multislice analysis, we calculated some metrics of the correlation matrix and checked for their statistical significance. The metrics were all calculated using the implementations in BCT and the statistical relevance was tested using a Welch test. When considering the global metrics, i.e., assortativity, betweenness centrality, edge centrality, characteristic path length, clustering coefficient, and global efficiency (for definitions see Section 5.5.1) there were no differences in any of the comparison groups: healthy versus MCS, MCS versus UWS, or healthy versus UWS. This is why we decided to try another approach to find statistically differences between our groups.

5.5.3.1. Multislice Modularity

Now let us turn to the multislice approach. The following workflow is shown in Figure 33. First, we thresholded the correlation matrices with a proportional threshold $\theta=0.1$. This number was chosen according to previous papers which showed that a link density of 10% gives optimal discriminative ability (Achard et al., 2012; Itahashi et al., 2014; Mansour et al., 2016). Furthermore, the correlation matrix was binarized, i.e., such a matrix has just entries 1 or 0 depending on whether there is or is a connection between two ROIs or not. This gave us an adjacency matrix for an undirected graph. Now, we searched for communities or modules. For this we used the multislice modularity by Mucha which estimates basic modular structures across networks (Mucha et al., 2010). We used a categorical mul-

tislice modularity algorithm (*GenLouvain*, 2018) which couples each node (ROI) from one slice (subject) to the same node in other slices, see also Figure 31. This algorithm makes use of two parameters namely ω which is the coupling parameter between subjects and γ which gives the modularity resolution, i.e., determines the number and size of modules. Up to know there is no agreed consensus on how to find the two parameters ω and γ. We decided to perform a grid search through the parameter space $\omega\epsilon\{0.1,0.2,0.4,0.6,0.8,1\}$ and $\gamma\epsilon\{0.25, 0.5, 0.75, 1, 1.25, \ldots 3.75,4\}$ and searched for how many modules were found with each combination. The results can be found in Table 17 and Table 18. Little surprising the result did not (or just little) depend on ω. The brain architecture consists of 10 to 15 modules. Hence, we tried to find values for γ that give us such a number of modules. This was found to be the case for γ=2.00. What is also worth mentioning is that the number of modules also depends on the number of slices (or subjects) one considers in the multislice modularity algorithm.

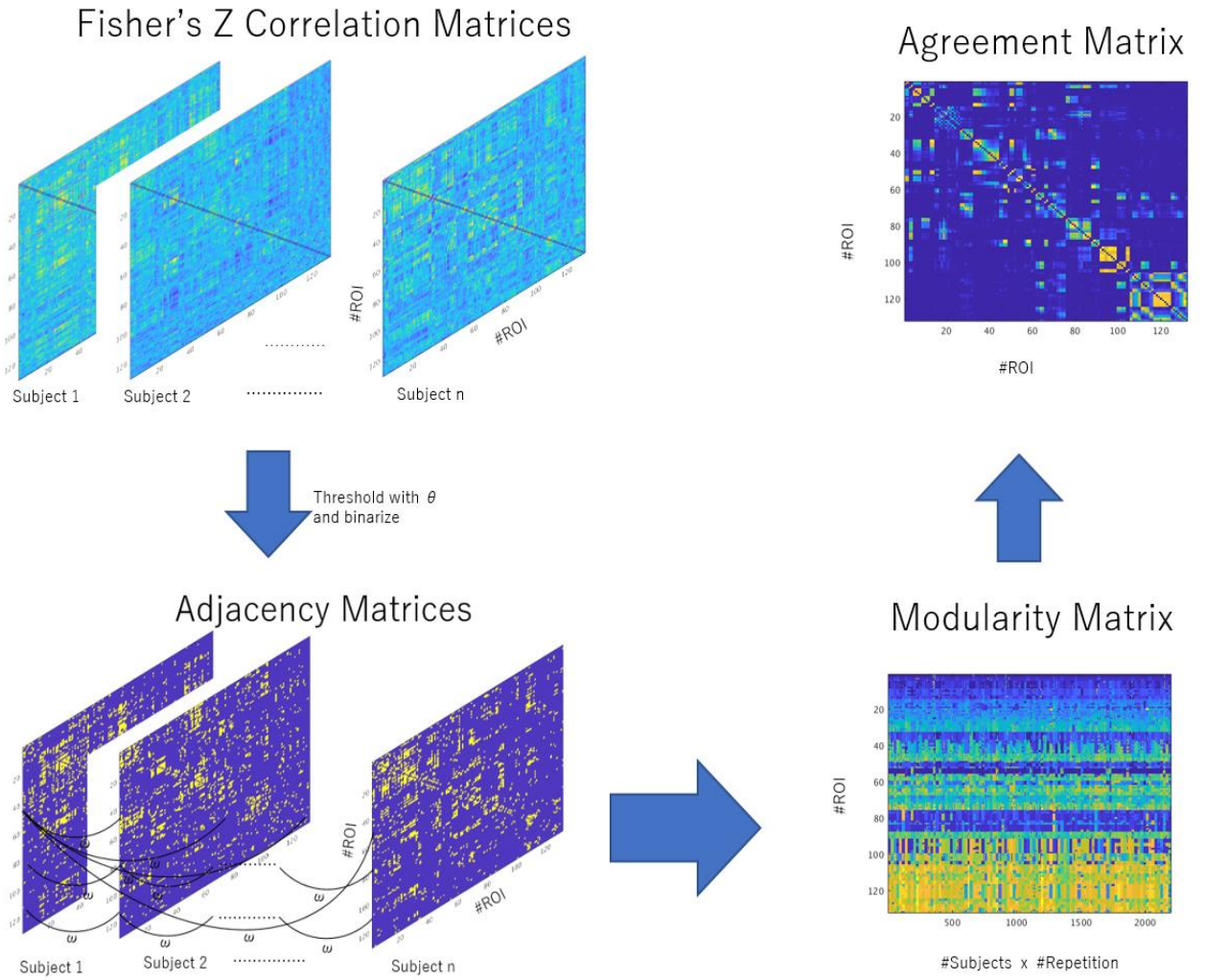

Figure 33: Workflow from Fisher's Z correlation matrices to agreement matrix. Starting in the upper left corner with the Fisher's Z correlation matrices which are thresholded and binarized to get the adjacency matrix. Using the multislice modularity algorithm gives us a modularity matrix which leads to the agreement matrix.(Wutzl et al., in prep.)

Since we did have more UWS patients and healthy controls than MCS patients, we randomly downsampled all groups to have the number of MCS patients, so that we could use the same γ and ω in our analyses. The next step was to find a suitable value for the coupling parameter ω. We did this again by trying different values, i.e., ω∈{0.01, 0.02, 0.03, ..., 0.32, 0.33, 0.34, 0.35}. This time we focused on the modularity matrix. We wanted the coupling coefficient ω to be big enough so that not all the subjects had totally different module partitions but also not so big that all the subjects had exactly the same partitions. Three different values for ω (ω=0.01, 0.25, 0.35) are plotted in Figure 34 with different colors indicating different modules. The x-axis shows the different slices or subjects and the y-axis the different ROIs. The colors per se do not have any specific meaning. The plot with ω=0.01 shows that the partitions are very different from each other, i.e., the module structure of the different subjects is very different. On the other hand, a coupling constant of ω=0.35 is so strong that the connection between the slices (subjects) is a lot stronger than between the nodes of each subject. Hence, this results in a plot where every subject has exactly the same module partition. We chose ω=0.25. because this is the largest value of ω where each partition for each subject is still unique.

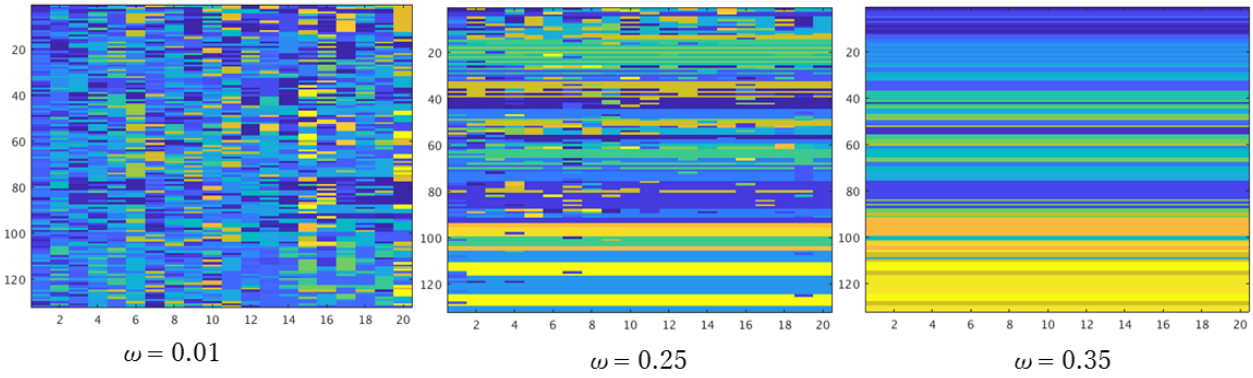

Figure 34: Comparison of different values for ω with ω=0.01 showing no real effect of the multislice coupling, i.e., every subject has a very different module composition whereas ω=0.35 shows that the coupling is so strong it is preferred over intra subject connectivity and ω=0.25 showing the tradeoff that every subject's partition is unique to this subject. The different colors symbolize different modules, x-axis indicates subjects or slices and the y-axis indicates the different ROI. (Wutzl et al., in prep.)

Once we found these two parameters, γ and ω, we could get back to the algorithm of Figure 33. Since the outcome of the multislice modularity algorithm is not deterministic, we run the algorithm 100 times to get an average of the modules. After that we created the agreement matrix (Lancichinetti and Fortunato, 2012) of the 100 module partition results for all subjects. Such a matrix gives how often two ROIs are in the same module. After normalization we get a matrix with values in the interval

[0,1]. The last step was to build the difference of the agreement matrices of different subject groups (UWS, MCS, healthy). Hence, we got a matrix with values in the interval [-1,1] which gives us information about how different the module structures of the different groups are with a 0 indicating nearly no difference and 1 and -1 showing high differences. In order to find significant results a permutation test (permuting the membership of the different groups) was performed with 1000 repetitions and a statistical significance value of 0.001 uncorrected was used (Wutzl et al., in prep.).

5.5.3.2. Classification

After comparing the agreement matrices, we turned toward classification. The aim was to use this multislice approach to classify one new subject to one of the three groups (healthy, MCS, or UWS). First of all, one subject which should be classified was chosen and then, was excluded from its group which were all randomly downsampled to the smallest group, namely MCS. Then we performed the same steps as shown in Figure 33 which resulted in agreement matrices for each group. After having those at hand we calculated a consensus modularity vector (Lancichinetti and Fortunato, 2012). Such a vector is a heuristic representation of the modular structure described by the agreement matrix. The calculation of the consensus vector via BCT needs two parameters. These are τ which gives the resolution of the reclustering, and the number of repetitions which describes how many reapplications of the clustering algorithms are performed. The next step was to compare the consensus vectors to the modularity structure of the previously chosen subject. Thus, we also needed a consensus vector for a single subject. To find such a consensus vector we first needed to determine an agreement matrix and thus modules. We tried three algorithms to find such modules. The first approach was to use the categorical method of Mucha et al. (Mucha et al., 2010) again. To do so, we used the same subject n times with n being the number of MCS patients included, i.e., the smallest number of subjects in one group. The next method was to use the command modularity_und of the BCT. This command applies Newman's spectral community detection to find modules for a single subject(Newman, 2006; Reichardt and Bornholdt, 2006). The last approach was the command community_louvain from BCT which uses the Louvain community detection algorithm with added finetuning to find modules (Blondel et al., 2008; Reichardt and Bornholdt, 2006; Ronhovde and Nussinov, 2009; Rubinov and Sporns, 2011; Sun et al., 2009). All these methods were then again repeated 100 times like for the multislice modularity approach, which also resulted in 100 modularity partitions from which we could build the agreement matrix which was again normalized. Now, having the agreement matrices of the groups (UWS, MCS and healthy) as well as for our chosen subject at hand we can calculate the consensus vector of

all the four groups and compare them using partition_distance (Meila, 2007). This method returns two outputs, i.e., normalized variation of information and normalized mutual information (see Definition 7 and Definition 9). We decided to use the first one as our measure. In order to find out which of the above-mentioned methods for modularity detection of the single subject give the best results, we used the F1-score (see Definition 20). We chose this metric because we have imbalanced sample sizes for which this method is more suitable than accuracy.

During our analyses we found that the F1-scores do not differ much when comparing the three different methods for modularity calculation of the single subject. However, the Louvain community approach gave slightly better results. Moreover, we found τ=0.35, again resulting in about 10 to 15 modules, i.e., brain networks, and a repetition of 100 to be suitable.

However, we assume that this measure (just measuring the partition distance of the consensus vectors) may not be very accurate because a lot of all 132 ROIs are included. Not all of these ROIs can be assumed to be equally important, i.e., some may just give noise. Hence, we decided to shorten the vector and just include the most important ROIs. These ROIs were considered as the most important ones which turned out to be statistically significant when comparing the module belongings (Wutzl et al., in prep.).

5.5.4. Results found when analyzing resting state fMRI data with networks and modularity

5.5.4.1. Results from the multislice modularity

When analyzing MCS or UWS patients versus healthy controls, we found that there were a lot of ROIs that had statistically significantly (at significance level 0.001 uncorrected) different module belonging when compared to a partner, namely 237 pairs (including 90 different ROIs) for healthy versus MCS and 321 pairs (including 111 ROIs) for healthy versus UWS. When comparing MCS and UWS patients we found a narrower result, i.e., just 7 ROI pairs were significant. These pairs mainly included the middle temporal gyrus, posterior division right. This ROI and the parietal operculum cortex left, the central operculum cortex left, the frontal operculum cortex left, the insular cortex left and right, as well as the Heschl's gyrus left were significantly less often in the same module in MCS

when compared to UWS. The two regions planum polare right and temporal pole left were more often in the same module.

5.5.4.2. Results from the classification

As described before we found a lot of significant results when comparing scDOC patients to healthy controls. Hence, we first run the algorithm without shortening the consensus vector. The confusion matrix of this algorithm is shown in Table 9.

Table 9: This table shows a confusion matrix using a consensus vector with all 132 ROIs, τ=0.35 and number of repetitions 100, and all other values were the same as in the modularity part. The table shows the real group and the one predicted from the classifier. (Wutzl et al., in prep.)

predicted \ real	UWS	MCS	Healthy
UWS	12	8	6
MCS	8	5	2
Healthy	9	7	22

The F1-score of this table is 0.4618 which is not bad for a classifier with three classes (a random classifier would give an F1-score of 0.3333). However, one has to take the whole confusion matrix into account. When looking at Table 9, we find that the good result comes from the separation of healthy subjects to scDOC. When calculating the F1-score for healthy versus scDOC we find that it is 0.6976, now comparing to 0.5, which is the result of a random classification. When grouping UWS patients and healthy together, we calculate an F1-score of 0.5419 which corresponds to a nearly random classifier. A similar result, i.e., an F1-score of 0.5686, is found for the groups MCS and healthy versus UWS. Thus, the fact that the classifier is better than random is just due to the good classification between patients and healthy subjects.

When considering daily-life applications, it is not so important to have a classifier which separates healthy subjects from patients but which separates the two patient groups because this is where a very high misdiagnosis rate is evident (see Section 3). Thus, we just focused on this inter-patient classification of MCS and UWS from now on. The first approach was again to use the entire consensus vector for the classification. The confusion matrix of this classifier is shown in Table 10.

Table 10: This table shows the confusion matrix of the classification algorithm with a consensus vector with all 132 ROIs. τ=0.35, number of repetitions 100, and the rest of the parameters were the same as in the section 5.5.3.1. (Wutzl et al., in prep.)

predicted \ real	UWS	MCS
UWS	17	12
MCS	12	8

This gives us an F1-score of 0.4931, in other words, a classification at random. This shows that using all the ROIs is very noisy and not suitable for such a fine classification. Hence, we shortened the consensus vector such that it only included the 9 ROIs that were found to be statistically important when comparing modules (see last Section 5.5.4.1). The following Table 11 shows a confusion matrix of the classifier if we use a consensus vector with just these 9 ROIs.

Table 11: Confusion matrix of the classifier if the consensus vector just consists of the nine important regions when comparing the agreement matrices of UWS and MCS. The parameters were the same as before. (Wutzl et al., in prep.)

predicted \ real	UWS	MCS
UWS	18	6
MCS	11	14

This confusion matrix gives an F1-score of 0.6576 which is higher than a random classifier with a value of 0.5. A closer look shows, that the classifier was able to classify 62.07% of the UWS patients and 70.00% of the MCS patients correctly. (Wutzl et al., in prep.)

5.5.5. Discussion of the analysis of resting state fMRI data with networks and modularity

We found many significant results, namely ROI pairs that belong to different modules, when comparing scDOC to healthy controls. Such a result is difficult to interpret. But we can conclude that the modularity structure of the brain is very different when comparing healthy controls and scDOC patients. When turning to the comparison of MCS and UWS patients we found a small number of different pairs in module belonging, namely nine ROIs or seven pairs. This shows that the multislice modularity approach can find differences where classical methods fail to find some. This is especially interesting for the comparison between MCS and UWS because the diagnosis of those is still challenging and every new information can be useful.

Turning to the classification we demonstrated that the approach to compare the consensus vectors of the different groups to a single test subject using normalized variation of information worked very well when distinguishing between healthy subjects and scDOC patients. This makes us conclude, first of all, that the method is reliable and works. Moreover, this result means that the modular structure of the brains of the different subject groups vary in a lot of ROIs. This is also what was found when comparing the agreement matrices of the different groups. On the other hand, the simple comparison of the consensus vector did not show significant results when trying to classify UWS and MCS patients, meaning that their module structure does not differ that much. Hence, we shortened the consensus vector to just the ROIs which turned out to be important when comparing the agreement matrices. Using this proposed approach, we could show that the classification gets better, and that the algorithm gives an F1-score which is higher than that of a random classifier. However, one might ask why the classification does not give even better results. We hypothesize that this is not due to a lack in quality of our method but rather lies in the fact that the JFK CRS-R was used as a ground truth for the reference data. This method is a behavioral measure and as such prone to misdiagnosis. Though our physicians gave their best, the misdiagnosis rate is something that cannot be neglected. Nonetheless, we claim that we would be able to achieve even better results, when using this method for a disease with less initial misdiagnoses. Nonetheless, this method is useful for the diagnosis of patients with scDOC. Furthermore, a larger dataset would make the classifier more accurate and then the second approach can be used to classify new patients. This method is of special interest, because all it uses is the resting state of an fMRI scan and thus is not biased by behavioral testing. Moreover, the method does not need the compliance of the patients, something that is of special interest when dealing with this patient group (Wutzl et al., in prep.).

5.5.6. Summary of the analysis of resting state fMRI data with networks and modularity

In the above, we presented techniques using the multislice approach of Mucha et al. (Mucha et al., 2010). We used this method to find the modules of the fMRI data of healthy subjects, MCS and UWS patients. The first part dealt with the comparison of agreement matrices which show the relative frequency of two ROIs being in the same module for one subject group. We could show that this method revealed differences where classical approaches fail to find some, i.e., in the module structure when comparing MCS and UWS patients. Moreover, the comparison of scDOC patients and healthy controls revealed a lot of different module assignments between ROI pairs. The second part introduces a new method for the classification of UWS and MCS patients as well as healthy subjects just according

to their fMRI resting state brain scans. We generated the consensus community vector from the agreement matrices and compared them using normalized variation of information. This gives good results when comparing scDOC to healthy controls, but just random classification for UWS versus MCS patients. Shortening the consensus vector to the ROIs found to be most important in the first step even made it possible to classify UWS and MCS patients with an F1-score better than a random classifier would give. Hence, we conclude that this method is useful for classifying fMRI resting state data into different groups and we hypothesize that the classification of a new patient would even be better if we would have more accurate diagnosis for the initial data set.

5.6. Using genetic algorithm and support vector classifier for feature selection

5.6.1. Introduction to the use of genetic algorithm and support vector classifier

When considering the misdiagnosis of the patients with scDOC, we find that a lot of effort was made to improve the results. Hence, in the last decades also interdisciplinary approaches have been used. Of these interdisciplinary methods machine learning seems to be useful for neuroimaging data (Lemm et al., 2011; Richiardi et al., 2013). Höller et al. divided scDOC patients into the different subgroups using EEG-features from an imagery paradigm (Höller et al., 2013). Zheng and colleagues used an approach with DTI and machine learning (Zheng et al., 2016). Moreover, Pugin et al. predicted the outcome of post-anoxic comatose patients after cardiac arrest according to their resting state fMRI scans also using machine learning (Pugin et al., 2018). Another study, which was conducted by Riganello et al. in 2018, showed that the heart rate variability entropy gives useful features for machine learning techniques to discriminate scDOC patients. Above all, classification methods, e.g., support vector classifier (SVC) (see Section 5.6.3), also combined with feature extraction, have been applied with success (Karamzadeh et al., 2015; Pereira et al., 2009; Sachdeva et al., 2013; Segovia et al., 2016). Most of these papers use feature extraction, i.e., the data are transformed from the feature space to some target space. This is done using, e.g., principal component analysis (PCA). For an exemplary paper see (Sachdeva et al., 2013). However, such an approach is difficult to interpret because the target space is usually not the feature space. Hence, it is difficult to find the significant features. This is why we turn to another approach, which is feature selection. This technique describes a method where input patterns are reduced to only the most important features. In the following we will use a combination of a genetic algorithm (GA) (see Section 5.6.2) and a SVC (see Section 5.6.3) for this feature selection. Such a combination has been used successfully in other research fields, see

for example (Frohlich et al., 2003; Huang and Wang, 2006; Salcedo-Sanz et al., 2002). Turning to the classification of fMRI data, we find that we have a high dimensional input space. Using the whole data as input features also includes a lot of irrelevant features for our classification. This can increase the computational cost and the runtime of the system and, what is even more important, lead to worse results. Thus, the aim is to find the features that contribute most to the classification process. We have to face the balancing act of wanting to include as little features as possible but also finding the best results of the SVC.

Before details of the method and the results are presented, a short introductions to GA as well as to SVC are given in the next two sections.

5.6.2. Genetic algorithm (GA)

We want to find the ROIs that are most important for the distinction between healthy controls and patient groups as well as between UWS and MCS patients. This is done via feature selection using a GA which is a form of evolutionary algorithm. Pioneer work for this algorithm was done by John Henry Holland (Holland, 1975). In the following, a brief introduction to the field of GA will be given, but for more details see, e.g., (Davis, 1991; Goldberg, 1989; Michalewicz, 1994). We follow in this section (Olariu and Zomaya, 2005) Chapter 16.

GAs are adaptive, efficient, randomized, and robust search and optimization processes. They use models from natural genetics and are most often used in multimodal, large and complex landscapes. GAs are based on natural genetic systems. The genetic information of every potential solution is stored in a structure called chromosome. A group of chromosomes is called a population. Biologically inspired operations are performed on the population in order to find a new and hopefully better solution. Like in nature, populations that are better suited to the environment survive and pass on their genetic information to the new generation (Olariu and Zomaya, 2005).

The essential components as defined by Olariu and Zomaya (Olariu and Zomaya, 2005) p. 236-237 are:

- *A representation strategy that determines the way in which potential solutions will be encoded to form string like structures called chromosomes.*
- *A population of chromosomes.*
- *Mechanism for evaluating each string (fitness function).*

- *Selection/reproduction procedure.*
- *Genetic operators (crossover and mutation).*
- *Probabilities to perform genetic operations.*

Figure 35 shows a typical workflow of a GA.

GAs operates on a chromosomal representation of a parameter set. This is encoded as a string of finite size using an alphabet of finite length. In general, chromosomes are binary strings of 1s and 0s. An example of such a binary chromosome of length 10 is

1 0 1 1 0 0 0 0 1 1.

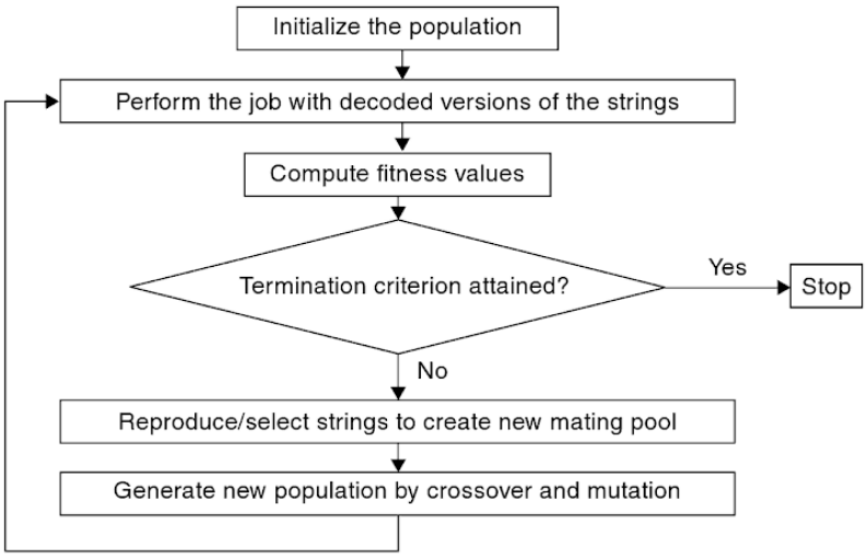

Figure 35: The GA starts with a random initialization of the population. The next step consists of performing the job with the decoded version of the strings. After that the fitness computation follows. Then it is checked whether the termination criterion has already been reached. If so, the algorithm stops, if not, strings are selected to create a new mating pool which is followed by crossover and mutation to generate a new population. This new population is now used instead of the previous population and the algorithm is repeated until the termination criterion is reached. (Olariu and Zomaya, 2005)

Thus, the number of different chromosomes is 2^n with n being the length of the chromosomes. Each chromosome stands for a possible solution. A population is a set of chromosomes in a generation. The size of such a population may be fixed or vary from one generation to another. Usually the initial population is chosen randomly.

The key point of a GA is the fitness function. It is the only information which is used by the GA to search the target space. Hence, it is crucial to define it right. The fitness function is chosen in such a way that good chromosomes have a high fitness.

The next important step is the selection or reproduction process. During this step, individual chromosomes, referred to as parent chromosomes, are copied into a new population called mating pool or children. If the number of copies of a chromosome is directly proportional to the value of the fitness function, it is called proportional selection scheme. However, there are different selection procedures, e.g., the stochastic universal selection, binary tournament selection or the roulette wheel parent selection. For details see, for example (Goldberg, 1989; Michalewicz, 1994). Moreover, an elite list is often used. Such a list consists of the chromosomes with the best fitness function values and are not changed from one step to the next.

The most often used genetic operations to change the parents into new children population are *mutation* and *crossover*.

Mutation describes random changes in the genetic structure of a chromosome. The easiest is the bit-by-bit mutation, i.e., each bit in a chromosome will be changed with a certain probability. The following shows an example of a mutation of position 4 in the above example chromosome of length 10.

1 0 1 **1** 0 0 0 0 1 1
1 0 1 **0** 0 0 0 0 1 1

Mutation provides genetic diversity in the population. It may be the case that the optimal solution is not represented in the genetic structure of the current population. Thus, the algorithm could not find the optimal solution without mutation.

Crossover, on the other hand, needs two input parent chromosomes. These chromosomes are combined to produce new children for the next generation. The most common used scheme is the so-called single point crossover. Other techniques are for example the two-point as well as multiple point crossover, the uniform and shuffle exchange crossover. Details can be found in, e.g., (Davis, 1991). Here, the single-point crossover is described. Such a crossover starts, by pairing the parent chromosomes at random. Then, crossover occurs with a crossover probability at a certain position of

the chromosome. The following shows an example of a crossover of our example chromosome of length 10 and another parent chromosome. The crossover is shown after bit 7 by a vertical bar.

1 0 1 1 0 0 0 |0 1 1
1 1 0 1 0 0 1 |1 0 1

After the crossover the children look like

1 0 1 1 0 0 0 **1 0 1**
1 1 0 1 0 0 1 **0 1 1.**

The GA runs until it reaches a termination criterion. Such a termination criterion can be manifold. Some of the most often used criteria are:

- A predefined value of the fitness function is obtained by at least one chromosome.
- The average fitness value does not change anymore with a new population.
- A certain number of generations has been reached.

What has not been mentioned up to now is that there are a lot of parameters that need to be finetuned and fixed by the programmer. The four most important parameters are the population size, the probabilities for crossover and mutation, as well as the termination criterion. Besides, there are also other parameters and adjustments need to be made within the algorithm depending in general on the given problem.

5.6.3. Support vector classifier (SVC)

We are using a support vector classifier (SVC) in our algorithm for which a brief introduction is given in the following. SVC are also called *support vector machines* or *support vector networks* and were introduced by Corinna Cortes and Vladimir Vapnik in 1995 (Cortes and Vapnik, 1995). SVC is a machine learning approach for a classification problem with two classes. The main idea is that the input vectors are mapped into a high dimensional feature space where they are separated by a hyperplane. For the formal definition we follow (Abe, 2010).

First, we start with a description of a hard-margin SVC. Let x_i (i=1, …, N) be n-dimensional input data which belong either to class 1 with label $y_i = 1$ or to class 2 with label $y_i = -1$. If the data are linearly separated, a decision function D can be found so that for all n-dimensional vectors *v*

$$\mathrm{D}(v) = w^{\mathrm{T}}v + b \tag{37}$$

with *w* being an n-dimensional vector and *b* a bias term. Moreover, for each i=1, …, N holds

$$w^T x_i + b \begin{cases} > 0 & \text{for} \quad y_i = 1 \\ < 0 & \text{for} \quad y_i = -1 \end{cases} . \tag{38}$$

Since the data are linearly separable, no x_i satisfies $w^{\mathrm{T}}x_i+b=0$ for i=1, …, N. So instead of the above we consider (with maybe different constants w and b)

$$w^T x_i + b \begin{cases} \geq 1 & \text{for} \quad y_i = 1 \\ \leq -1 & \text{for} \quad y_i = -1 \end{cases} \tag{39}$$

which is equivalent to

$$y_i(w^T x_i + b) \geq 1 \text{ for } i = 1, \dots, N . \tag{40}$$

The hyperplane given by

$$\mathrm{D}(v) = \mathrm{w}^{\mathrm{T}}v + b = c \text{ for } -1 < c < 1 \tag{41}$$

separates x_i (i=1, …, N) according to their classes. The distance between the separation hyperplane and the data sample x_i nearest to it is called *margin.* However, there is an infinite number of separating hyperplanes. Hence, the aim is to find the separating hyperplane with the maximum margin which is then called the *optimal separating hyperplane*. Figure 36 shows different separating hyperplanes and the optimal separating hyperplane with the maximal margin.

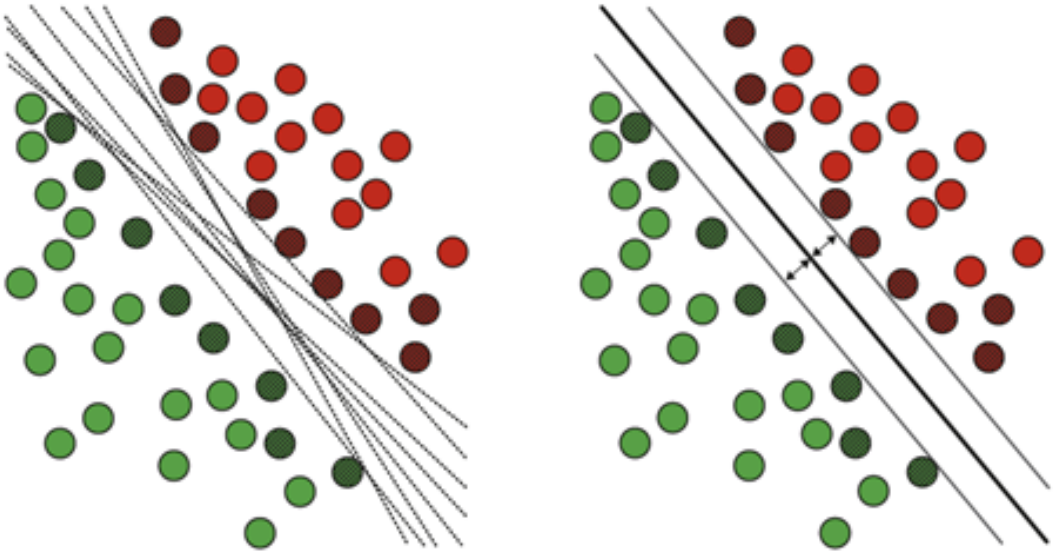

Figure 36: On the left-hand side different separating hyperplanes are shown for the two groups (red=group 1, green=group 2). On the right-hand side the optimal hyperplane is plotted with the maximum margin. Modified from (Koutsouleris et al., 2009).

When trying to find this optimally separating hyperplane, one has to consider the maximal distance of the margin points, i.e., points nearest to the margin. This maximal distance is reached when $c = 0$ in Equation (41). The next step is to find values for w and b. Now we take an arbitrary data point v and calculate its distance to the hyperplane. This is given by

$$\text{dist}(v, D) = \frac{|w^T v + b|}{\|w\|}. \tag{42}$$

We want to maximize this equation for our margin points. Now, let us consider a margin point x_M for which an equal sign holds in Equation (40). This gives

$$dist(x_M, D) = \frac{1}{\|w\|} \tag{43}$$

and thus, maximizing the margin is equivalent to minimizing $\|w\|$. In summary, one has to solve the following minimization problem for w and b

$$\text{minimize } Q(w, b) = \frac{1}{2}\|w\|^2 \tag{44}$$

$$\text{subject to } y_i(w^T x_i + b) \geq 1 \quad \text{for } i = 1, \ldots, N \tag{45}$$

where the factor ½ and the quadratic function are just introduced for mathematical convenience but do not change the problem per se.

The assumption we made before that the classes are linear separable means that there exist *w* and *b* that can satisfy Equation (44). Such a solution is called *feasible*. It is important to notice, that also if the solutions are not unique, the objective function is always unique. The points satisfying the equalities are the so-called *support vectors* which give the name to the whole algorithm.

Up to now we assumed that the data are linearly separable which is not the case in general. Now we will extend the above case so that the SVC is also applicable to inseparable cases. In order to do so we introduce the slack variable $\xi_i \geq 0$ into Equation (40)

$$y_i(w^T x_i + b) \geq 1 - \xi_i \text{ for } i = 1, \ldots, N \tag{46}$$

which leads to the following minimization problem

$$\text{minimize } Q(w, b, \xi) = \frac{1}{2}\|w\|^2 + \frac{C}{p}\sum_{i=1}^{N} \xi_i^p \tag{47}$$

$$\text{subject to } y_i(w^T x_i + b) \geq 1 - \xi_i, \quad \xi_i \geq 0 \quad \text{for } i = 1, \ldots, N \tag{48}$$

with C being the margin parameter, i.e., C gives the tradeoff between the minimization of the classification error and the maximization of the margin. The variable p can either be 1 or 2 and thus the SVC is either called L1 or L2 soft margin SVC.

What makes SVC so special is the introduction of so-called *kernels*. A kernel describes the way in which the scalar product is performed. The most common kernels are the linear kernel, polynomial kernels, exponential kernels, or the radial basis function kernel. The aforementioned kernels are just a few examples because basically any function can be used as a kernel. For more details see the corresponding literature, e.g., (Scholkopf and Smola, 2001).

5.6.4. Methods for the combination of GA and SVC

The first part of our analysis was done in CONN (see Section 5.3). From here on, we used python version 2.7 (Python Software Foundation, https://www.python.org/) for our calculations. The main part of the analysis was a GA (see Section 5.6.2 for an introduction). The starting point were the Fisher's Z transformed correlation matrices found with CONN (see Section 5.3) which consisted of 132 ROIs. All these 132 ROIs could be considered as features. Nevertheless, not all of them are

equally important for the classification of the different groups (healthy, MCS, and UWS). Thus, we aimed at finding the most important ones, i.e., those ROIs that contribute most to the classification of our three groups.

Different methods exist to select the most important features for classification, namely wrapper, filter, or embedded method. When using a filter method, the features are preselected during the preprocessing step. This is done with regards to a relevance measure which does not depend on the performance of the learning algorithm. The advantages of this method are that it is computationally effective and robust to overfitting. The wrapper approach describes a method where a subset of all features is used as input to the classifier. Then the performance is calculated and used as a relevance criterion for the selected subset. This method is more powerful than the filter method, but the disadvantages are that it is computationally more expensive and often has the problem of overfitting. The last method, the embedded approach, is a newly proposed method which combines feature selection directly with the learning algorithm (Blum and Langely, 1997; Guyon and Elisseeff, 2003; Kohavi and John, 1997; Weston et al., 2000).

The python library scikit-learn has already implemented some feature selection techniques (Pedregosa et al., 2011). These include for example the univariate feature selection technique SelectKBest, but also multivariate methods, e.g., Recursive Feature Elimination (Guyon et al., 2002). Nevertheless, all these algorithms do not achieve what we aimed for, namely using the single ROIs as features. We use correlation matrixes as input data for the algorithms. Hence, each entry is a feature of two ROIs, namely the correlation of ROI i to ROI j. We propose to use the meta-heuristic GA to determine a subset of single ROIs as features.

We started with randomly allocating 1s and 0s to our ROIs with a probability of 0.25. This means that each ROI got a 1 with a probability of 0.25. If the ROI was allocated a 1, it was considered in the classification algorithm. We applied the chromosome as a filter to the columns and rows of the correlation matrix, a 1 indicating that the ROI should be included and a 0 that it should not be included. Figure 37 shows a graphical representation of the procedure. The application of the binary ROI mask results in a smaller truncated correlation matrix (orange matrix in Figure 37). Since the correlation matrix is symmetric, we then extracted the upper triangular matrix of this smaller correlation matrix. This smaller matrix was then transformed into a feature vector for the SVC (see Section 5.6.3) which was then used for the classification process where the fitness function was determined.

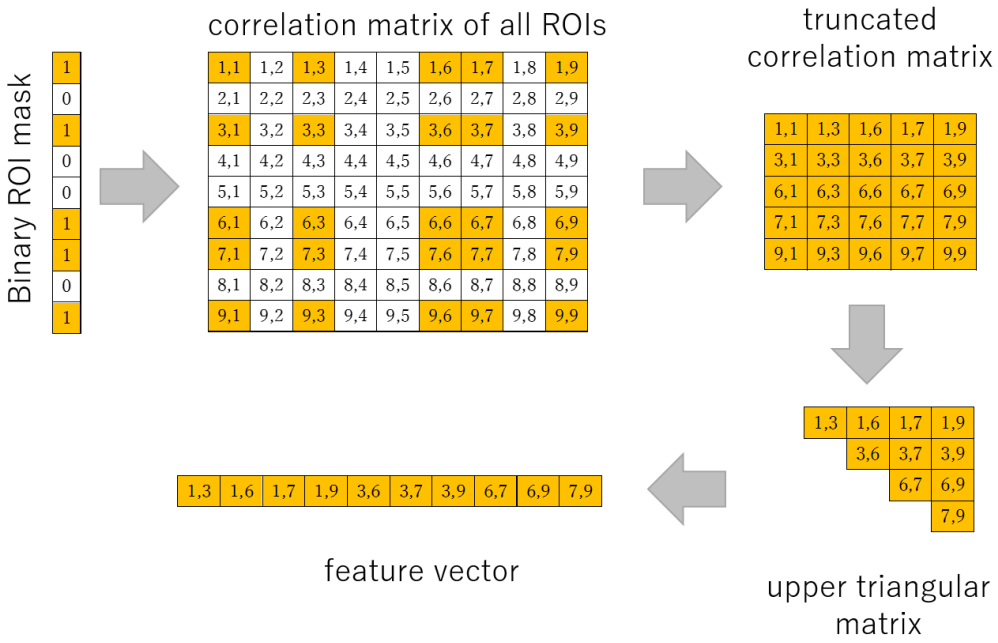

Figure 37: Representation of the used algorithm. In the upper row we have a binary ROI mask vector on the left-hand side as an individual of the GA. This vector is applied to the rows and columns of the correlation matrix in the middle of the upper row (in our algorithm this correlation matrix is a 132-by-132 matrix, however, for graphical representation only a 9-by-9 matrix is shown). Hence, just those combinations of ROIs which are both turned "on", i.e., indicated with an entry 1, are selected. This procedure results in a smaller truncated correlation matrix (orange matrix on the right-hand side of the upper row). Since it has symmetrical entries, its upper triangular matrix was extracted and then flattened into a feature vector for the use in the SVC. (Wutzl et al., in prep.)

As described in Figure 35 and Section 5.6.2 we needed to define a termination criterion. Our termination criterion made the GA repeat 1000 generations regardless of the value of the fitness function. What is worth mentioning is that the solution of a GA can just get better over time and never worse. Hence, if the algorithm finds a good solution it is kept until a better one is found. Thus, in the worst case it will yield as best solution the one it found in the very first generation.

The performance of a classifier is often evaluated with accuracy (see Definition 18) as metric. However, since this is not a good measure when dealing with different sample sizes, we use precision and recall (see Section 5.5.2.2). Hence, the precision and recall were calculated and plotted as a precision-recall curve of which the area under the curve (AUC) was used as the fitness function.

The other parameters for the GA were as follows. A population of 1000, number of generations 100, number of elites 5, i.e., 5 chromosomes were kept in every step, mutation probability of 0.1 – we just allowed the turning off of ROIs as mutation because our aim was to decrease the number of ROIs,

which were different between the groups. We tested all four possible combinations: healthy versus patients, healthy versus MCS, healthy versus UWS and MCS versus UWS.

Finally, we checked whether the performance of the classifier improved when choosing just the eleven most important ROIs for classification. We averaged over 100 train-test splits with a ratio of 0.33. Such a fraction means that an amount of 0.33 of the whole sample set is kept for testing and the rest is used for training (Wutzl et al., in prep.).

5.6.5. Results found by the combination of GA and SVC

Figure 38 shows one run of the GA when testing healthy subjects versus scDOC patients. The presented run found as the best solution the ROIs [7,14,33,71,110,123], i.e., (see Table 16) middle frontal gyrus right, precentral gyrus left, postcentral gyrus right, temporal fusiform cortex, posterior division left, cerebellum crus 2 right, and cerebellum 10 left. When considering just these selected ROIs for the SVC, a fitness (AUC of precision and recall curve) of one was obtained. The fitness rose to this value from an initial (randomly chosen ROIs) value of 0.85. However, one has to keep in mind that this is just one exemplary run and that different runs find different ROIs as best solutions. Hence, the algorithm was performed 1000 times to find the ROIs that are most often in the best fit solution.

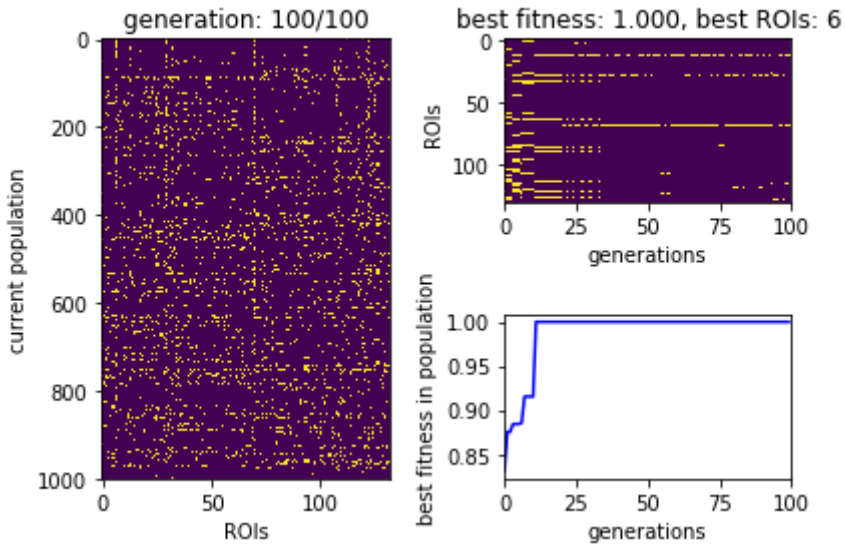

Figure 38: One exemplary run of the GA for heathy versus patients. Considering the color-coded matrix on the left-hand side, the yellow dots represent ones, i.e., those are the chosen ROIs. The x-axis shows the ROIs and the y-axis shows the population of the 100th generation. The upper figure on the right-hand side, shows the chosen ROIs (yellow dots) from the solution with the best fitness of each generation. This run ends with a solution, which has 6 ROIs, i.e., the ROIs [7,14,33,71,110,123]. The lower figure on the right-hand side represents the development of the best fitness of the population. Here it starts at an initial fitness value, i.e. the AUC of the precision and recall curve, of around 0.85 and ends at a fitness value of 1. (Wutzl et al., in prep.)

Considering the classification of healthy subjects versus scDOC patients we found that the ROI which was most often in the best fit solution was the postcentral gyrus right. This was also the most prominent one for the classification between healthy subjects versus MCS patients. The superior temporal gyrus posterior division right was the second most important one when distinguishing healthy subjects from patients and the postcentral gyrus left was the third most prominent one. When analyzing healthy subjects versus MCS, the insular cortex left and the postcentral gyrus left were the second and third most important ROIs. Turning to the third group (healthy versus UWS), the most important ROI was the superior temporal gyrus posterior division right. This ROI was also the second most prominent one when comparing healthy subjects versus scDOC patients. Caudate right and Vermis 3 were the second and third most important ROIs. Vermis 3 was also found to be essential when comparing healthy subjects and scDOC patients. Considering the comparison of MCS and UWS patients, we found the inferior temporal gyrus temporooccipital part left to be most crucial, the caudate left to be the second most important, and accumbens right to be the third most influential ROI. These did not show that much importance in any of the other separations. Nevertheless, we also found caudate right, inferior temporal gyrus anterior division left and temporal occipital fusiform cortex left to be significant when distinguishing healthy subjects and UWS patients, or UWS and MCS patients.

A histogram of all 1000 runs and their most important ROIs can be found in Figure 39 to Figure 42 showing all four combinations, namely Figure 39 shows healthy controls versus patients, Figure 40 healthy controls versus MCS patients, Figure 41 healthy controls versus UWS patients, and Figure 42 MCS versus UWS patients. The x-axis of all these histograms gives the number of the ROI in the CONN atlas (see Table 16 for the corresponding names) and the y-axis gives the frequency, i.e., how often this ROI was chosen to be in the best solution by the GA. Considering Figure 40, one finds that one ROI, namely postcentral gyrus right, is of special interest because its frequency bar towers significantly over the bars of the rest of the other ROIs. Looking at the other three histograms (Figure 39, Figure 41, and Figure 42) one also sees ROI bars that are higher than the others but those are not as pronounced as this one. A summary of the eleven most pronounced ROIs and their frequency can be found in Table 12 and Table 13.

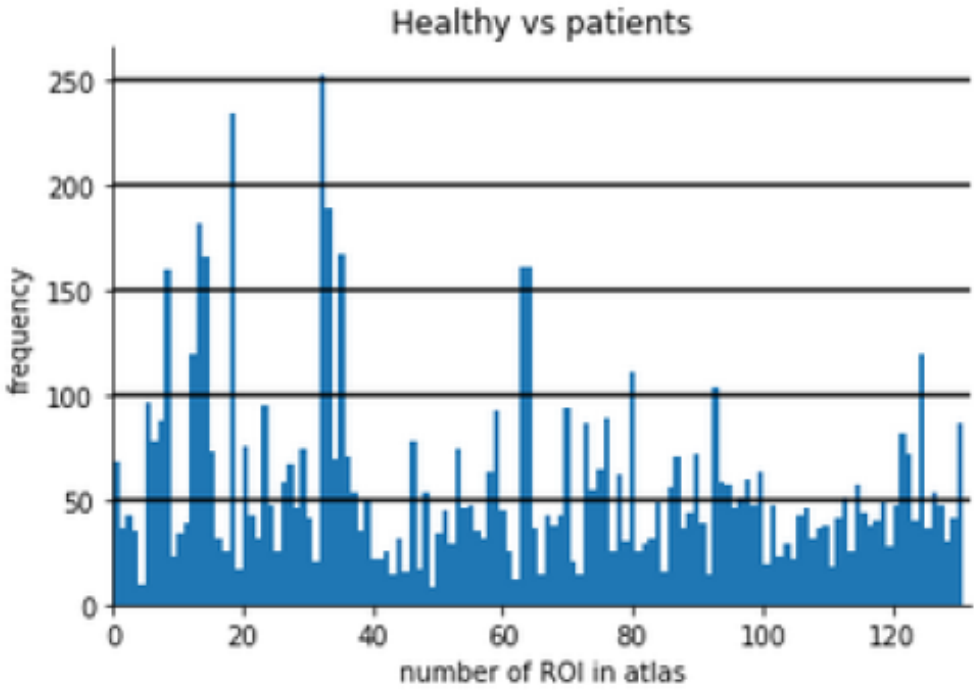

Figure 39: Frequency of the different ROIs when comparing healthy subjects to patients (MCS and UWS patients together). The x-axis gives the number of the ROI in the CONN atlas and the y-axis gives the frequency, i.e., how often the GA found this ROI to be part of the best solution when running 1000 times. (Wutzl et al., in prep.)

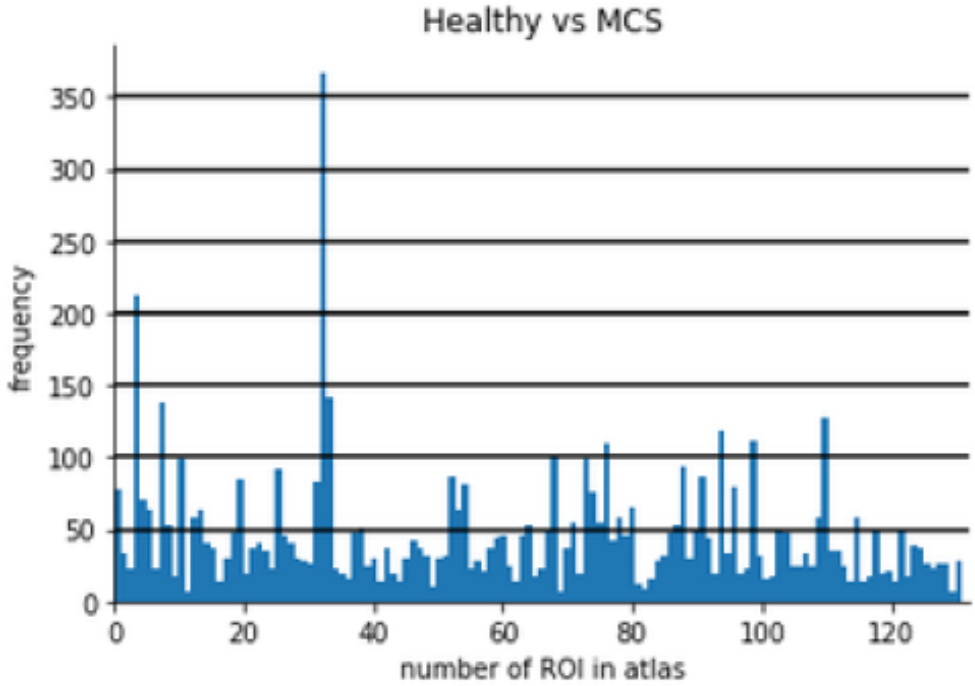

Figure 40: Frequency of the different ROIs when comparing healthy subjects to MCS patients. The x-axis gives the number of the ROI in the CONN atlas and the y-axis gives the frequency, i.e., how often the GA found this ROI to be part of the best solution when running 1000 times. (Wutzl et al., in prep.)

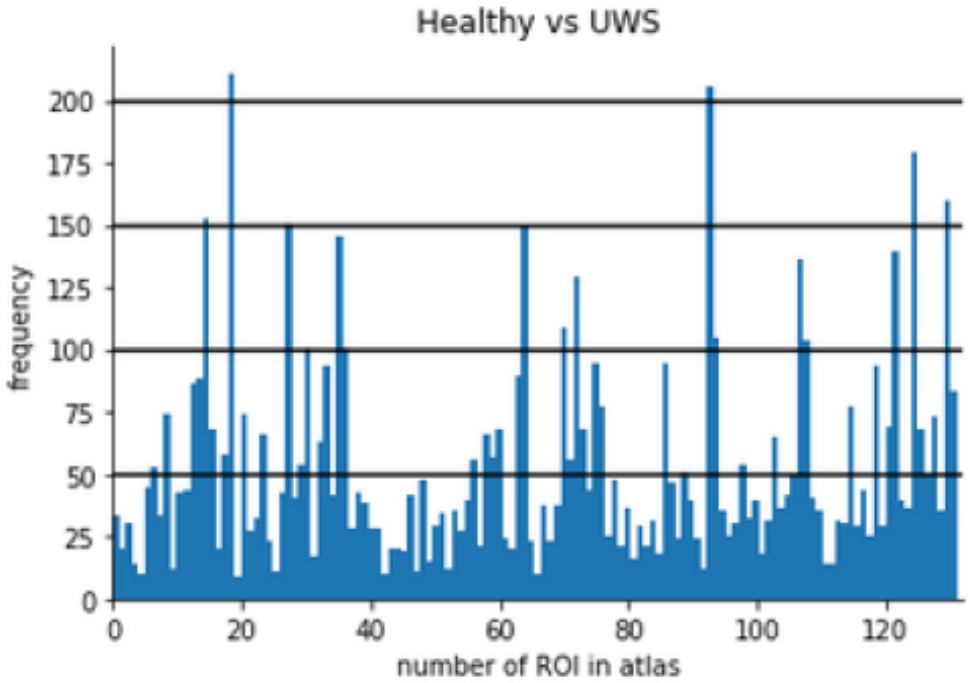

Figure 41: Frequency of the different ROIs when comparing healthy subjects to UWS patients. The x-axis gives the number of the ROI in the CONN atlas and the y-axis gives the frequency, i.e., how often the GA found this ROI to be part of the best solution when running 1000 times. (Wutzl et al., in prep.)

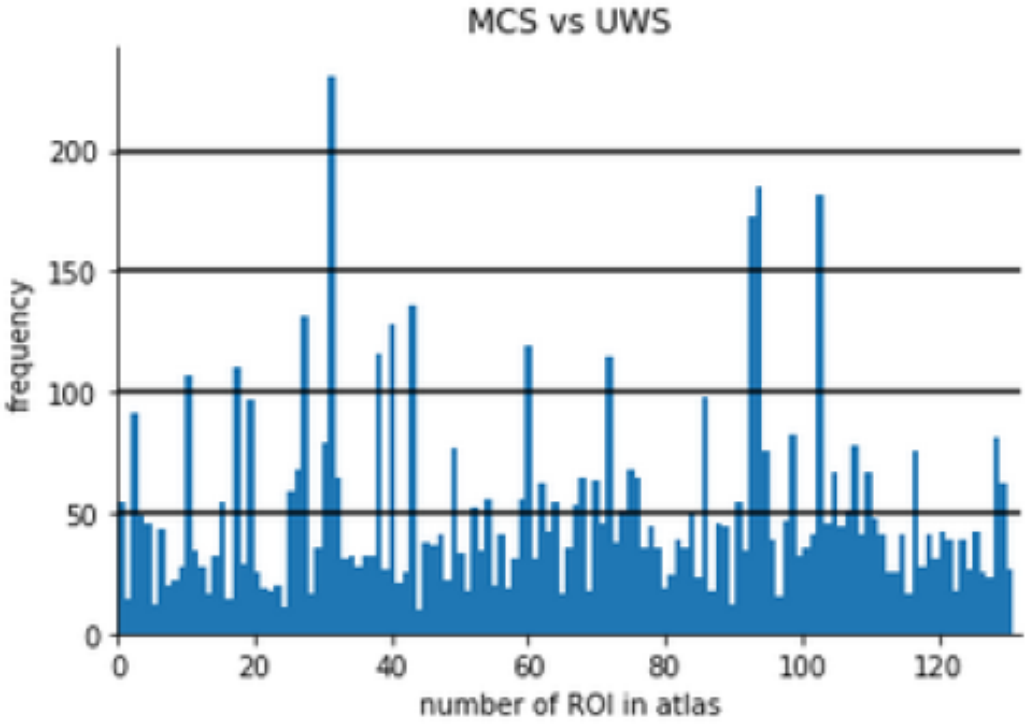

Figure 42: Frequency of the different ROIs when comparing MCS patients to UWS patients. The x-axis gives the number of the ROI in the CONN atlas and the y-axis gives the frequency, i.e., how often the GA found this ROI to be part of the best solution when running 1000 times. (Wutzl et al., in prep.)

Table 12: The eleven most pronounced ROIs (name: ROI, number in CONN atlas: Nr. and frequency: #), according to the GA, when comparing healthy subjects versus patients and healthy subjects versus MCS patients are shown in this table. Bold-marked ROIs show up more than once in this table or Table 13. (Wutzl et al., in prep.)

Healthy vs patients			Healthy vs MCS		
ROI	Nr.	#	ROI	Nr.	#
Postcentral Gyrus Right	**33**	253	**Postcentral Gyrus Right**	**33**	367
Superior Temporal Gyrus, posterior division Right	**19**	234	Insular Cortex Left	4	212
Postcentral Gyrus Left	**34**	189	**Postcentral Gyrus Left**	**34**	142
Precentral Gyrus Left	14	182	Middle Frontal Gyrus Left	8	138
Superior Parietal Lobule Left	36	167	Cerebelum 3 Left	111	128
Temporal Pole Right	**15**	166	Caudate Left	95	118
Parahippocampal Gyrus, posterior division Right	64	161	Hippocampus Right	100	111
Parahippocampal Gyrus, posterior division Left	**65**	161	Frontal Operculum Cortex Left	77	109
Inferior Frontal Gyrus, pars triangularis Right	9	160	Temporal Fusiform Cortex, anterior division Left	69	100
Precentral Gyrus Right	13	119	Inferior Frontal Gyrus, pars opercularis Right	11	99
Vermis 3	**126**	119	Occipital Fusiform Gyrus Right	74	99

Table 13: The eleven most pronounced ROIs (name: ROI, number in CONN atlas: Nr. and frequency: #), according to the GA, when comparing healthy subjects versus UWS patients and MCS versus UWS patients are shown in this table. Bold-marked ROIs show up more than once in this table or Table 12 . (Wutzl et al., in prep.)

Healthy vs UWS			MCS vs UWS		
ROI	Nr.	#	ROI	Nr.	#
Superior Temporal Gyrus, posterior division Right	**19**	211	Inferior Temporal Gyrus, temporooccipital part Left	32	231
Caudate Right	**94**	102	Caudate Left	95	185
Vermis 3	**126**	179	Accumbens Right	104	182
Vermis 9	131	160	**Caudate Right**	**94**	173
Temporal Pole Right	**15**	153	Lateral Occipital Cortex, superior division Left	44	136
Inferior Temporal Gyrus, anterior division Left	**28**	151	**Inferior Temporal Gyrus, anterior division Left**	**28**	131
Parahippocampal Gyrus, posterior division Left	**65**	150	Angular Gyrus Right	41	128
Superior Parietal Lobule Left	36	145	Frontal Orbital Cortex Left	61	119
Cerebelum 10 Left	123	139	Supramarginal Gyrus, posterior division Right	39	116
Cerebelum Crus1 Right	108	1036	**Temporal Occipital Fusiform Cortex Left**	**73**	115
Temporal Occipital Fusiform Cortex Left	**73**	129	Superior Temporal Gyrus, anterior division Left	18	110

The last step was comparing the performance of the classifier when eliminating all but the eleven most important ROIs for classification. Table 14 shows the accuracy and AUC of the precision and recall curve. These values were averaged over 100 train-test splits with a fraction of 0.33. We found that all the values increased for all the four combinations when comparing the initial value to the one found when just using the eleven ROIs that are most often in the best fit solution (Wutzl et al., in prep.).

Table 14: The table shows the accuracy and AUC of the precision and recall curve, when just using the eleven most important ROIs (Accuracy_11 and AUC_11) as well as for all 132 ROIs (Accuracy_132 and AUC_132) for the classification. The values are averaged over 100 runs using a train-test split with a fraction of 0.33. (Wutzl et al., in prep.)

	Healthy vs patient	**Healthy vs MCS**	**Healthy vs UWS**	**MCS vs UWS**
Accuracy_11	0.7096	0.7612	0.7880	0.7388
Accuracy_132	0.5163	0.4812	0.3645	0.5876
AUC_11	0.8239	0.7950	0.8871	0.8628
AUC_132	0.5018	0.3886	0.4116	0.6159

5.6.6. Discussion of the approach to combine GA and SVC for scDOC patients

The first finding is that the algorithm works and that it is applicable to patients with scDOC. The fact that some ROIs occur more often, namely for different comparisons, shows that the algorithm is consistent. Choosing the approach of feature selection gave us directly ROIs that are important for the classification and thus, do have different correlations with the rest of the ROIs, when comparing different groups.

Using the 11 most important features for the classification, the SVC gives better results than when using all of the ROIs. This shows that it is indeed better to use just a fraction of all the ROIs and that there are a lot of ROIs that just contribute noise and are not useful for the classification. Nearly all the values for 132 ROIs (see Table 14) are close to random, whereas using just the 11 most prominent ones give statistically significant results for the separation.

According to our findings the postcentral gyrus right seems to play an important role in MCS patients. Its frequency is highest when looking at the comparison of healthy controls versus patients and also it is especially pronounced in the case of healthy controls versus MCS. On the other hand, turning to UWS patients we find that the superior temporal gyrus, posterior division right is important because it has the highest frequency when comparing healthy controls and UWS patients and also is the second most important ROI for the comparison of healthy controls and patients. The distinction of MCS

versus UWS shows quite different results and only shows three ROIs that are also important in other comparisons, namely, healthy subjects versus UWS patients, but no same ROI to the comparison of healthy versus patients. Hence, we conclude that the separation of healthy versus scDOC patients is fundamentally different from the one of MCS and UWS patients. This sounds quite reasonable because there is a big gap between healthy and patients whereas the distinction between scDOC patients is quite difficult. Even though we concentrated here on finding the most important ROIs, it is not that easy. Often correlations of ROIs or even networks are altered in the different patient groups, for example Huntington's or Parkinson's disease (Göttlich et al., 2013; Werner et al., 2014).

This approach seems to be a promising tool in the field of neuroscience. Nevertheless, it has its limitations. The brainstem and the cerebellar anatomical regions are missing in the important ROIs. Brainstem lesions seem to play an important role in scDOC (Kampfl et al., 1998; Paterakis et al., 2000; Fischer et al., 2016). The fact, that these ROIs are missing among those found in the best fit solution, might be due to the way the atlas assigns the ROI regions. Thus, also other atlases have to be used in order to confirm our results. Furthermore, it would be interesting to analyze MCS+ versus MCS- patients as well as LIS and LIPS, because these have especially high misdiagnosis rate (see Section 3). In the future, the combination of GA and SVC shall also be applied to other neurological diseases, especially dementia, where specially supratentorial features can distinguish different pathological entities, e.g., in early stages of dementia or other neurogenerative diseases, Multiple Sclerosis, brain tumor, or cognitive and psychiatric disorders (Wutzl et al., in prep.).

5.6.7. Summary of the approach to combine GA and SVC for scDOC patients

We investigated scDOC patients and wanted to know which ones are the ROIs that show the biggest difference between the patient groups and healthy subjects. For this we used a combination of two approaches, namely GA and SVC, both being two well-established methods in data science. Nevertheless, we were the first, to our best knowledge, to use this combination for patients with scDOC. Several repetitions of the GA found different ROIs in each run to be important. The fact that we find different results each time lies in the nature of the GA. Hence, we ran the algorithm 1000 times and checked the ROIs that showed up most often. We looked at the eleven most prominent ROIs for each comparison, i.e., healthy controls versus scDOC patients, healthy controls versus MCS patients, healthy controls versus UWS patients, and MCS versus UWS patients. The results show that the algorithm is applicable to this patient group and found important ROIs for the separation. In the future, we hope that this algorithm can also help to investigate other neurological diseases.

6. Conclusion

Since the diagnosis of scDOC patients is still very challenging, a lot of misdiagnosis is made. This thesis tries to contribute to the understanding of these disorders and introduces new techniques, focusing on fMRI, that may help in the diagnosis of these patients.

After an introduction to fMRI as well as to scDOC, the first thing we showed was that a special task fMRI is possible for scDOC patients under anesthesia. This special task consisted of stimulating the patient on his extremities using a brush. This paradigm had shown robustness before, which is why we chose it for our experiments with anesthesia. Our results demonstrate for the first time, as far as we know, that this task fMRI is suitable for an investigation of an MCS patient as well as a patient in the final state of CJD. Before our experiment it was not even clear whether an fMRI would show results when anesthetizing a patient with scDOC. Moreover, it was believed that patients in the final stage of CJD are in the AS and do not activate the cerebral cortex anymore. We could report, as a novel result, that this was not true.

Then we turned to the analysis of resting state fMRI of patients with scDOC. In the first part we used a special connectivity software which revealed differences when comparing scDOC patients to healthy controls as well as one of the subgroups, i.e., MCS or UWS patients, to healthy controls. However, we did not find any differences between the connectivity of MCS and UWS patients. The fact that we detected significant differences between the other comparisons, shows that the connectivity of these patients and healthy controls is not the same. Nonetheless, we did not find any results between MCS and UWS patients which might be due to the diversity of the disorders, making it difficult to find statistically significant differences between the subgroups of scDOC.

The next part dealt with the approach of multislice modularity. This method was applied for the first time, to our best knowledge, to the data of scDOC patients. Moreover, a new classifier was introduced. We used this approach to first find different module assignments in the three classes of healthy controls, MCS, and UWS patients. When comparing healthy subjects to either group of scDOC patients we found many different module assignments, which made us conclude that the brains of healthy subjects and those of patients are very different when it comes to modules. On the other hand, when considering UWS versus MCS patients we found seven different module assignments. The fact that there are such little significant differences is due to the manifold disease patterns of scDOC. Hence, these results are even more important because, despite the different causes of the disorders,

similarities were found. Then we turned to the new classifier which was based on this multislice modularity calculation. This new classifier was able to distinguish healthy subjects and patients with scDOC very well but had problems when it came to the separation of UWS and MCS patients. Hence, we modified the classifier to just take the ROIs, which turned out to be important in the modularity assignment part. This allowed us to find a classifier that was statistically better than random when classifying MCS versus UWS patients and thus, could assist physicians in their decision making when diagnosing these patients.

The last part deals with a combination of GA and SVC which is a well-established composition but has never, as far as we know, been used for feature selection of this patient group. We truncated the correlation matrix in a special way so that we just include some preselected ROIs. Thus, were able to find those ROIs that are most different when comparing the patient groups as well as healthy controls.

The work presented contributes to the literature in the way that it shows for the first time that scDOC patients can be anesthetized for their fMRI investigation, at least for such a robust task fMRI. This finding will make it a lot easier for physicians in the future because this patient group does not tolerate fMRI examinations very well and it would be a lot more comfortable for the patients if they were anesthetized. Nonetheless, different tasks and also resting state fMRI should be tested in the future so that maybe the whole fMRI examination can be done under anesthesia and not only a somatosensory paradigm. Moreover, our technique gave the novel insight that the diagnosis of AS is not appropriate for patients in the final stage of CJD.

The new analysis method for resting state fMRI using the multislice modularity approach of Mucha et al. (Mucha et al., 2010) leads to a classifier that is better than random when classifying the different disorders. Hence, it could assist the physician in determining diagnoses. It is of special interest because the classifier just uses resting state fMRI and as such is not prone to misdiagnoses relying on behavioral testing. However, the results of the classifier have room for improvement. The weak spots are, on the one hand, the misdiagnosis rate of MCS and UWS patients that we had to include, in lack of another option, as ground truth and, on the other hand, our sample size was not very large. It was large enough for finding results, but a more reliable result needs a larger sample size. Furthermore, we hypothesize, that our method is suitable for other brain disorders and would give even better results when classifying a disease with a lower misdiagnosis rate for the training set.

The GA and SVC approach is also suitable for other diseases, especially for those whose damage is located to a single brain areas. This is of course not proven yet and is something that should be done

in the future. Perhaps, the combination of GA and SVC, as well as the multlislice technique can help to understand even more brain diseases.

7. Supplemental material

Table 15: Overview of the patients included in the study. The table gives the number of the subject, UWS indicating UWS patients, MCS indicating MCS patients and missing indicates a missing diagnosis for UWS or MCS but the patient had scDOC. Moreover, the age, sex, time since onset, the etiology and the used scanner are listed. (Wutzl et al., in prep., in prep.b)

subject	age [yr]	sex	time since onset [d]	etiology	scanner
UWS1	45	F	64	traumatic brain injury	3 T Philips
UWS2	45	M	635	cardiopulmonary resuscitation	3 T Philips
UWS3	50	M	204	cardiopulmonary resuscitation	3 T Philips
UWS4	69	M	58	cardiopulmonary resuscitation	3 T Philips
UWS5	39	F	73	respiratory failure	3 T Philips
UWS6	47	M	65	cardiopulmonary resuscitation	3 T Philips
UWS7	45	M	182	traumatic brain injury	3 T Philips
UWS8	29	F	104	basilar thrombosis	3 T Philips
UWS9	78	M	39	cardiopulmonary resuscitation	3 T Philips
UWS10	47	F	51	Multiple ischemic infarct	3 T Philips
UWS11	63	M	16	subarachnoid hemorrhage	3 T Philips
UWS12	51	M	30	cardiopulmonary resuscitation	3 T Philips
UWS13	50	M	165	Ischemic brainstem infarct	3 T Siemens
UWS14	51	F	1474	cardiopulmonary resuscitation	3 T Siemens
UWS15	38	F	78	subarachnoid hemorrhage	3 T Siemens
UWS16	55	F	121	cardiopulmonary resuscitation	3 T Siemens
UWS17	61	M	116	traumatic brain injury	3 T Siemens
UWS18	26	M	124	traumatic brain injury	3 T Siemens
UWS19	55	M	47	metabolic encephalopathy	3 T Siemens
UWS20	54	M	70	cardiopulmonary resuscitation	3 T Siemens
UWS21	59	M	20	traumatic brain injury	3 T Siemens
UWS22	55	M	182	cardiopulmonary resuscitation	3 T Siemens
UWS23	73	M	59	traumatic brain injury	3 T Siemens
UWS24	43	M	68	cardiopulmonary resuscitation	3 T Siemens
UWS25	52	M	611	venous sinus thrombosis	3 T Siemens

UWS26	82	M	27	cardiopulmonary resuscitation	3 T Siemens
UWS27	68	M	43	cardiopulmonary resuscitation	3 T Siemens
UWS28	30	M	502	traumatic brain injury	3T Siemens
UWS29	18	M	569	hyperthermia	3 T Siemens
UWS30	18	M	41	encephalopathy	3 T Siemens
UWS31	17	M	94	encephalopathy	3 T Siemens
UWS32	33	M	80	encephalopathy	3 T Siemens
UWS33	48	F	missing	intracerebral hemorrhage	3 T Siemens
UWS34	66	M	60	traumatic brain injury	3 T Siemens
MCS1	40	M	1887	traumatic brain injury	3 T Philips
MCS2	54	F	640	subarachnoid hemorrhage	3 T Philips
MCS3	51	M	102	intracerebral hemorrhage	3 T Philips
MCS4	37	M	67	respiratory failure	3 T Philips
MCS5	47	M	49	PICA infarct	3 T Philips
MCS6	47	M	52	traumatic brain injury	3 T Siemens
MCS7	34	M	51	traumatic brain injury	3 T Siemens
MCS8	54	F	74	subarachnoid hemorrhage	3 T Siemens
MCS9	46	M	34	multiple cerebral infarct	3 T Siemens
MCS10	65	M	85	intracerebral hemorrhage	3 T Siemens
MCS11	31	M	66	traumatic brain injury	3 T Siemens
MCS12	52	M	146	subarachnoid hemorrhage	3 T Siemens
MCS13	71	F	355	subarachnoid hemorrhage	3 T Siemens
MCS14	66	F	224	intracerebral hemorrhage	3 T Siemens
MCS15	53	F	100	subarachnoid hemorrhage	3 T Siemens
MCS16	41	F	40	cardiopulmonary resuscitation	3 T Siemens
MCS17	71	F	70	cardiopulmonary resuscitation	3 T Siemens
MCS18	43	M	75	traumatic brain injury	3 T Siemens
MCS19	32	F	37	encephalitis	3 T Siemens
MCS20	33	M	91	encephalitis	3 T Siemens
MCS21	85	M	66	subarachnoid hemorrhage	3 T Siemens
MCS22	18	M	937	traumatic brain injury	3 T Siemens
Missing1	20	M	missing	missing	3 T Siemens
Missing2	19	M	missing	missing	3 T Siemens

Table 16: Table of all the ROIs of the CONN atlas (Whitfield-Gabrieli and Nieto-Castanon, 2012)

Number of ROI	Region	Number of ROI	Region
1	Frontal Pole Right	67	Lingual Gyrus Left
2	Frontal Pole Left	68	Temporal Fusiform Cortex, anterior division Right
3	Insular Cortex Right	69	Temporal Fusiform Cortex, anterior division Left
4	Insular Cortex Left	70	Temporal Fusiform Cortex, posterior division Right
5	Superior Frontal Gyrus Right	71	Temporal Fusiform Cortex, posterior division Left
6	Superior Frontal Gyrus Left	72	Temporal Occipital Fusiform Cortex Right
7	Middle Frontal Gyrus Right	73	Temporal Occipital Fusiform Cortex Left
8	Middle Frontal Gyrus Left	74	Occipital Fusiform Gyrus Right
9	Inferior Frontal Gyrus, pars triangularis Right	75	Occipital Fusiform Gyrus Left
10	Inferior Frontal Gyrus, pars triangularis Left	76	Frontal Operculum Cortex Right
11	Inferior Frontal Gyrus, pars opercularis Right	77	Frontal Operculum Cortex Left
12	Inferior Frontal Gyrus, pars opercularis Left	78	Central Opercular Cortex Right
13	Precentral Gyrus Right	79	Central Opercular Cortex Left
14	Precentral Gyrus Left	80	Parietal Operculum Cortex Right
15	Temporal Pole Right	81	Parietal Operculum Cortex Left
16	Temporal Pole Left	82	Planum Polare Right
17	Superior Temporal Gyrus, anterior division Right	83	Planum Polare Left
18	Superior Temporal Gyrus, anterior division Left	84	Heschl's Gyrus Right
19	Superior Temporal Gyrus, posterior division Right	85	Heschl's Gyrus Left
20	Superior Temporal Gyrus, posterior division Left	86	Planum Temporale Right
21	Middle Temporal Gyrus, anterior division Right	87	Planum Temporale Left
22	Middle Temporal Gyrus, anterior division Left	88	Supracalcarine Cortex Right
23	Middle Temporal Gyrus, posterior division Right	89	Supracalcarine Cortex Left
24	Middle Temporal Gyrus, posterior division Left	90	Occipital Pole Right
25	Middle Temporal Gyrus, temporooccipital part Right	91	Occipital Pole Left
26	Middle Temporal Gyrus, temporooccipital part Left	92	Thalamus Right
27	Inferior Temporal Gyrus, anterior	93	Thalamus Left

	division Right		
28	Inferior Temporal Gyrus, anterior division Left	94	Caudate Right
29	Inferior Temporal Gyrus, posterior division Right	95	Caudate Left
30	Inferior Temporal Gyrus, posterior division Left	96	Putamen Right
31	Inferior Temporal Gyrus, temporooccipital part Right	97	Putamen Left
32	Inferior Temporal Gyrus, temporooccipital part Left	98	Pallidum Right
33	Postcentral Gyrus Right	99	Pallidum Left
34	Postcentral Gyrus Left	100	Hippocampus Right
35	Superior Parietal Lobule Right	101	Hippocampus Left
36	Superior Parietal Lobule Left	102	Amygdala Right
37	Supramarginal Gyrus, anterior division Right	103	Amygdala Left
38	Supramarginal Gyrus, anterior division Left	104	Accumbens Right
39	Supramarginal Gyrus, posterior division Right	105	Accumbens Left
40	Supramarginal Gyrus, posterior division Left	106	Brain-Stem
41	Angular Gyrus Right	107	Cerebelum Crus1 Left
42	Angular Gyrus Left	108	Cerebelum Crus1 Right
43	Lateral Occipital Cortex, superior division Right	109	Cerebelum Crus2 Left
44	Lateral Occipital Cortex, superior division Left	110	Cerebelum Crus2 Right
45	Lateral Occipital Cortex, inferior division Right	111	Cerebelum 3 Left
46	Lateral Occipital Cortex, inferior division Left	112	Cerebelum 3 Right
47	Intracalcarine Cortex Right	113	Cerebelum 4 5 Left
48	Intracalcarine Cortex Left	114	Cerebelum 4 5 Right
49	Frontal Medial Cortex	115	Cerebelum 6 Left
50	Juxtapositional Lobule Cortex - formerly Supplementary Motor Cortex- Right	116	Cerebelum 6 Right
51	Juxtapositional Lobule Cortex - formerly Supplementary Motor Cortex- Left	117	Cerebelum 7b Left
52	Subcallosal Cortex	118	Cerebelum 7b Right
53	Paracingulate Gyrus Right	119	Cerebelum 8 Left
54	Paracingulate Gyrus Left	120	Cerebelum 8 Right
55	Cingulate Gyrus, anterior division	121	Cerebelum 9 Left
56	Cingulate Gyrus, posterior division	122	Cerebelum 9 Right
57	Precuneous Cortex	123	Cerebelum 10 Left
58	Cuneal Cortex Right	124	Cerebelum 10 Right
59	Cuneal Cortex Left	125	Vermis 1 2
60	Frontal Orbital Cortex Right	126	Vermis 3

61	Frontal Orbital Cortex Left	127	Vermis 4 5
62	Parahippocampal Gyrus, anterior division Right	128	Vermis 6
63	Parahippocampal Gyrus, anterior division Left	129	Vermis 7
64	Parahippocampal Gyrus, posterior division Right	130	Vermis 8
65	Parahippocampal Gyrus, posterior division Left	131	Vermis 9
66	Lingual Gyrus Right	132	Vermis 10

Table 17: Number of average modules of the Gen Louvain algorithm with a repetition of 10 and the total number of 29 UWS patient varying γ from 0.25 to 4.0 with an increment of 0.25 and ω from 0.1 to 1.0.

γ \ ω	**0.1**	**0.2**	**0.4**	**0.6**	**0.8**	**1.0**
0.25	1.0	1.0	1.0	1.0	1.0	1.0
0.5	1.4	1.0	1.0	1.0	1.0	1.0
0.75	3.7	2.0	2.0	2.0	2.0	2.0
1.0	5.4	3.6	4.3	4.3	4.5	4.3
1.25	7.2	6.1	6.4	6.6	6.7	6.7
1.5	9.2	7.8	9.3	9.2	9.3	9.9
1.75	11.1	9.6	11.3	11.0	11.1	11.3
2.0	13.2	12.3	13.5	14.0	13.9	12.9
2.25	16.6	15.8	17.2	18.1	17.9	17.7
2.5	19.6	19.9	21.5	21.4	21.3	21.9
2.75	23.2	24.1	24.6	24.4	24.0	24.6
3.0	28.4	28.8	28.8	29.3	29.3	29.1
3.25	33.1	32.0	32.0	33.2	33.4	32.7
3.5	40.1	37.8	37.8	36.8	37.4	37.6
3.75	44.3	42.2	42.6	42.3	41.8	42.0
4.0	49.2	45.9	45.8	45.5	45.2	45.9

Table 18: Number of average modules of the Gen Louvain algorithm with a repetition of 10 and the total number of 20 MCS patient varying γ from 0.25 to 4.0 with an increment of 0.25 and ω from 0.1 to 1.0.

γ \ ω	**0.1**	**0.2**	**0.4**	**0.6**	**0.8**	**1.0**
0.25	1.2	1.0	1.0	1.0	1.0	1.0
0.5	2.0	1.2	1.0	1.0	1.0	1.0
0.75	4.0	2.3	2.0	2.0	2.0	2.0
1.0	5.5	4.4	3.4	3.8	3.9	3.9
1.25	8.2	6.4	6.1	5.9	6.1	6.0
1.5	10.8	9.0	10.1	10.3	10.5	10.3
1.75	13.8	11.4	13.1	13.3	12.7	12.9
2.0	17.0	14.5	16.5	15.8	15.6	15.9
2.25	20.0	17.9	20.1	19.1	18.9	20.1
2.5	22.9	21.2	24.2	24.7	23.4	23.9
2.75	27.0	26.4	30.2	29.8	28.6	29.1
3.0	31.4	31.2	33.7	33.7	33.1	32.5
3.25	35.3	37.1	38.4	38.9	38.4	37.9
3.5	40.0	42.7	45.4	45.1	43.9	43.4
3.75	44.7	48.2	50.9	51.6	50.2	49.7
4.0	49.9	56.0	57.4	56.8	56.3	58.6

Table 19: Number of average modules of the Gen Louvain algorithm with a repetition of 10 and the total number of 30 healthy controls varying γ from 0.25 to 4.0 with an increment of 0.25 and ω from 0.1 to 1.0.

γ \ ω	**0.1**	**0.2**	**0.4**	**0.6**	**0.8**	**1.0**
0.25	1.0	1.0	1.0	1.0	1.0	1.0
0.5	2.2	1.0	1.4	1.4	1.9	1.7
0.75	3.8	2.8	3.0	3.0	3.0	3.0
1.0	5.1	4.4	4.1	4.7	4.3	4.6
1.25	6.7	5.7	6.3	6.2	6.3	6.3
1.5	8.2	7.1	8.4	7.7	7.6	8.1
1.75	10.0	8.2	10.5	10.2	9.9	10.1
2.0	12.3	10.7	12.3	12.2	12.4	12.6
2.25	14.1	12.3	14.4	14.2	14.2	14.3
2.5	17.1	14.8	16.9	16.3	15.8	16.4
2.75	20.0	18.0	18.5	18.4	18.5	18.4
3.0	23.6	20.6	20.0	20.3	20.4	20.0
3.25	27.0	22.1	21.6	21.8	20.8	21.8
3.5	32.7	26.3	25.9	26.0	25.6	25.8
3.75	36.2	29.2	29.0	29.8	30.0	28.8
4.0	41.8	35.4	35.9	35.7	36.2	36.7

References

Abdulmassih, R., Min, Z., 2016. An ominous radiographic feature: cortical ribbon sign. Intern. Emerg. Med. 11, 281–283. doi:10.1007/s11739-015-1287-4

Abe, S., 2010. Support Vector Machines for Pattern Classification. Springer Science & Business Media.

Achard, S., Delon-Martin, C., Vértes, P.E., Renard, F., Schenck, M., Schneider, F., Heinrich, C., Kremer, S., Bullmore, E.T., 2012. Hubs of brain functional networks are radically reorganized in comatose patients. Proc. Natl. Acad. Sci. U. S. A. 109, 20608–20613. doi:10.1073/pnas.1208933109

Afifi, A.K., 2003. The basal ganglia: a neural network with more than motor function. Semin. Pediatr. Neurol. 10, 3–10.

Amaro, E., Barker, G.J., 2006. Study design in fMRI: Basic principles. Brain Cogn. 60, 220–232. doi:10.1016/j.bandc.2005.11.009

Andoh, J., Matsushita, R., Zatorre, R.J., 2015. Asymmetric Interhemispheric Transfer in the Auditory Network: Evidence from TMS, Resting-State fMRI, and Diffusion Imaging. J. Neurosci. Off. J. Soc. Neurosci. 35, 14602–14611. doi:10.1523/JNEUROSCI.2333-15.2015

Andrews, K., Murphy, L., Munday, R., Littlewood, C., 1996. Misdiagnosis of the vegetative state: retrospective study in a rehabilitation unit. BMJ 313, 13–16.

Ansell, B.J., Keenan, J.E., 1989. The Western Neuro Sensory Stimulation Profile: a tool for assessing slow-to-recover head-injured patients. Arch. Phys. Med. Rehabil. 70, 104–108.

Ardila, A., Bernal, B., Rosselli, M., 2016. How Localized are Language Brain Areas? A Review of Brodmann Areas Involvement in Oral Language. Arch. Clin. Neuropsychol. Off. J. Natl. Acad. Neuropsychol. 31, 112–122. doi:10.1093/arclin/acv081

Australian Department of Health and Aging, 2008. Infection Control Guidelines (Part 4-31).

Balasubramani, P.P., Chakravarthy, V.S., Ali, M., Ravindran, B., Moustafa, A.A., 2015. Identifying the Basal Ganglia network model markers for medication-induced impulsivity in Parkinson's disease patients. PloS One 10, e0127542. doi:10.1371/journal.pone.0127542

Bandettini, P.A., Wong, E.C., Hinks, R.S., Tikofsky, R.S., Hyde, J.S., 1992. Time course EPI of human brain function during task activation. Magn. Reson. Med. 25, 390–397.

Bauby, J.-D., 1998. Schmetterling und Taucherglocke, Neuauflage. ed. dtv Verlagsgesellschaft, München.

Bauer, G., Gerstenbrand, F., Rumpl, E., 1979. Varieties of the locked-in syndrome. J. Neurol. 221, 77–91.

Becker, E.D., 2007. Paul Christian Lauterbur. Phys. Today 60, 77–78. doi:10.1063/1.2761815

Beckmann, C.F., DeLuca, M., Devlin, J.T., Smith, S.M., 2005. Investigations into resting-state connectivity using independent component analysis. Philos. Trans. R. Soc. Lond. B. Biol. Sci. 360, 1001–1013. doi:10.1098/rstb.2005.1634

Bekinschtein, T., Cologan, V., Dahmen, B., Golombek, D., 2009. You are only coming through in waves: wakefulness variability and assessment in patients with impaired consciousness. Prog. Brain Res. 177, 171–189. doi:10.1016/S0079-6123(09)17712-9

Bell, A.J., Sejnowski, T.J., 1995. An Information-Maximization Approach to Blind Separation and Blind Deconvolution. Neural Comput. 7, 1129–1159. doi:10.1162/neco.1995.7.6.1129

Benjamini, Y., Hochberg, Y., 1995. Controlling the False Discovery Rate: A Practical and Powerful Approach to Multiple Testing. J. R. Stat. Soc. Ser. B Methodol. 57, 289–300.

Benzer, A., Mitterschiffthaler, G., Marosi, M., Luef, G., Pühringer, F., De La Renotiere, K., Lehner, H., Schmutzhard, E., 1991. Prediction of non-survival after trauma: Innsbruck Coma Scale. Lancet Lond. Engl. 338, 977–978.

Bernat, J.L., 2006. Chronic disorders of consciousness. Lancet Lond. Engl. 367, 1181–1192. doi:10.1016/S0140-6736(06)68508-5

Binder, J.R., Frost, J.A., Hammeke, T.A., Bellgowan, P.S., Rao, S.M., Cox, R.W., 1999. Conceptual

processing during the conscious resting state. A functional MRI study. J. Cogn. Neurosci. 11, 80–95.
Birbaumer, N., Ghanayim, N., Hinterberger, T., Iversen, I., Kotchoubey, B., Kübler, A., Perelmouter, J., Taub, E., Flor, H., 1999. A spelling device for the paralysed. Nature 398, 297. doi:10.1038/18581
Birbaumer, N., Schmidt, R.F., 1999. Biologische Psychologie, 4., vollst. überarb. u. erg. ed. Springer, Berlin.
Birn, R.M., Bandettini, P.A., Cox, R.W., Shaker, R., 1999. Event-related fMRI of tasks involving brief motion. Hum. Brain Mapp. 7, 106–114.
Biswal, B., Yetkin, F.Z., Haughton, V.M., Hyde, J.S., 1995. Functional connectivity in the motor cortex of resting human brain using echo-planar MRI. Magn. Reson. Med. 34, 537–541.
Biswal, B.B., 2012. Resting state fMRI: a personal history. NeuroImage 62, 938–944. doi:10.1016/j.neuroimage.2012.01.090
Biswal, B.B., Van Kylen, J., Hyde, J.S., 1997. Simultaneous assessment of flow and BOLD signals in resting-state functional connectivity maps. NMR Biomed. 10, 165–170.
Blakemore, S.-J., 2008. The social brain in adolescence. Nat. Rev. Neurosci. 9, 267–277. doi:10.1038/nrn2353
Bleaney, B., 1999. Edward Mills Purcell. 30 August 1912 — 7 March 1997: Elected For.Mem.R.S. 1989. Biogr. Mem. Fellows R. Soc. 45, 437–447. doi:10.1098/rsbm.1999.0029
Blondel, V.D., Guillaume, J.-L., Lambiotte, R., Lefebvre, E., 2008. Fast unfolding of communities in large networks. J. Stat. Mech. Theory Exp. 2008, P10008. doi:10.1088/1742-5468/2008/10/P10008
Blum, A.L., Langely, P., 1997. Selection of relevant features and examples in machine learning. Artif. Intell. 97, 245–271. doi:10.1016/S0004-3702(97)00063-5
Boesch, C., 2004. Nobel prizes for nuclear magnetic resonance: 2003 and Historical perspectives. J. Magn. Reson. Imaging 20, 177–179. doi:10.1002/jmri.20120
Boly, M., Phillips, C., Tshibanda, L., Vanhaudenhuyse, A., Schabus, M., Dang-Vu, T.T., Moonen, G., Hustinx, R., Maquet, P., Laureys, S., 2008. Intrinsic brain activity in altered states of consciousness: how conscious is the default mode of brain function? Ann. N. Y. Acad. Sci. 1129, 119–129. doi:10.1196/annals.1417.015
Boly, M., Seth, A.K., Wilke, M., Ingmundson, P., Baars, B., Laureys, S., Edelman, D.B., Tsuchiya, N., 2013. Consciousness in humans and non-human animals: recent advances and future directions. Front. Psychol. 4, 625. doi:10.3389/fpsyg.2013.00625
Borer-Alafi, N., Gil, M., Sazbon, L., Korn, C., 2002. Loewenstein communication scale for the minimally responsive patient. Brain Inj. 16, 593–609. doi:10.1080/02699050110119484
Born, J.D., 1988. The Glasgow-Liège Scale. Prognostic value and evolution of motor response and brain stem reflexes after severe head injury. Acta Neurochir. (Wien) 91, 1–11.
Braver, T.S., Barch, D.M., Gray, J.R., Molfese, D.L., Snyder, A., 2001. Anterior cingulate cortex and response conflict: effects of frequency, inhibition and errors. Cereb. Cortex N. Y. N 1991 11, 825–836.
Bremmer, F., Schlack, A., Shah, N.J., Zafiris, O., Kubischik, M., Hoffmann, K., Zilles, K., Fink, G.R., 2001. Polymodal motion processing in posterior parietal and premotor cortex: a human fMRI study strongly implies equivalencies between humans and monkeys. Neuron 29, 287–296.
Bruno, M., Bernheim, J.L., Schnakers, C., Laureys, S., 2008. Locked-in: don't judge a book by its cover. J. Neurol. Neurosurg. Psychiatry 79, 2. doi:10.1136/jnnp.2007.125294
Bruno, M.-A., Gosseries, O., Ledoux, D., Hustinx, R., Laureys, S., 2011a. Assessment of consciousness with electrophysiological and neurological imaging techniques. Curr. Opin. Crit. Care 17, 146–151. doi:10.1097/MCC.0b013e328343476d
Bruno, M.-A., Vanhaudenhuyse, A., Thibaut, A., Moonen, G., Laureys, S., 2011b. From unresponsive wakefulness to minimally conscious PLUS and functional locked-in syndromes: recent advances in our understanding of disorders of consciousness. J. Neurol. 258, 1373–1384. doi:10.1007/s00415-011-6114-x

Büchel, C., Holmes, A.P., Rees, G., Friston, K.J., 1998. Characterizing stimulus-response functions using nonlinear regressors in parametric fMRI experiments. NeuroImage 8, 140–148. doi:10.1006/nimg.1998.0351

Bullmore, E., Sporns, O., 2009. Complex brain networks: graph theoretical analysis of structural and functional systems. Nat. Rev. Neurosci. 10, 186–198. doi:10.1038/nrn2575

Butts, C.T., 2008. Social network analysis: A methodological introduction. Asian J. Soc. Psychol. 13.

Buxton, R.B., Wong, E.C., Frank, L.R., 1998. Dynamics of blood flow and oxygenation changes during brain activation: the balloon model. Magn. Reson. Med. 39, 855–864.

Cammaroto, S., Smorto, C., Galletta, D., Bramanti, P., Calabrò, R.S., 2015. Autopsy-like MRI findings: report on Creutzfeldt-Jakob disease in the end-stage. Neurol. Sci. Off. J. Ital. Neurol. Soc. Ital. Soc. Clin. Neurophysiol. 36, 1497–1499. doi:10.1007/s10072-015-2112-6

Candelieri, A., Cortese, M.D., Dolce, G., Riganello, F., Sannita, W.G., 2011. Visual pursuit: within-day variability in the severe disorder of consciousness. J. Neurotrauma 28, 2013–2017. doi:10.1089/neu.2011.1885

Casimiro, C., Martins, J., Parreira, T., Baldeiras, I., Ribeiro, H., Batista, S., Machado, E., Maduro, A., Rebelo, O., Freitas, P., 2012. [Bilateral hyperintensity of the pulvinar and dorsomedial nucleus of the thalamus in sporadic Creutzfeldt-Jakob disease]. Acta Med. Port. 25 Suppl 1, 41–44.

Cavanna, A.E., Trimble, M.R., 2006. The precuneus: a review of its functional anatomy and behavioural correlates. Brain J. Neurol. 129, 564–583. doi:10.1093/brain/awl004

Chatelle, C., Chennu, S., Noirhomme, Q., Cruse, D., Owen, A.M., Laureys, S., 2012. Brain-computer interfacing in disorders of consciousness. Brain Inj. 26, 1510–1522. doi:10.3109/02699052.2012.698362

Childs, N.L., Mercer, W.N., Childs, H.W., 1993. Accuracy of diagnosis of persistent vegetative state. Neurology 43, 1465–1467.

Coleman, M.R., Bekinschtein, T., Monti, M.M., Owen, A.M., Pickard, J.D., 2009. A multimodal approach to the assessment of patients with disorders of consciousness. Prog. Brain Res. 177, 231–248. doi:10.1016/S0079-6123(09)17716-6

Cologan, V., Drouot, X., Parapatics, S., Delorme, A., Gruber, G., Moonen, G., Laureys, S., 2013. Sleep in the unresponsive wakefulness syndrome and minimally conscious state. J. Neurotrauma 30, 339–346. doi:10.1089/neu.2012.2654

Constable, R.T., Spencer, D.D., 2001. Repetition time in echo planar functional MRI. Magn. Reson. Med. 46, 748–755.

Cortes, C., Vapnik, V., 1995. Support-vector networks. Mach. Learn. 20, 273–297. doi:10.1007/BF00994018

Crone, J.S., Soddu, A., Höller, Y., Vanhaudenhuyse, A., Schurz, M., Bergmann, J., Schmid, E., Trinka, E., Laureys, S., Kronbichler, M., 2014. Altered network properties of the fronto-parietal network and the thalamus in impaired consciousness. NeuroImage Clin. 4, 240–248. doi:10.1016/j.nicl.2013.12.005

Davis, L.D., 1991. Handbook Of Genetic Algorithms, 1st edition. ed. Van Nostrand Reinhold, New York.

De Martino, F., Moerel, M., van de Moortele, P.-F., Ugurbil, K., Goebel, R., Yacoub, E., Formisano, E., 2013. Spatial organization of frequency preference and selectivity in the human inferior colliculus. Nat. Commun. 4, 1386. doi:10.1038/ncomms2379

de Villemeur, T.B., 2013. Creutzfeldt-Jakob disease. Handb. Clin. Neurol. 112, 1191–1193. doi:10.1016/B978-0-444-52910-7.00040-4

Desikan, R.S., Ségonne, F., Fischl, B., Quinn, B.T., Dickerson, B.C., Blacker, D., Buckner, R.L., Dale, A.M., Maguire, R.P., Hyman, B.T., Albert, M.S., Killiany, R.J., 2006. An automated labeling system for subdividing the human cerebral cortex on MRI scans into gyral based regions of interest. NeuroImage 31, 968–980. doi:10.1016/j.neuroimage.2006.01.021

Di Perri, C., Stender, J., Laureys, S., Gosseries, O., 2014. Functional neuroanatomy of disorders of consciousness. Epilepsy Behav. EB 30, 28–32. doi:10.1016/j.yebeh.2013.09.014

Donaldson, D.I., Petersen, S.E., Ollinger, J.M., Buckner, R.L., 2001. Dissociating state and item

components of recognition memory using fMRI. NeuroImage 13, 129–142. doi:10.1006/nimg.2000.0664

Draper, N.R., Smith, H., 1998. Applied Regression Analysis, Third edition. ed. Wiley-Interscience, New York Chichester.

Dueck, M.H., Petzke, F., Gerbershagen, H.J., Paul, M., Hesselmann, V., Girnus, R., Krug, B., Sorger, B., Goebel, R., Lehrke, R., Sturm, V., Boerner, U., 2005. Propofol attenuates responses of the auditory cortex to acoustic stimulation in a dose-dependent manner: a FMRI study. Acta Anaesthesiol. Scand. 49, 784–791. doi:10.1111/j.1399-6576.2005.00703.x

Dunitz, J.D., 1996. Linus Carl Pauling. 28 February 1901-19 August 1994. Biogr. Mem. Fellows R. Soc. 42, 317–338. doi:10.2307/770212

Estrada, E., 2011. The Structure of Complex Networks: Theory and Applications. Oxford University Press, Oxford, New York.

Estraneo, A., Moretta, P., Cardinale, V., De Tanti, A., Gatta, G., Giacino, J.T., Trojano, L., 2015. A multicentre study of intentional behavioural responses measured using the Coma Recovery Scale-Revised in patients with minimally conscious state. Clin. Rehabil. 29, 803–808. doi:10.1177/0269215514556002

Evans, A.C., Collins, D.L., Mills, S.R., Brown, E.D., Kelly, R.L., Peters, T.M., 1993. 3D statistical neuroanatomical models from 305 MRI volumes, in: 1993 IEEE Conference Record Nuclear Science Symposium and Medical Imaging Conference. Presented at the 1993 IEEE Conference Record Nuclear Science Symposium and Medical Imaging Conference, pp. 1813–1817 vol.3. doi:10.1109/NSSMIC.1993.373602

Filler, A.G., 2009. The History, Development and Impact of Computed Imaging in Neurological Diagnosis and Neurosurgery: CT, MRI, and DTI. Nat. Preced. doi:10.1038/npre.2009.3267.4

Fischer, D.B., Boes, A.D., Demertzi, A., Evrard, H.C., Laureys, S., Edlow, B.L., Liu, H., Saper, C.B., Pascual-Leone, A., Fox, M.D., Geerling, J.C., 2016. A human brain network derived from coma-causing brainstem lesions. Neurology 87, 2427–2434. doi:10.1212/WNL.0000000000003404

Forner, S.A., Takada, L.T., Bettcher, B.M., Lobach, I.V., Tartaglia, M.C., Torres-Chae, C., Haman, A., Thai, J., Vitali, P., Neuhaus, J., Bostrom, A., Miller, B.L., Rosen, H.J., Geschwind, M.D., 2015. Comparing CSF biomarkers and brain MRI in the diagnosis of sporadic Creutzfeldt-Jakob disease. Neurol. Clin. Pract. 5, 116–125. doi:10.1212/CPJ.0000000000000111

Fortunato, S., 2010. Community detection in graphs. Phys. Rep. 486, 75–174. doi:10.1016/j.physrep.2009.11.002

Fox, M.D., Snyder, A.Z., Vincent, J.L., Corbetta, M., Van Essen, D.C., Raichle, M.E., 2005. The human brain is intrinsically organized into dynamic, anticorrelated functional networks. Proc. Natl. Acad. Sci. U. S. A. 102, 9673–9678. doi:10.1073/pnas.0504136102

Frahm, J., Krüger, G., Merboldt, K.D., Kleinschmidt, A., 1996. Dynamic uncoupling and recoupling of perfusion and oxidative metabolism during focal brain activation in man. Magn. Reson. Med. 35, 143–148.

Frazier, J.A., Chiu, S., Breeze, J.L., Makris, N., Lange, N., Kennedy, D.N., Herbert, M.R., Bent, E.K., Koneru, V.K., Dieterich, M.E., Hodge, S.M., Rauch, S.L., Grant, P.E., Cohen, B.M., Seidman, L.J., Caviness, V.S., Biederman, J., 2005. Structural brain magnetic resonance imaging of limbic and thalamic volumes in pediatric bipolar disorder. Am. J. Psychiatry 162, 1256–1265. doi:10.1176/appi.ajp.162.7.1256

Freeman, L.C., 1978. Centrality in social networks conceptual clarification. Soc. Netw. 1, 215–239. doi:10.1016/0378-8733(78)90021-7

Friston Karl J., 1994. Functional and effective connectivity in neuroimaging: A synthesis. Hum. Brain Mapp. 2, 56–78. doi:10.1002/hbm.460020107

Friston, K.J., Fletcher, P., Josephs, O., Holmes, A., Rugg, M.D., Turner, R., 1998a. Event-related fMRI: characterizing differential responses. NeuroImage 7, 30–40. doi:10.1006/nimg.1997.0306

Friston, K.J., Holmes, A., Poline, J.B., Price, C.J., Frith, C.D., 1996. Detecting activations in PET and

fMRI: levels of inference and power. NeuroImage 4, 223–235. doi:10.1006/nimg.1996.0074
Friston, K.J., Holmes, A.P., Price, C.J., Büchel, C., Worsley, K.J., 1999. Multisubject fMRI studies and conjunction analyses. NeuroImage 10, 385–396. doi:10.1006/nimg.1999.0484
Friston, K.J., Holmes, A.P., Worsley, K.J., Poline, J.-P., Frith, C.D., Frackowiak, R.S.J., 1994a. Statistical parametric maps in functional imaging: A general linear approach. Hum. Brain Mapp. 2, 189–210. doi:10.1002/hbm.460020402
Friston, K.J., Jezzard, P., Turner, R., 1994b. Analysis of functional MRI time-series. Hum. Brain Mapp. 1, 153–171. doi:10.1002/hbm.460010207
Friston, K.J., Josephs, O., Rees, G., Turner, R., 1998b. Nonlinear event-related responses in fMRI. Magn. Reson. Med. 39, 41–52.
Frohlich, H., Chapelle, O., Scholkopf, B., 2003. Feature selection for support vector machines by means of genetic algorithm, in: Proceedings. 15th IEEE International Conference on Tools with Artificial Intelligence. Presented at the Proceedings. 15th IEEE International Conference on Tools with Artificial Intelligence, pp. 142–148. doi:10.1109/TAI.2003.1250182
Frost, M.A., Goebel, R., 2013. Functionally informed cortex based alignment: An integrated approach for whole-cortex macro-anatomical and ROI-based functional alignment. NeuroImage 83, 1002–1010. doi:10.1016/j.neuroimage.2013.07.056
Frost, M.A., Goebel, R., 2012. Measuring structural-functional correspondence: spatial variability of specialised brain regions after macro-anatomical alignment. NeuroImage 59, 1369–1381. doi:10.1016/j.neuroimage.2011.08.035
Fukushima, R., Shiga, Y., Nakamura, M., Fujimori, J., Kitamoto, T., Yoshida, Y., 2004. MRI characteristics of sporadic CJD with valine homozygosity at codon 129 of the prion protein gene and PrPSc type 2 in Japan. J. Neurol. Neurosurg. Psychiatry 75, 485–487.
Furukawa, F., Ishibashi, S., Sanjo, N., Yamashita, H., Mizusawa, H., 2014. Serial magnetic resonance imaging changes in sporadic Creutzfeldt-Jakob disease with valine homozygosity at codon 129 of the prion protein gene. JAMA Neurol. 71, 1186–1187. doi:10.1001/jamaneurol.2014.548
Gallasch, E., Golaszewski, S.M., Fend, M., Siedentopf, C.M., Koppelstaetter, F., Eisner, W., Gerstenbrand, F., Felber, S.R., 2006. Contact force- and amplitude-controllable vibrating probe for somatosensory mapping of plantar afferences with fMRI. J. Magn. Reson. Imaging JMRI 24, 1177–1182. doi:10.1002/jmri.20742
Gasparini, S., Ferlazzo, E., Branca, D., Labate, A., Cianci, V., Latella, M.A., Aguglia, U., 2013. Teaching neuroimages: Pseudohypertrophic cerebral cortex in end-stage Creutzfeldt-Jakob disease. Neurology 80, e21. doi:10.1212/WNL.0b013e31827b92bd
GenLouvain: A generalized Louvain method for community detection implemented in MATLAB, 2018. . GenLouvain.
Genovese, C.R., Lazar, N.A., Nichols, T., 2002. Thresholding of statistical maps in functional neuroimaging using the false discovery rate. NeuroImage 15, 870–878. doi:10.1006/nimg.2001.1037
Gerstenbrand, F., Hamdi, T., Kothbauer, P., Rustam, H., Al Badri, M., 1977. Apallic syndrome in chronic mercury poisoning. Eur. Neurol. 15, 249–256.
Giacino, J.T., 2005. The minimally conscious state: defining the borders of consciousness. Prog. Brain Res. 150, 381–395. doi:10.1016/S0079-6123(05)50027-X
Giacino, J.T., 2004. The vegetative and minimally conscious states: consensus-based criteria for establishing diagnosis and prognosis. NeuroRehabilitation 19, 293–298.
Giacino, J.T., Ashwal, S., Childs, N., Cranford, R., Jennett, B., Katz, D.I., Kelly, J.P., Rosenberg, J.H., Whyte, J., Zafonte, R.D., Zasler, N.D., 2002. The minimally conscious state: definition and diagnostic criteria. Neurology 58, 349–353.
Giacino, J.T., Edlow, B., Chatelle, C., Schnakers, C., 2015. The Minimally Conscious State: Clinical Features, Pathophysiology and Therapeutic Implications.
Giacino, J.T., Fins, J.J., Laureys, S., Schiff, N.D., 2014. Disorders of consciousness after acquired brain injury: the state of the science. Nat. Rev. Neurol. 10, 99–114.

doi:10.1038/nrneurol.2013.279
Giacino, J.T., Hirsch, J., Schiff, N., Laureys, S., 2006. Functional neuroimaging applications for assessment and rehabilitation planning in patients with disorders of consciousness. Arch. Phys. Med. Rehabil. 87, S67-76. doi:10.1016/j.apmr.2006.07.272
Giacino, J.T., Kalmar, K., Whyte, J., 2004. The JFK Coma Recovery Scale-Revised: measurement characteristics and diagnostic utility. Arch. Phys. Med. Rehabil. 85, 2020–2029.
Giacino, J.T., Kezmarsky, M.A., DeLuca, J., Cicerone, K.D., 1991. Monitoring rate of recovery to predict outcome in minimally responsive patients. Arch. Phys. Med. Rehabil. 72, 897–901.
Giacino, J.T., Schnakers, C., Rodriguez-Moreno, D., Kalmar, K., Schiff, N., Hirsch, J., 2009. Behavioral assessment in patients with disorders of consciousness: gold standard or fool's gold? Prog. Brain Res. 177, 33–48. doi:10.1016/S0079-6123(09)17704-X
Gill-Thwaites, H., 2006. Lotteries, loopholes and luck: misdiagnosis in the vegetative state patient. Brain Inj. 20, 1321–1328.
Gill-Thwaites, H., 1997. The Sensory Modality Assessment Rehabilitation Technique--a tool for assessment and treatment of patients with severe brain injury in a vegetative state. Brain Inj. 11, 723–734.
Gill-Thwaites, H., Munday, R., 2004. The Sensory Modality Assessment and Rehabilitation Technique (SMART): a valid and reliable assessment for vegetative state and minimally conscious state patients. Brain Inj. 18, 1255–1269.
Girvan, M., Newman, M.E.J., 2002. Community structure in social and biological networks. Proc. Natl. Acad. Sci. U. S. A. 99, 7821–7826. doi:10.1073/pnas.122653799
Glover, G.H., 1999. Deconvolution of impulse response in event-related BOLD fMRI. NeuroImage 9, 416–429.
Golaszewski, S., Wutzl, B., Unterrainer, A.F., Florea, C., Kronbichler, M., Nardone, R., Rattay, F., Trinka, E., Weis, S., in prep. FMRI findings in the final stage of Creutzfeldt-Jakob-disease.
Golaszewski, S.M., Siedentopf, C.M., Baldauf, E., Koppelstaetter, F., Eisner, W., Unterrainer, J., Guendisch, G.M., Mottaghy, F.M., Felber, S.R., 2002a. Functional magnetic resonance imaging of the human sensorimotor cortex using a novel vibrotactile stimulator. NeuroImage 17, 421–430.
Golaszewski, S.M., Zschiegner, F., Siedentopf, C.M., Unterrainer, J., Sweeney, R.A., Eisner, W., Lechner-Steinleitner, S., Mottaghy, F.M., Felber, S., 2002b. A new pneumatic vibrator for functional magnetic resonance imaging of the human sensorimotor cortex. Neurosci. Lett. 324, 125–128.
Goldberg, D.E., 1989. Genetic Algorithms in Search, Optimization and Machine Learning, 1st ed. Addison-Wesley Longman Publishing Co., Inc., Boston, MA, USA.
Goldfine, A.M., Schiff, N.D., 2011. Consciousness: Its Neurobiology and the Major Classes of Impairment. Neurol. Clin. 29, 723–737. doi:10.1016/j.ncl.2011.08.001
Goldstein, J.M., Seidman, L.J., Makris, N., Ahern, T., O'Brien, L.M., Caviness, V.S., Kennedy, D.N., Faraone, S.V., Tsuang, M.T., 2007. Hypothalamic abnormalities in schizophrenia: sex effects and genetic vulnerability. Biol. Psychiatry 61, 935–945. doi:10.1016/j.biopsych.2006.06.027
Gosseries, O., Pistoia, F., Charland-Verville, V., Carolei, A., Sacco, S., Laureys, S., 2016. The Role of Neuroimaging Techniques in Establishing Diagnosis, Prognosis and Therapy in Disorders of Consciousness. Open Neuroimaging J. 10, 52–68. doi:10.2174/1874440001610010052
Gosseries, O., Zasler, N.D., Laureys, S., 2014. Recent advances in disorders of consciousness: focus on the diagnosis. Brain Inj. 28, 1141–1150. doi:10.3109/02699052.2014.920522
Göttlich, M., Münte, T.F., Heldmann, M., Kasten, M., Hagenah, J., Krämer, U.M., 2013. Altered resting state brain networks in Parkinson's disease. PloS One 8, e77336. doi:10.1371/journal.pone.0077336
Greicius, M.D., Krasnow, B., Reiss, A.L., Menon, V., 2003. Functional connectivity in the resting brain: a network analysis of the default mode hypothesis. Proc. Natl. Acad. Sci. U. S. A. 100, 253–258. doi:10.1073/pnas.0135058100
Greicius, M.D., Srivastava, G., Reiss, A.L., Menon, V., 2004. Default-mode network activity

distinguishes Alzheimer's disease from healthy aging: evidence from functional MRI. Proc. Natl. Acad. Sci. U. S. A. 101, 4637–4642. doi:10.1073/pnas.0308627101
Gurd, J.M., Amunts, K., Weiss, P.H., Zafiris, O., Zilles, K., Marshall, J.C., Fink, G.R., 2002. Posterior parietal cortex is implicated in continuous switching between verbal fluency tasks: an fMRI study with clinical implications. Brain J. Neurol. 125, 1024–1038.
Gusnard, D.A., Raichle, M.E., Raichle, M.E., 2001. Searching for a baseline: functional imaging and the resting human brain. Nat. Rev. Neurosci. 2, 685–694. doi:10.1038/35094500
Guyon, I., Elisseeff, A., 2003. An Introduction to Variable and Feature Selection. J. Mach. Learn. Res. 3, 1157–1182.
Guyon, I., Weston, J., Barnhill, S., Vapnik, V., 2002. Gene Selection for Cancer Classification using Support Vector Machines. Mach. Learn. 46, 389–422. doi:10.1023/A:1012487302797
Haacke, E.M., Brown, R.W., Thompson, M.R., Venkatesan, R., 1999. Magnetic Resonance Imaging: Physical Principles and Sequence Design, 1st edition. ed. Wiley-Liss, New York, NY.
Ham, T., Leff, A., de Boissezon, X., Joffe, A., Sharp, D.J., 2013. Cognitive control and the salience network: an investigation of error processing and effective connectivity. J. Neurosci. Off. J. Soc. Neurosci. 33, 7091–7098. doi:10.1523/JNEUROSCI.4692-12.2013
Havlicek, M., Roebroeck, A., Friston, K., Gardumi, A., Ivanov, D., Uludag, K., 2015. Physiologically informed dynamic causal modeling of fMRI data. NeuroImage 122, 355–372. doi:10.1016/j.neuroimage.2015.07.078
Haxby, J.V., Guntupalli, J.S., Connolly, A.C., Halchenko, Y.O., Conroy, B.R., Gobbini, M.I., Hanke, M., Ramadge, P.J., 2011. A common, high-dimensional model of the representational space in human ventral temporal cortex. Neuron 72, 404–416. doi:10.1016/j.neuron.2011.08.026
Hinrichs, H., Scholz, M., Tempelmann, C., Woldorff, M.G., Dale, A.M., Heinze, H.J., 2000. Deconvolution of event-related fMRI responses in fast-rate experimental designs: tracking amplitude variations. J. Cogn. Neurosci. 12 Suppl 2, 76–89. doi:10.1162/089892900564082
Hirschberg, R., Giacino, J.T., 2011. The Vegetative and Minimally Conscious States: Diagnosis, Prognosis and Treatment. Neurol. Clin. 29, 773–786. doi:10.1016/j.ncl.2011.07.009
Hofstadter, R., 2008. Felix Bloch. Phys. Today 37, 115. doi:10.1063/1.2916128
Holland, J.H., 1975. Adaptation in natural and artificial systems: an introductory analysis with applications to biology, control, and artificial intelligence. University of Michigan Press.
Höller, Y., Bergmann, J., Thomschewski, A., Kronbichler, M., Höller, P., Crone, J.S., Schmid, E.V., Butz, K., Nardone, R., Trinka, E., 2013. Comparison of EEG-features and classification methods for motor imagery in patients with disorders of consciousness. PloS One 8, e80479. doi:10.1371/journal.pone.0080479
Howseman, A.M., Grootoonk, S., Porter, D.A., Ramdeen, J., Holmes, A.P., Turner, R., 1999. The effect of slice order and thickness on fMRI activation data using multislice echo-planar imaging. NeuroImage 9, 363–376. doi:10.1006/nimg.1998.0418
Huang, C.-L., Wang, C.-J., 2006. A GA-based feature selection and parameters optimizationfor support vector machines. Expert Syst. Appl. 31, 231–240. doi:10.1016/j.eswa.2005.09.024
Huang, J., Carr, T.H., Cao, Y., 2002. Comparing cortical activations for silent and overt speech using event-related fMRI. Hum. Brain Mapp. 15, 39–53.
Huang, Z., Zhang, J., Wu, J., Qin, P., Wu, X., Wang, Z., Dai, R., Li, Y., Liang, W., Mao, Y., Yang, Z., Zhang, J., Wolff, A., Northoff, G., 2016. Decoupled temporal variability and signal synchronization of spontaneous brain activity in loss of consciousness: An fMRI study in anesthesia. NeuroImage 124, 693–703. doi:10.1016/j.neuroimage.2015.08.062
Huettel, S.A., Song, A.W., McCarthy, G., 2008. Functional Magnetic Resonance Imaging, Second Edition, 2nd edition. ed. Sinauer Associates, Sunderland, Mass.
Humphries, M.D., Gurney, K., 2008. Network 'Small-World-Ness': A Quantitative Method for Determining Canonical Network Equivalence. PLOS ONE 3, e0002051. doi:10.1371/journal.pone.0002051
Hutzelmann, A., Biederer, J., 1998. MRI follow-up in a case of clinically diagnosed Creutzfeld-Jakob disease. Eur. Radiol. 8, 421–423. doi:10.1007/s003300050404

In, C.B., Choi, Y.S., Park, E.Y., Chang, D.J., Lee, S.K., Choi, H., Moon, H.S., 2011. Anesthetic management in patients suspected of Creutzfeldt-Jakob disease -A case report-. Korean J. Anesthesiol. 61, 262–264. doi:10.4097/kjae.2011.61.3.262

Itahashi, T., Yamada, T., Watanabe, H., Nakamura, M., Jimbo, D., Shioda, S., Toriizuka, K., Kato, N., Hashimoto, R., 2014. Altered network topologies and hub organization in adults with autism: a resting-state fMRI study. PloS One 9, e94115. doi:10.1371/journal.pone.0094115

Jin, J., 1998. Electromagnetic Analysis and Design in Magnetic Resonance Imaging, 1 edition. ed. CRC Press, Boca Raton, Fla.

Jox, R.J., Bernat, J.L., Laureys, S., Racine, E., 2012. Disorders of consciousness: responding to requests for novel diagnostic and therapeutic interventions. Lancet Neurol. 11, 732–738. doi:10.1016/S1474-4422(12)70154-0

Kampfl, A., Schmutzhard, E., Franz, G., Pfausler, B., Haring, H.P., Ulmer, H., Felber, S., Golaszewski, S., Aichner, F., 1998. Prediction of recovery from post-traumatic vegetative state with cerebral magnetic-resonance imaging. Lancet Lond. Engl. 351, 1763–1767. doi:10.1016/S0140-6736(97)10301-4

Karamzadeh, N., Ardeshirpour, Y., Kellman, M., Chowdhry, F., Anderson, A., Chorlian, D., Wegman, E., Gandjbakhche, A., 2015. Relative brain signature: a population-based feature extraction procedure to identify functional biomarkers in the brain of alcoholics. Brain Behav. 5. doi:10.1002/brb3.335

Kiehl, K.A., Liddle, P.F., Hopfinger, J.B., 2000. Error processing and the rostral anterior cingulate: an event-related fMRI study. Psychophysiology 37, 216–223.

Kilner, J.M., Neal, A., Weiskopf, N., Friston, K.J., Frith, C.D., 2009. Evidence of mirror neurons in human inferior frontal gyrus. J. Neurosci. Off. J. Soc. Neurosci. 29, 10153–10159. doi:10.1523/JNEUROSCI.2668-09.2009

Kim, J.H., Choi, B.S., Jung, C., Chang, Y., Kim, S., 2011. Diffusion-weighted imaging and magnetic resonance spectroscopy of sporadic Creutzfeldt-Jakob disease: correlation with clinical course. Neuroradiology 53, 939–945. doi:10.1007/s00234-010-0820-4

Kobayashi, A., Satoh, S., Ironside, J.W., Mohri, S., Kitamoto, T., 2005. Type 1 and type 2 human PrPSc have different aggregation sizes in methionine homozygotes with sporadic, iatrogenic and variant Creutzfeldt–Jakob disease. J. Gen. Virol. 86, 237–240. doi:10.1099/vir.0.80389-0

Kobylarz, E.J., Schiff, N.D., 2005. Neurophysiological correlates of persistent vegetative and minimally conscious states. Neuropsychol. Rehabil. 15, 323–332. doi:10.1080/09602010443000605

Kohavi, R., John, G., 1997. Wrappers for feature subset selection. Artif. Intell. 97, 273–324. doi:10.1016/S0004-3702(97)00043-X

Koutsouleris, N., Meisenzahl, E.M., Davatzikos, C., Bottlender, R., Frodl, T., Scheuerecker, J., Schmitt, G., Zetzsche, T., Decker, P., Reiser, M., Möller, H.-J., Gaser, C., 2009. Use of Neuroanatomical Pattern Classification to Identify Subjects in At-Risk Mental States of Psychosis and Predict Disease Transition. Arch. Gen. Psychiatry 66, 700–712. doi:10.1001/archgenpsychiatry.2009.62

Krmpotich, T.D., Tregellas, J.R., Thompson, L.L., Banich, M.T., Klenk, A.M., Tanabe, J.L., 2013. Resting-state activity in the left executive control network is associated with behavioral approach and is increased in substance dependence. Drug Alcohol Depend. 129, 1–7. doi:10.1016/j.drugalcdep.2013.01.021

Krope, K., Pantazis, G., Nägele, T., Claussen, C.D., Horger, M., 2011. [Sporadic creutzfeld-jacob disease]. ROFO. Fortschr. Geb. Rontgenstr. Nuklearmed. 183, 593–596. doi:10.1055/s-0031-1274713

Kruggel, F., von Cramon, D.Y., 1999. Temporal properties of the hemodynamic response in functional MRI. Hum. Brain Mapp. 8, 259–271.

Kübler, A., Furdea, A., Halder, S., Hammer, E.M., Nijboer, F., Kotchoubey, B., 2009. A brain-computer interface controlled auditory event-related potential (p300) spelling system for locked-in patients. Ann. N. Y. Acad. Sci. 1157, 90–100. doi:10.1111/j.1749-

6632.2008.04122.x
Kulkarni, K.M., 2015. Progressive MRI findings in Creutzfeldt-Jakob disease. J. Neuro-Ophthalmol. Off. J. North Am. Neuro-Ophthalmol. Soc. 35, 96–98. doi:10.1097/WNO.0000000000000185
Kumaran, S.P., Gupta, K., Pushpa, B., Viswamitra, S., Joshy, E., 2012. Diffusion-weighted imaging: As the first diagnostic clue to Creutzfeldt Jacob disease. J. Neurosci. Rural Pract. 3, 408–410. doi:10.4103/0976-3147.102645
Kutner, M., Nachtsheim, C., Li, W., 2004. Applied Linear Statistical Models, 5th edition. ed. McGraw-Hill/Irwin, Boston.
Kwong, K.K., Belliveau, J.W., Chesler, D.A., Goldberg, I.E., Weisskoff, R.M., Poncelet, B.P., Kennedy, D.N., Hoppel, B.E., Cohen, M.S., Turner, R., 1992. Dynamic magnetic resonance imaging of human brain activity during primary sensory stimulation. Proc. Natl. Acad. Sci. U. S. A. 89, 5675–5679.
Ladogana, A., Puopolo, M., Croes, E.A., Budka, H., Jarius, C., Collins, S., Klug, G.M., Sutcliffe, T., Giulivi, A., Alperovitch, A., Delasnerie-Laupretre, N., Brandel, J.-P., Poser, S., Kretzschmar, H., Rietveld, I., Mitrova, E., Cuesta, J. de P., Martinez-Martin, P., Glatzel, M., Aguzzi, A., Knight, R., Ward, H., Pocchiari, M., van Duijn, C.M., Will, R.G., Zerr, I., 2005. Mortality from Creutzfeldt-Jakob disease and related disorders in Europe, Australia, and Canada. Neurology 64, 1586–1591. doi:10.1212/01.WNL.0000160117.56690.B2
Lametti, D.R., Mattar, A.A.G., 2006. Mirror neurons and the lateralization of human language. J. Neurosci. Off. J. Soc. Neurosci. 26, 6666–6667.
Lancichinetti, A., Fortunato, S., 2012. Consensus clustering in complex networks. Sci. Rep. 2, 336. doi:10.1038/srep00336
Latora, V., Marchiori, M., 2001. Efficient Behavior of Small-World Networks. Phys. Rev. Lett. 87, 198701. doi:10.1103/PhysRevLett.87.198701
Laureys, S., 2006. The Boundaries of Consciousness: Neurobiology and Neuropathology. Elsevier.
Laureys, S., Boly, M., Maquet, P., 2006. Tracking the recovery of consciousness from coma. J. Clin. Invest. 116, 1823–1825. doi:10.1172/JCI29172
Laureys, S., Celesia, G.G., Cohadon, F., Lavrijsen, J., León-Carrión, J., Sannita, W.G., Sazbon, L., Schmutzhard, E., von Wild, K.R., Zeman, A., Dolce, G., European Task Force on Disorders of Consciousness, 2010. Unresponsive wakefulness syndrome: a new name for the vegetative state or apallic syndrome. BMC Med. 8, 68. doi:10.1186/1741-7015-8-68
Laureys, S., Faymonville, M.E., Luxen, A., Lamy, M., Franck, G., Maquet, P., 2000. Restoration of thalamocortical connectivity after recovery from persistent vegetative state. Lancet Lond. Engl. 355, 1790–1791.
Laureys, S., Owen, A.M., Schiff, N.D., 2004. Brain function in coma, vegetative state, and related disorders. Lancet Neurol. 3, 537–546. doi:10.1016/S1474-4422(04)00852-X
Laureys, S., Pellas, F., Van Eeckhout, P., Ghorbel, S., Schnakers, C., Perrin, F., Berré, J., Faymonville, M.-E., Pantke, K.-H., Damas, F., Lamy, M., Moonen, G., Goldman, S., 2005. The locked-in syndrome : what is it like to be conscious but paralyzed and voiceless? Prog. Brain Res. 150, 495–511. doi:10.1016/S0079-6123(05)50034-7
Laureys, S., Tononi, G. (Eds.), 2008. The Neurology of Consciousness: Cognitive Neuroscience and Neuropathology, 1 edition. ed. Academic Press, Amsterdam.
Legostaeva, L., Mochalova, E., Poydasheva, A., Kremneva, E., Sergeev, D., Ryabinkina, J., Domashenko, M., Suponeva, N., Piradov, M., 2017. Misdiagnosis in doc patients: Russian experience. J. Neurol. Sci. 381, 756. doi:10.1016/j.jns.2017.08.2134
Lemm, S., Blankertz, B., Dickhaus, T., Müller, K.-R., 2011. Introduction to machine learning for brain imaging. NeuroImage, Multivariate Decoding and Brain Reading 56, 387–399. doi:10.1016/j.neuroimage.2010.11.004
León-Carrión, J., van Eeckhout, P., Domínguez-Morales, M.D.R., Pérez-Santamaría, F.J., 2002. The locked-in syndrome: a syndrome looking for a therapy. Brain Inj. 16, 571–582. doi:10.1080/02699050110119781
Lodi, R., Parchi, P., Tonon, C., Manners, D., Capellari, S., Strammiello, R., Rinaldi, R., Testa, C.,

Malucelli, E., Mostacci, B., Rizzo, G., Pierangeli, G., Cortelli, P., Montagna, P., Barbiroli, B., 2009. Magnetic resonance diagnostic markers in clinically sporadic prion disease: a combined brain magnetic resonance imaging and spectroscopy study. Brain J. Neurol. 132, 2669–2679. doi:10.1093/brain/awp210

Logothetis, N.K., Pauls, J., Augath, M., Trinath, T., Oeltermann, A., 2001. Neurophysiological investigation of the basis of the fMRI signal. Nature 412, 150. doi:10.1038/35084005

Lu, H., Golay, X., Pekar, J.J., Van Zijl, P.C.M., 2004. Sustained poststimulus elevation in cerebral oxygen utilization after vascular recovery. J. Cereb. Blood Flow Metab. Off. J. Int. Soc. Cereb. Blood Flow Metab. 24, 764–770. doi:10.1097/01.WCB.0000124322.60992.5C

Luauté, J., Maucort-Boulch, D., Tell, L., Quelard, F., Sarraf, T., Iwaz, J., Boisson, D., Fischer, C., 2010. Long-term outcomes of chronic minimally conscious and vegetative states. Neurology 75, 246–252. doi:10.1212/WNL.0b013e3181e8e8df

Lulé, D., Noirhomme, Q., Kleih, S.C., Chatelle, C., Halder, S., Demertzi, A., Bruno, M.-A., Gosseries, O., Vanhaudenhuyse, A., Schnakers, C., Thonnard, M., Soddu, A., Kübler, A., Laureys, S., 2013. Probing command following in patients with disorders of consciousness using a brain-computer interface. Clin. Neurophysiol. Off. J. Int. Fed. Clin. Neurophysiol. 124, 101–106. doi:10.1016/j.clinph.2012.04.030

Maddock, R.J., Garrett, A.S., Buonocore, M.H., 2003. Posterior cingulate cortex activation by emotional words: fMRI evidence from a valence decision task. Hum. Brain Mapp. 18, 30–41. doi:10.1002/hbm.10075

Maddock, R.J., Garrett, A.S., Buonocore, M.H., 2001. Remembering familiar people: the posterior cingulate cortex and autobiographical memory retrieval. Neuroscience 104, 667–676.

Majerus, S., Gill-Thwaites, H., Andrews, K., Laureys, S., 2005. Behavioral evaluation of consciousness in severe brain damage. Prog. Brain Res. 150, 397–413. doi:10.1016/S0079-6123(05)50028-1

Makris, N., Goldstein, J.M., Kennedy, D., Hodge, S.M., Caviness, V.S., Faraone, S.V., Tsuang, M.T., Seidman, L.J., 2006. Decreased volume of left and total anterior insular lobule in schizophrenia. Schizophr. Res. 83, 155–171. doi:10.1016/j.schres.2005.11.020

Mandeville, J.B., Marota, J.J., Ayata, C., Zaharchuk, G., Moskowitz, M.A., Rosen, B.R., Weisskoff, R.M., 1999. Evidence of a cerebrovascular postarteriole windkessel with delayed compliance. J. Cereb. Blood Flow Metab. Off. J. Int. Soc. Cereb. Blood Flow Metab. 19, 679–689. doi:10.1097/00004647-199906000-00012

Mandeville, J.B., Marota, J.J., Kosofsky, B.E., Keltner, J.R., Weissleder, R., Rosen, B.R., Weisskoff, R.M., 1998. Dynamic functional imaging of relative cerebral blood volume during rat forepaw stimulation. Magn. Reson. Med. 39, 615–624.

Mansour, A., Baria, A.T., Tetreault, P., Vachon-Presseau, E., Chang, P.-C., Huang, L., Apkarian, A.V., Baliki, M.N., 2016. Global disruption of degree rank order: a hallmark of chronic pain. Sci. Rep. 6, 34853. doi:10.1038/srep34853

Marcar, V.L., Schwarz, U., Martin, E., Loenneker, T., 2006. How depth of anesthesia influences the blood oxygenation level-dependent signal from the visual cortex of children. AJNR Am. J. Neuroradiol. 27, 799–805.

Martuzzi, R., Ramani, R., Qiu, M., Rajeevan, N., Constable, R.T., 2010. Functional connectivity and alterations in baseline brain state in humans. NeuroImage 49, 823–834. doi:10.1016/j.neuroimage.2009.07.028

McKeown, M.J., Makeig, S., Brown, G.G., Jung, T.P., Kindermann, S.S., Bell, A.J., Sejnowski, T.J., 1998. Analysis of fMRI data by blind separation into independent spatial components. Hum. Brain Mapp. 6, 160–188.

Medaglia, J.D., 2017. Functional Neuroimaging in Traumatic Brain Injury: From Nodes to Networks. Front. Neurol. 8. doi:10.3389/fneur.2017.00407

Meila, M., 2007. Comparing clusterings—an information based distance. J. Multivar. Anal. 98, 873–895. doi:10.1016/j.jmva.2006.11.013

Menon, V., Uddin, L.Q., 2010. Saliency, switching, attention and control: a network model of insula

function. Brain Struct. Funct. 214, 655–667. doi:10.1007/s00429-010-0262-0
Michalewicz, Z., 1994. Genetic Algorithms + Data Structures = Evolution Programs (2Nd, Extended Ed.). Springer-Verlag, Berlin, Heidelberg.
Monti, M.M., Vanhaudenhuyse, A., Coleman, M.R., Boly, M., Pickard, J.D., Tshibanda, L., Owen, A.M., Laureys, S., 2010. Willful modulation of brain activity in disorders of consciousness. N. Engl. J. Med. 362, 579–589. doi:10.1056/NEJMoa0905370
Morris, P., 2017. Sir Peter Mansfield obituary [WWW Document]. the Guardian. URL http://www.theguardian.com/science/2017/feb/20/sir-peter-mansfield-obituary (accessed 3.30.18).
Mucha, P.J., Richardson, T., Macon, K., Porter, M.A., Onnela, J.-P., 2010. Community structure in time-dependent, multiscale, and multiplex networks. Science 328, 876–878. doi:10.1126/science.1184819
Naci, L., Monti, M.M., Cruse, D., Kübler, A., Sorger, B., Goebel, R., Kotchoubey, B., Owen, A.M., 2012. Brain-computer interfaces for communication with nonresponsive patients. Ann. Neurol. 72, 312–323. doi:10.1002/ana.23656
Newey, C.R., Sarwal, A., Wisco, D., Alam, S., Lederman, R.J., 2013. Variability in diagnosing Creutzfeldt-Jakob disease using standard and proposed diagnostic criteria. J. Neuroimaging Off. J. Am. Soc. Neuroimaging 23, 58–63. doi:10.1111/j.1552-6569.2012.00763.x
Newman, M.E.J., 2006. Modularity and community structure in networks. Proc. Natl. Acad. Sci. 103, 8577–8582. doi:10.1073/pnas.0601602103
Newman, M.E.J., 2002. Assortative mixing in networks. Phys. Rev. Lett. 89. doi:10.1103/PhysRevLett.89.208701
Noé, E., Olaya, J., Navarro, M.D., Noguera, P., Colomer, C., García-Panach, J., Rivero, S., Moliner, B., Ferri, J., 2012. Behavioral recovery in disorders of consciousness: a prospective study with the Spanish version of the Coma Recovery Scale-Revised. Arch. Phys. Med. Rehabil. 93, 428–433.e12. doi:10.1016/j.apmr.2011.08.048
Ogawa, S., Lee, T.M., Kay, A.R., Tank, D.W., 1990. Brain magnetic resonance imaging with contrast dependent on blood oxygenation. Proc. Natl. Acad. Sci. U. S. A. 87, 9868–9872.
Ogawa, S., Tank, D.W., Menon, R., Ellermann, J.M., Kim, S.G., Merkle, H., Ugurbil, K., 1992. Intrinsic signal changes accompanying sensory stimulation: functional brain mapping with magnetic resonance imaging. Proc. Natl. Acad. Sci. U. S. A. 89, 5951–5955.
Olariu, S., Zomaya, A.Y., 2005. Handbook of Bioinspired Algorithms and Applications. CRC Press.
Ostrum, A.E., 1994. The ‘locked-in’ syndrome – comments from a survivor. Brain Inj. 8, 95–98. doi:10.3109/02699059409150962
Otten, L.J., Henson, R.N.A., Rugg, M.D., 2002. State-related and item-related neural correlates of successful memory encoding. Nat. Neurosci. 5, 1339–1344. doi:10.1038/nn967
Owen, A.M., 2013. Detecting consciousness: a unique role for neuroimaging. Annu. Rev. Psychol. 64, 109–133. doi:10.1146/annurev-psych-113011-143729
Owen, A.M., Coleman, M.R., Boly, M., Davis, M.H., Laureys, S., Pickard, J.D., 2006. Detecting awareness in the vegetative state. Science 313, 1402. doi:10.1126/science.1130197
Pape, T.L.-B., Heinemann, A.W., Kelly, J.P., Hurder, A.G., Lundgren, S., 2005. A measure of neurobehavioral functioning after coma. Part I: Theory, reliability, and validity of Disorders of Consciousness Scale. J. Rehabil. Res. Dev. 42, 1–17.
Paterakis, K., Karantanas, A.H., Komnos, A., Volikas, Z., 2000. Outcome of patients with diffuse axonal injury: the significance and prognostic value of MRI in the acute phase. J. Trauma 49, 1071–1075.
Pedregosa, F., Varoquaux, G., Gramfort, A., Michel, V., Thirion, B., Grisel, O., Blondel, M., Prettenhofer, P., Weiss, R., Dubourg, V., Vanderplas, J., Passos, A., Cournapeau, D., Brucher, M., Perrot, M., Duchesnay, É., 2011. Scikit-learn: Machine Learning in Python. J. Mach. Learn. Res. 12, 2825−2830.
Peierls, R.E., 1960. Wolfgang Ernst Pauli, 1900-1958. Biogr. Mem. Fellows R. Soc. 5, 174–192. doi:10.1098/rsbm.1960.0014

Pereira, F., Mitchell, T., Botvinick, M., 2009. Machine learning classifiers and fMRI: a tutorial overview. NeuroImage 45, S199–S209. doi:10.1016/j.neuroimage.2008.11.007

Plewes, D.B., Kucharczyk, W., 2012. Physics of MRI: a primer. J. Magn. Reson. Imaging JMRI 35, 1038–1054. doi:10.1002/jmri.23642

Plum, F., Posner, J.B., 1972. The diagnosis of stupor and coma. Contemp. Neurol. Ser. 10, 1–286.

Porter, M.A., Onnela, J.-P., Mucha, P.J., 2009. Communities in Networks. ArXiv09023788 Cond-Mat Physicsnlin Physicsphysics Stat.

Posner, J.B., Saper, C.B., Schiff, N., Plum, F., 2007. Plum and Posner's Diagnosis of Stupor and Coma, Fourth Edition. ed, Contemporary Neurology Series. Oxford University Press, Oxford, New York.

Powers, D., 2011. Evaluation: From precision, recall and f-measure to roc., informedness, markedness & correlation. J. Mach. Learn. Technol. 2, 37–63.

Pugin, D., Hofmeister, J., Gasche, Y., Van De Ville, D., Vulliemoz, S., Haller, S., 2018. T114. Predicting coma outcome using resting-state fMRI and machine learning. Clin. Neurophysiol. 129, e46. doi:10.1016/j.clinph.2018.04.115

Rader, M.A., Ellis, D.W., 1994. The Sensory Stimulation Assessment Measure (SSAM): a tool for early evaluation of severely brain-injured patients. Brain Inj. 8, 309–321.

Radicchi, F., Castellano, C., Cecconi, F., Loreto, V., Parisi, D., 2004. Defining and identifying communities in networks. Proc. Natl. Acad. Sci. U. S. A. 101, 2658–2663. doi:10.1073/pnas.0400054101

Raichle, M.E., 2006. Neuroscience. The brain's dark energy. Science 314, 1249–1250. doi:10.1126/science. 1134405

Raichle, M.E., Mintun, M.A., 2006. Brain work and brain imaging. Annu. Rev. Neurosci. 29, 449–476. doi:10.1146/annurev.neuro.29.051605.112819

Rappaport, M., Dougherty, A.M., Kelting, D.L., 1992. Evaluation of coma and vegetative states. Arch. Phys. Med. Rehabil. 73, 628–634.

Rath, J., Wurnig, M., Fischmeister, F., Klinger, N., Höllinger, I., Geißler, A., Aichhorn, M., Foki, T., Kronbichler, M., Nickel, J., Siedentopf, C., Staffen, W., Verius, M., Golaszewski, S., Koppelstaetter, F., Auff, E., Felber, S., Seitz, R.J., Beisteiner, R., 2016. Between- and within-site variability of fMRI localizations. Hum. Brain Mapp. 37, 2151–2160. doi:10.1002/hbm.23162

Reichardt, J., Bornholdt, S., 2006. Statistical mechanics of community detection. Phys. Rev. E 74, 016110. doi:10.1103/PhysRevE.74.016110

Richiardi, J., Achard, S., Bunke, H., Ville, D.V.D., 2013. Machine Learning with Brain Graphs: Predictive Modeling Approaches for Functional Imaging in Systems Neuroscience. IEEE Signal Process. Mag. 30, 58–70. doi:10.1109/MSP.2012.2233865

Rolinski, M., Griffanti, L., Szewczyk-Krolikowski, K., Menke, R.A.L., Wilcock, G.K., Filippini, N., Zamboni, G., Hu, M.T.M., Mackay, C.E., 2015. Aberrant functional connectivity within the basal ganglia of patients with Parkinson's disease. NeuroImage Clin. 8, 126–132. doi:10.1016/j.nicl.2015.04.003

Ronhovde, P., Nussinov, Z., 2009. Multiresolution community detection for megascale networks by information-based replica correlations. Phys. Rev. E 80, 016109. doi:10.1103/PhysRevE.80.016109

Rubinov, M., Sporns, O., 2011. Weight-conserving characterization of complex functional brain networks. NeuroImage 56, 2068–2079. doi:10.1016/j.neuroimage.2011.03.069

Rubinov, M., Sporns, O., 2010. Complex network measures of brain connectivity: Uses and interpretations. NeuroImage, Computational Models of the Brain 52, 1059–1069. doi:10.1016/j.neuroimage.2009.10.003

Sachdeva, J., Kumar, V., Gupta, I., Khandelwal, N., Ahuja, C.K., 2013. Segmentation, feature extraction, and multiclass brain tumor classification. J. Digit. Imaging 26, 1141–1150. doi:10.1007/s10278-013-9600-0

Salcedo-Sanz, S., Prado-Cumplido, M., Pérez-Cruz, F., Bousoño-Calzón, C., 2002. Feature Selection

via Genetic Optimization, in: Artificial Neural Networks — ICANN 2002, Lecture Notes in Computer Science. Presented at the International Conference on Artificial Neural Networks, Springer, Berlin, Heidelberg, pp. 547–552. doi:10.1007/3-540-46084-5_89

Schacter, D.L., Buckner, R.L., Koutstaal, W., Dale, A.M., Rosen, B.R., 1997. Late onset of anterior prefrontal activity during true and false recognition: an event-related fMRI study. NeuroImage 6, 259–269. doi:10.1006/nimg.1997.0305

Schiff, N.D., Rodriguez-Moreno, D., Kamal, A., Kim, K.H.S., Giacino, J.T., Plum, F., Hirsch, J., 2005. fMRI reveals large-scale network activation in minimally conscious patients. Neurology 64, 514–523. doi:10.1212/01.WNL.0000150883.10285.44

Schmidt, S.A., Akrofi, K., Carpenter-Thompson, J.R., Husain, F.T., 2013. Default mode, dorsal attention and auditory resting state networks exhibit differential functional connectivity in tinnitus and hearing loss. PloS One 8, e76488. doi:10.1371/journal.pone.0076488

Schnakers, C., Bessou, H., Rubi-Fessen, I., Hartmann, A., Fink, G.R., Meister, I., Giacino, J.T., Laureys, S., Majerus, S., 2015. Impact of aphasia on consciousness assessment: a cross-sectional study. Neurorehabil. Neural Repair 29, 41–47. doi:10.1177/1545968314528067

Schnakers, C., Giacino, J., Kalmar, K., Piret, S., Lopez, E., Boly, M., Malone, R., Laureys, S., 2006. Does the FOUR score correctly diagnose the vegetative and minimally conscious states? Ann. Neurol. 60, 744–745; author reply 745. doi:10.1002/ana.20919

Schnakers, C., Vanhaudenhuyse, A., Giacino, J., Ventura, M., Boly, M., Majerus, S., Moonen, G., Laureys, S., 2009. Diagnostic accuracy of the vegetative and minimally conscious state: clinical consensus versus standardized neurobehavioral assessment. BMC Neurol. 9, 35. doi:10.1186/1471-2377-9-35

Scholkopf, B., Smola, A.J., 2001. Learning with Kernels: Support Vector Machines, Regularization, Optimization, and Beyond. MIT Press, Cambridge, MA, USA.

Schröter, A., Zerr, I., Henkel, K., Tschampa, H.J., Finkenstaedt, M., Poser, S., 2000. Magnetic resonance imaging in the clinical diagnosis of Creutzfeldt-Jakob disease. Arch. Neurol. 57, 1751–1757.

Seel, R.T., Sherer, M., Whyte, J., Katz, D.I., Giacino, J.T., Rosenbaum, A.M., Hammond, F.M., Kalmar, K., Pape, T.L.-B., Zafonte, R., Biester, R.C., Kaelin, D., Kean, J., Zasler, N., 2010. Assessment Scales for Disorders of Consciousness: Evidence-Based Recommendations for Clinical Practice and Research. Arch. Phys. Med. Rehabil. 91, 1795–1813. doi:10.1016/j.apmr.2010.07.218

Seeley, W.W., Menon, V., Schatzberg, A.F., Keller, J., Glover, G.H., Kenna, H., Reiss, A.L., Greicius, M.D., 2007. Dissociable intrinsic connectivity networks for salience processing and executive control. J. Neurosci. Off. J. Soc. Neurosci. 27, 2349–2356. doi:10.1523/JNEUROSCI.5587-06.2007

Segovia, F., Górriz, J.M., Ramírez, J., Phillips, C., The Alzheimer's Disease Neuroimaging Initiative, 2016. Combining Feature Extraction Methods to Assist the Diagnosis of Alzheimer's Disease. Curr. Alzheimer Res. 13, 831–837.

Seidl, M., Golaszewski, S.M., Kunz, A.B., Nardone, R., Bauer, G., Trinka, E., Gerstenbrand, F., 2013. The locked-in plus syndrome. J. Neurol. Sci. 333, e263–e264. doi:10.1016/j.jns.2013.07.1010

Shampo, M.A., Kyle, R.A., Steensma, D.P., 2012. Isidor Rabi—1944 Nobel Laureate in Physics. Mayo Clin. Proc. 87, e11. doi:10.1016/j.mayocp.2011.11.012

Sherman, L.E., Rudie, J.D., Pfeifer, J.H., Masten, C.L., McNealy, K., Dapretto, M., 2014. Development of the default mode and central executive networks across early adolescence: a longitudinal study. Dev. Cogn. Neurosci. 10, 148–159. doi:10.1016/j.dcn.2014.08.002

Shiel, A., Horn, S.A., Wilson, B.A., Watson, M.J., Campbell, M.J., McLellan, D.L., 2000. The Wessex Head Injury Matrix (WHIM) main scale: a preliminary report on a scale to assess and monitor patient recovery after severe head injury. Clin. Rehabil. 14, 408–416.

Shulman, G.L., Corbetta, M., Fiez, J.A., Buckner, R.L., Miezin, F.M., Raichle, M.E., Petersen, S.E., 1997. Searching for activations that generalize over tasks. Hum. Brain Mapp. 5, 317–322. doi:10.1002/(SICI)1097-0193(1997)5:4<317::AID-HBM19>3.0.CO;2-A

Sikorska, B., Knight, R., Ironside, J.W., Liberski, P.P., 2012. Creutzfeldt-Jakob disease. Adv. Exp. Med. Biol. 724, 76–90. doi:10.1007/978-1-4614-0653-2_6

Skipper, J.I., Goldin-Meadow, S., Nusbaum, H.C., Small, S.L., 2007. Speech-associated gestures, Broca's area, and the human mirror system. Brain Lang. 101, 260–277. doi:10.1016/j.bandl.2007.02.008

Slichter, C.P., 1996. Principles of Magnetic Resonance, 3rd enlarged and updated ed. 1990. Corr. 3rd printing 1996 edition. ed. Springer, Berlin.

Smith, S.M., Jenkinson, M., Woolrich, M.W., Beckmann, C.F., Behrens, T.E.J., Johansen-Berg, H., Bannister, P.R., De Luca, M., Drobnjak, I., Flitney, D.E., Niazy, R.K., Saunders, J., Vickers, J., Zhang, Y., De Stefano, N., Brady, J.M., Matthews, P.M., 2004. Advances in functional and structural MR image analysis and implementation as FSL. NeuroImage, Mathematics in Brain Imaging 23, S208–S219. doi:10.1016/j.neuroimage.2004.07.051

Smitha, K., Akhil Raja, K., Arun, K., Rajesh, P., Thomas, B., Kapilamoorthy, T., Kesavadas, C., 2017. Resting state fMRI: A review on methods in resting state connectivity analysis and resting state networks. Neuroradiol. J. 30, 305–317. doi:10.1177/1971400917697342

Sorger, B., Dahmen, B., Reithler, J., Gosseries, O., Maudoux, A., Laureys, S., Goebel, R., 2009. Another kind of "BOLD Response": answering multiple-choice questions via online decoded single-trial brain signals. Prog. Brain Res. 177, 275–292. doi:10.1016/S0079-6123(09)17719-1

Sporns, O., 2010. Networks of the Brain, 1 edition. ed. The MIT Press, Cambridge, Massachusetts London, England.

Staffen, W., Kronbichler, M., Aichhorn, M., Mair, A., Ladurner, G., 2006. Selective brain activity in response to one's own name in the persistent vegetative state. J. Neurol. Neurosurg. Psychiatry 77, 1383–1384. doi:10.1136/jnnp.2006.095166

Stålhammar, D., Starmark, J.E., Holmgren, E., Eriksson, N., Nordström, C.H., Fedders, O., Rosander, B., 1988. Assessment of responsiveness in acute cerebral disorders. A multicentre study on the reaction level scale (RLS 85). Acta Neurochir. (Wien) 90, 73–80.

Stanczak, D.E., White, J.G., Gouview, W.D., Moehle, K.A., Daniel, M., Novack, T., Long, C.J., 1984. Assessment of level of consciousness following severe neurological insult. A comparison of the psychometric qualities of the Glasgow Coma Scale and the Comprehensive Level of Consciousness Scale. J. Neurosurg. 60, 955–960. doi:10.3171/jns.1984.60.5.0955

Strother, S.C., 2006. Evaluating fMRI preprocessing pipelines. IEEE Eng. Med. Biol. Mag. 25, 27–41. doi:10.1109/MEMB.2006.1607667

Strother, S.C., Anderson, J.R., Xu, X.L., Liow, J.S., Bonar, D.C., Rottenberg, D.A., 1994. Quantitative comparisons of image registration techniques based on high-resolution MRI of the brain. J. Comput. Assist. Tomogr. 18, 954–962.

Sun, Y., Danila, B., Josić, K., Bassler, K.E., 2009. Improved community structure detection using a modified fine-tuning strategy. EPL Europhys. Lett. 86, 28004. doi:10.1209/0295-5075/86/28004

Szewczyk-Krolikowski, K., Menke, R.A.L., Rolinski, M., Duff, E., Salimi-Khorshidi, G., Filippini, N., Zamboni, G., Hu, M.T.M., Mackay, C.E., 2014. Functional connectivity in the basal ganglia network differentiates PD patients from controls. Neurology 83, 208–214. doi:10.1212/WNL.0000000000000592

Talairach, J., Tournoux, P., 1988. Co-planar stereotaxic atlas of the human brain : 3-dimensional proportional system : an approach to cerebral imaging. Stuttgart ; New York : G. Thieme ; New York : Thieme Medical Publishers.

Teasdale, G., Jennett, B., 1976. Assessment and prognosis of coma after head injury. Acta Neurochir. (Wien) 34, 45–55.

Teasdale, G., Jennett, B., 1974. Assessment of coma and impaired consciousness. A practical scale. Lancet Lond. Engl. 2, 81–84.

Times, S.T. the N.Y., 1971. Charles DuBois Coryell Is Dead; Chemist Worked on Atom Bomb. N. Y. Times.

Tresch, D.D., Sims, F.H., Duthie, E.H., Goldstein, M.D., Lane, P.S., 1991. Clinical characteristics of patients in the persistent vegetative state. Arch. Intern. Med. 151, 930–932.

Tzourio-Mazoyer, N., Landeau, B., Papathanassiou, D., Crivello, F., Etard, O., Delcroix, N., Mazoyer, B., Joliot, M., 2002. Automated anatomical labeling of activations in SPM using a macroscopic anatomical parcellation of the MNI MRI single-subject brain. NeuroImage 15, 273–289. doi:10.1006/nimg.2001.0978

Uddin, L.Q., 2015. Salience processing and insular cortical function and dysfunction. Nat. Rev. Neurosci. 16, 55–61. doi:10.1038/nrn3857

Uludağ, K., Dubowitz, D.J., Yoder, E.J., Restom, K., Liu, T.T., Buxton, R.B., 2004. Coupling of cerebral blood flow and oxygen consumption during physiological activation and deactivation measured with fMRI. NeuroImage 23, 148–155. doi:10.1016/j.neuroimage.2004.05.013

Uludag, K., Ugurbil, K., Berliner, L., 2015. fMRI: From Nuclear Spins to Brain Functions, 1st ed. 2015版. ed. Springer, New York, NY.

Urakami, Y., 2012. Relationship between, sleep spindles and clinical recovery in patients with traumatic brain injury: a simultaneous EEG and MEG study. Clin. EEG Neurosci. 43, 39–47. doi:10.1177/1550059411428718

Urbach, H., Paus, S., Tschampa, H.J., Keller, E., Schild, H.H., 2001. [Creutzfeldt-Jakob disease: value of MRI]. ROFO. Fortschr. Geb. Rontgenstr. Nuklearmed. 173, 509–514. doi:10.1055/s-2001-14990

Vanhaudenhuyse, A., Noirhomme, Q., Tshibanda, L.J.-F., Bruno, M.-A., Boveroux, P., Schnakers, C., Soddu, A., Perlbarg, V., Ledoux, D., Brichant, J.-F., Moonen, G., Maquet, P., Greicius, M.D., Laureys, S., Boly, M., 2010. Default network connectivity reflects the level of consciousness in non-communicative brain-damaged patients. Brain J. Neurol. 133, 161–171. doi:10.1093/brain/awp313

Venkatesan, A., Frucht, S., 2006. Movement disorders after resuscitation from cardiac arrest. Neurol. Clin. 24, 123–132. doi:10.1016/j.ncl.2005.11.001

Wasserman, S., Faust, K., 1994. Social Network Analysis: Methods and Applications. Cambridge University Press.

Watts, D.J., Strogatz, S.H., 1998. Collective dynamics of ‘small-world’ networks. Nature 393, 440. doi:10.1038/30918

Werner, C.J., Dogan, I., Saß, C., Mirzazade, S., Schiefer, J., Shah, N.J., Schulz, J.B., Reetz, K., 2014. Altered resting-state connectivity in Huntington’s disease. Hum. Brain Mapp. 35, 2582–2593. doi:10.1002/hbm.22351

West, J., Fitzpatrick, J.M., Wang, M.Y., Dawant, B.M., Maurer, C.R., Kessler, R.M., Maciunas, R.J., Barillot, C., Lemoine, D., Collignon, A., Maes, F., Suetens, P., Vandermeulen, D., van den Elsen, P.A., Napel, S., Sumanaweera, T.S., Harkness, B., Hemler, P.F., Hill, D.L., Hawkes, D.J., Studholme, C., Maintz, J.B., Viergever, M.A., Malandain, G., Woods, R.P., 1997. Comparison and evaluation of retrospective intermodality brain image registration techniques. J. Comput. Assist. Tomogr. 21, 554–566.

Weston, J., Mukherjee, S., Chapelle, O., Pontil, M., Poggio, T., Vapnik, V., 2000. Feature Selection for SVMs, in: Proceedings of the 13th International Conference on Neural Information Processing Systems, NIPS’00. MIT Press, Cambridge, MA, USA, pp. 647–653.

Whitfield-Gabrieli, S., Nieto-Castanon, A., 2012. Conn: a functional connectivity toolbox for correlated and anticorrelated brain networks. Brain Connect. 2, 125–141. doi:10.1089/brain.2012.0073

Wijdicks, E.F.M., Bamlet, W.R., Maramattom, B.V., Manno, E.M., McClelland, R.L., 2005. Validation of a new coma scale: The FOUR score. Ann. Neurol. 58, 585–593. doi:10.1002/ana.20611

Woods, R.P., Mazziotta, J.C., Cherry, S.R., 1993. MRI-PET registration with automated algorithm. J. Comput. Assist. Tomogr. 17, 536–546.

Worsley, K.J., Evans, A.C., Marrett, S., Neelin, P., 1992. A three-dimensional statistical analysis for CBF activation studies in human brain. J. Cereb. Blood Flow Metab. Off. J. Int. Soc. Cereb.

Blood Flow Metab. 12, 900–918. doi:10.1038/jcbfm.1992.127
Wutzl, B., Leibnitz, K., Rattay, F., Kronbichler, M., Murata, M., Golaszewski, S.M., in prep. Genetic Algorithms for feature selection when classifying severe chronic disorders of consciousness.
Wutzl, B., Leibnitz, K., Rattay, F., Kronbichler, M., Murata, M., Golaszewski, S.M., in prep. Classifying patients with severe chronic disorders of consciousness using multislice modularity of brain networks from fMRI data.
Wutzl, B., Unterrainer, A.F., Kronbichler, M., Rattay, F., Trinka, E., Gerstenbrand, F., Golaszewski, S.M., 2018. Functional Magnetic Resonance Imaging under anaesthesia of a patient with severe chronic disorders of consciousness. Clin. Neurol. Neurosurg. doi:10.1016/j.clineuro.2018.06.029
Zeller, A., 2017. Neuronale Korrelate der Stimulusverarbeitung bei Bewusstseinsstörungen in funktioneller Magnetresonanztomographie (Dissertation). Universität Salzburg.
Zeman, A., 2001. Consciousness. Brain 124, 1263–1289. doi:10.1093/brain/124.7.1263
Zheng, Z.S., Reggente, N., Lutkenhoff, E., Owen, A.M., Monti, M.M., 2016. Disentangling disorders of consciousness: Insights from diffusion tensor imaging and machine learning. Hum. Brain Mapp. 38, 431–443. doi:10.1002/hbm.23370

List of Abbreviations

AC. *anterior commissure*
ALS. *amyotrophic lateral sclerosis*
AS. *apallic syndrome*
AUC. *area under the curve*
B_0. *outer magnetic field*
BCI. *brain-computer interface*
BMI. *brain-machine interface*
BOLD. *blood oxygenation level dependent*
CBF. *cerebral blood flow*
CBV. *cerebral blood volume*
CJD. *Creutzfeldt-Jakob disease*
CLOCS. *Comprehensive Levels of Consiousness Scale*
$CMRO_2$. *cerebral metabolic rate of oxygenation consumption*
CNC. *Coma/Near Coma Scale*
Cr. *creatine*
CRS-R. *Coma Recovery Scale-Revised*
CSF. *cerebrospinal fluid*
dHb. *deoxygenated hemoglobin*
DOCS. *Disorders of Consiousness Scale*
EEG. *electroencephalography*
EPI. *echo planar imaging*
FA. *flip angle*
FDR. *false discovery rate*
FLAIR. *fluid-attenuated inversion recovery*
fMRI. *functional magnetic resonance imaging*
FOUR. *Full Outline of UnResponsiveness Score*
FOV. *field of view*
FWE. *family wise error*
FWHM. f*ull width half maximum*
g. *Earth's gravitational field*
GA. *genetic algorithm*
GCS. *Glasgow Coma Scale*
GLM. *general linear model*
GLS. *Glasgow-Liege Coma Scale*
GM. *gray matter*
GRAPPA. *generalized autocalibrating partial parallel acquisition*
HMPAO. hexamethylpropylenaminooxim
HRF. *hemodynamic response function*
ICA. *Independent Component Analysis*
iLOC l. *lateral occipital cortex, inferior division left*
iLOC r. *lateral occipital cortex, inferior division right*
INNS. *Innsbruck Coma Scale*
J. *angular momentum*
kg. *kilogram*
LIPS. *locked-in plus syndrome*

LIS. *locked-in syndrome*
LOEW. *Loewenstein Communication Scale*
MCS. minimally conscious state
MEG. *magnetoencephalography*
mg. *milligram*
mi. *myo-inositol*
mm. *millimeter*
MNI. *Montréal Neurological Institute*
MPRAGE. *magnetization prepared rapid gradient echo*
MRI. *magentic resonance imaging*
MRS. *magnetic resonance spectroscopy*
ms. *milliseconds*
NAA. *N-acetyl-aspartate*
NMR. *nuclear magnetic resonance*
OFusG r. *occipital fusiform gyrus right*
OP l. *occipital pole left*
PC. *posterior commissure*
PCA. *principal component analysis*
PET. *positron-emission tomography*
PreCG l. *precentral gyrus left*
PreCG r. *precentral gyrus right*
RLS85. *Swedish Reaction Level Scale 1985*
ROI. *region of interest*
s. *seconds*
scBS. *schwere chronische Bewusstseinsstörungen*
scDOC. *severe chronic disorders of consciousness*
sCJD. *sporadic Creutzfeldt-Jakob disease*
SMART. *Sensory Modality Assessment Technique*
SPECT. *single photon emission computed tomography*
SPM. *Statistical Parametric Mapping*
SSAM. *Sensory Stimulation Assessment Measure*
SVC. *support vector classifier*
TE. *echo time*
TI. *time of inversion*
TP l. *temporal pole left*
TP r. *temporal pole right*
TR. r*epetition time*
UWS. unresponsive wakefulness syndrome
vCJD. *new variant Creutzfeldt Jakob Disease*
VS. *vegetative state*
WHIM. *Wessex Head Injury Matrix*
WM. *white matter*
WNSSP. *Western Neuro Sensory Stimulation Profile*
γ . *gyromagnetic ratio, modularity resolution (Mucha)*
μ . *magentic moment*
ν . *Larmor frequency*
ω . *angular velocity, coupling parameter (Mucha)*

Curriculum Vitae: Betty Wutzl

Personal Data

Name:	Betty (legal name: Bettina)
Second name:	WUTZL
Academic title:	Bachelor of Science (BSc), Bakkalaurea der Naturwissenschaften (Bakk.rer.nat.), Magistra der Naturwissenschaften (Mag.rer.nat.), Diplom-Ingenieurin (DI)
Date of birth:	27.09.1988
Place of birth:	St. Pölten
Nationality:	Austrian
Address:	Osaka, Japan

Education

since 02.02.2015	**Doctoral program** in Engineering Sciences at TU Wien, Austria Thesis working title: Network analysis of brain functions of patients with severe chronic disorders of consciousness using functional magnetic resonance imaging Supervisor: Rattay F., Golaszewski S.M.
07.01.2018-28.01.2018	IBRO-Simons Computational Neuroscience Imbizo, **Summer school**, Cape Town, South Africa
27.07.2015-31.07.2015	Brain Connectivity Methods **Workshop**, Temple University, Philadelphia, USA
01.10.2014-10.07.2017	**University Course** Medical Physics at Medical University of Vienna, Austria

Mathematics:

17.11.2014	Master degree: **Diplom-Ingenieurin (DI) equals Master of Science (MSc)** of TU Wien, Austria Thesis: Research for a linear optimised power model of Italy with focus on the hydro power system of Veneto, supervisor: F. Rattay
01.10.2010-17.11.2014	**Master Program** Mathematics in Science and Technology at TU Wien, Austria (completed with distinction)
28.09.2010	Bachelor degree: **Bachelor of Science (BSc)** of TU Wien, Austria Thesis: Discussion of curves in the three dimensional Lorentz-Minkowski space, supervisor: F. Manhart
01.10.2006- 28.09.2010	**Bachelor Program** Mathematics in Science and Technology at TU Wien, Austria

Astronomy:

17.11.2011	Bachelor degree: **Bakkalaurea der Naturwissenschaften (Bakk.rer.nat.)** of the University of Vienna, Austria Thesis: Stellar Equilibrium and Collapse, supervisor: E. Dorfi
01.10.2008-17.11.2011	**Bachelor Program** Astronomy

Physics:

10.04.2013	Master degree **Magistra der Naturwissenschaften (Mag.rer.nat.)** of the University of Vienna, Austria Thesis: Locally rotationally symmetric Bianchi type I cosmological models with anisotropic matter sources, supervisor: J.M. Heinzle
Summer Semester 2010	**Semester abroad** at Complutense University of Madrid, Spain
01.10.2006-10.04.2013	**Diploma Program** (combined Bachelor and Master Program) Physics (completed with distinction) at the University of Vienna, Austria

Work Experience

01.04.2017-present	**Research student (Monbukagakusho Scholarship)** at Osaka University, Japan project title: Detectability and comparative evaluation of brain resting state networks from different imaging modalities supervisor: Murata M., Leibnitz K.
01.02.2015-31.03.2017	**Research associate** at Paracelsus Medical University Salzburg
27.06.2013-23.10.2013	**IAESTE Internship** at Karunya Institute of Technolgy and Sciences, India Project title: Dynamics of Photorefractive Similaritons, supervisor: T.Soloman Raju
01.10.2008-28.02.2010	**Tutor** for the laboratory lecture “Physics for Nutritionists“ at the
01.10.2010-29.02.2012	University of Vienna, Austria
04.08.2008-29.08.2008	**Assistant** of the Local Authority of Hofstetten-Grünau, Austria
23.07.2007-12.08.2007	**Assistant** at the Production at Constantia Teich GmbH, Austria
24.07.2006-13.08.2006	**Assistant** at the Production at Constantia Teich GmbH, Austria
04.07.2005-31.07.2005	**Assistant** at the Quality Management at Constantia Teich GmbH, Austria

Publications

- Functional magnetic resonance imaging under anaesthesia of a patient with severe chronic disorders of consciousness, Wutzl B., Unterrainer A.F., Kronbichler M., Rattay F., Trinka E., Gerstenbrand F., Golaszewski S.M., Clinical Neurology and Neurosurgery, Volume 172, September 2018
- Genetic Algorithms for feature selection when classifying severe chronic disorders of consciousness, Wutzl B., Leibnitz K., Rattay F., Kronbichler M., Murata M., Golaszewski S.M., in preparation
- Classifying patients with severe chronic disorders of consciousness using multislice modularity of brain networks from fMRI data, Wutzl B., Leibnitz K., Rattay F., Kronbichler M., Murata M., Golaszewski S.M., in preparation
- FMRI findings in the final stage of Creutzfeldt-Jakob-disease, Golaszewski S.M., Wutzl B., Unterrainer A.F., Florea C., Kronbichler M., Kronbichler L., Nardone R., Rattay F., Trinka E., Weis S., in preparation

Conference contributions

OHBM 2018 (Organisation for Human Brain Mapping)

- The role of fMRI in the diagnosis and prognosis of patients with disorders of consciousness, Wutzl B, Golaszewski S, Florea C, Schwenker K, Rattay F, Trinka E, Gerstenbrand F, Leibnitz K, Murata M; poster 19.-21.6.2018

The 4th CiNet Conference

- Comparison of brain resting state networks from different imaging modalities, Wutzl B, Leibnitz L; poster, 26.-27.2.2018

EAN 2017 (3rd Congress of the European Academy of Neurology)

- Promising and highly diagnostic fMRI paradigms for classifying the level of consciousness of patients with severe chronic disorders of consciousness, Wutzl B, Florea C, Schwenker K, Rattay F, Trinka E, Gerstenbrand F, Golaszewski SM; oral presentation 25.06.2017
- Cortical afferent inhibition reflects cognitive impairment in obstructive sleep apnea syndrome: a TMS study, Golaszewski SM, Kunz AB, Schwenker K, Wutzl B, Seidl M, Brigo F, Höller Y, Florea C, Trinka E, Nardone R; poster 24.-27.06.2017

EAN 2016 (2nd Congress of the European Academy of Neurology)

- The role of functional MRI in the diagnosis and prognosis of patients with severe chronic disorders of consciousness, Wutzl B, Florea C, Seidl M, Kunz AB, Schwenker K, Nardone R, Trinka E, Gerstenbrand F, Golaszewski S; oral presentation, 29.05.2016
- Whole-hand electrical stimulation in stroke patients in the subacute stage, Schwenker K., Christova M, Wutzl B, Bartsch H, Nardone R, Gallasch E, Rafolt D, Gerstenbrand F, Trinka E, Golaszewski S; oral presentation, 29.05.2016
- Long-Term Coma State and the Bedrest Syndrom, Golaszewski S, Wutzl B, Florea C, Kunz AB, Seidl M, Schwenker K, Nardone R, Trinka E, Gerstenbrand F; poster, 30.05.2016
- The Locked-In-Plus-Syndrome, Golaszewski S, Florea C, Wutzl B, Seidl M, Kunz AB, Schwenker K, Nardone R, Trinka E, Gerstenbrand F; poster, 30.05.2016

ÖGN 2016 (13. Jahrestagung der Österreichischen Gesellschaft für Neurologie)

- Long-Term Coma State and the Bedrest Syndrom, Golaszewski SM, Florea C, Wutzl B, Schwenker K, Kunz A; poster, 16.-18.03.2016

SCI-TReCS Summit 2015 (Spinal Cord and Injury Tissue Regeneration Center Salzburg Summit)

- Stimulation of the proprioceptive System in SCI patients, Golaszewski SM, Wutzl B, Schwenker K, Kunz AB, Seidl M, Florea C, Leis S, Trinka E, Gerstenbrand F; poster, 05.11.2015

WRAP 2013 (Workshop on Recent Advances in Photonics, IEEE)

- Dynamics of Photorefractive Similaritons, Wutzl B, Soloman Raju T; paper, 17.-18.12.2013

Prize

Runner-up prize: EAN Tournament “Basic Neurology”, European Academy of Neurology, 2017

Programming Skills

- LaTeX
- MATLAB (including SPM, CONN)
- python
- Maple (basics)
- R (basics)
- C (basics)

Language Skills

- German (native)
- English (fluent)
- Spanish (fluent)
- Italian (basic)
- Japanese (basic)
- French (basic)
- Latin